CENTRAL RESEARCH LIBRARY
DOCUMENT COLLECTION

[redacted]

1

OAK RIDGE NATIONAL LABORATORY
operated by
UNION CARBIDE CORPORATION
NUCLEAR DIVISION
for the
U.S. ATOMIC ENERGY COMMISSION

UNION CARBIDE

LOCKHEED MARTIN ENERGY RESEARCH LIBRARIES
3 4456 0513437 9

ORNL-TM-1941

DECLASSIFIED
CLASSIFICATION CHANGED TO:
BY AUTHORITY OF: AECM-2104 a.2 B6 8/21/74
BY: BL Rudd

FUELS AND MATERIALS DEVELOPMENT PROGRAM QUARTERLY PROGRESS REPORT FOR PERIOD ENDING JUNE 30, 1967

P. Patriarca

OAK RIDGE NATIONAL LABORATORY
CENTRAL RESEARCH LIBRARY
DOCUMENT COLLECTION
LIBRARY LOAN COPY
DO NOT TRANSFER TO ANOTHER PERSON
If you wish someone else to see this document, send in name with document and the library will arrange a loan.
UCN-7969
(3 3-67)

[redacted]

NOTICE This document contains information of a preliminary nature and was prepared primarily for internal use at the Oak Ridge National Laboratory. It is subject to revision or correction and therefore does not represent a final report.

[redacted]

LEGAL NOTICE

This report was prepared as an account of Government sponsored work. Neither the United States, nor the Commission, nor any person acting on behalf of the Commission:

A. Makes any warranty or representation, expressed or implied, with respect to the accuracy, completeness, or usefulness of the information contained in this report, or that the use of any information, apparatus, method, or process disclosed in this report may not infringe privately owned rights; or

B. Assumes any liabilities with respect to the use of, or for damages resulting from the use of any information, apparatus, method, or process disclosed in this report.

As used in the above, "person acting on behalf of the Commission" includes any employee or contractor of the Commission, or employee of such contractor, to the extent that such employee or contractor of the Commission, or employee of such contractor prepares, disseminates, or provides access to, any information pursuant to his employment or contract with the Commission, or his employment with such contractor.

[redacted]

ORNL-TM-1941

Contract No. W-7405-eng-26

FUELS AND MATERIALS DEVELOPMENT PROGRAM QUARTERLY PROGRESS REPORT FOR PERIOD ENDING JUNE 30, 1967

Compiled by

P. Patriarca

SEPTEMBER 1967

OAK RIDGE NATIONAL LABORATORY
Oak Ridge, Tennessee
operated by
UNION CARBIDE CORPORATION
for the
U.S. ATOMIC ENERGY COMMISSION

[redacted]

LOCKHEED MARTIN ENERGY RESEARCH LIBRARIES

3 4456 0513437 9

[redacted]

FOREWORD

This is the thirteenth quarterly progress report describing work performed at the Oak Ridge National Laboratory for the Fuels and Materials Branch, Division of Reactor Development and Technology, U.S. Atomic Energy Commission. The specific programs covered are as follows:

Program Title	Person in Charge	Principal Investigator(s)
Part I. Metals and Ceramics Division		
Fuel Element Fabrication Development	G. M. Adamson, Jr.	W. R. Martin
Mechanical Properties	C. J. McHargue	J. R. Weir, Jr.
Nondestructive Test Development	W. O. Harms	R. W. McClung
Sintered Aluminum Products	G. M. Adamson, Jr.	W. R. Martin D. G. Harman
Zirconium Metallurgy	C. J. McHargue	P. L. Rittenhouse
Weldability of Nickel-Bearing Alloys	G. M. Adamson, Jr.	G. M. Slaughter
Part II. Reactor Chemistry Division		
Fission-Gas Release and Physical Properties of Fuel Materials During Irradiation	O. Sisman	R. M. Carroll J. G. Morgan

[redacted]

[redacted]

[redacted]

[redacted]

CONTENTS

Page

Summary vii

Part I. Metals and Ceramics Division

1. Fuel Element Fabrication Development 3

Conversion of UF_6 to UO_2 with a Flame Reactor 3

Preparation of PuO_2 Powder from PuF_6 by Chemical Vapor Deposition 4

Deposition of Tungsten-Rhenium Alloys 4

Irradiation Testing of 240-g Oak Ridge Reactor Fuel Elements . . 9

2. Mechanical Properties 13

In-Reactor and Postirradiation Stress-Rupture Properties of Type 304 Stainless Steel 13

Mechanical Properties of Type 304 Stainless Steel Containing Cyclotron-Injected Helium 16

Mechanical Properties of 0.2 wt % Ti-Modified Type 304L Stainless Steel Containing Cyclotron-Injected Helium 17

Electron Microscopy of Irradiated Stainless Steels 18

MSRE Surveillance Program — Hastelloy N 19

Measurement of the Nuclear Heating Rate in EBR-II 30

3. Nondestructive Test Development 35

Electromagnetic Test Methods 35

Analytical Studies 35

Phase-Sensitive Eddy-Current Instrument 36

Ultrasonic Test Methods 36

Fabrication of Reference Notches 36

Reference Standards 37

Optical Visualization of Ultrasound 38

Penetrating Radiation Methods 38

4. Sintered Aluminum Products Development 41

Dispersion Preparation 41

Powder Consolidation 44

Fracture Studies of SAP Alloys 49

Nondestructive Testing 52

SAP-UC Compatibility Experiments 53

[redacted]

[redacted]

Page

5. Zirconium Metallurgy 54
   Anisotropy in Zircaloy 54
      Tubing Tests 54
      Strain Behavior in Uniaxially Tested Zircaloy Tubing 54
   Texture Development in Single-Crystal Zirconium 57
      Rolling Textures 58
      Drawing Studies 61
   Optical Properties of Zirconium Alloys 63
   Inhibition of Oxidation by Anodic Films 66
6. Weldability of Nickel-Bearing Alloys 69
   Special Alloy Fabrication 69
      VARESTRAINT Testing Performed Under Subcontract at Rensselaer Polytechnic Institute 70
      Test Development 74
   The Effect of Energy Input on the Mechanical Properties of Austenitic Stainless Steel Welds 75

Part II. Reactor Chemistry Division

7. Fission-Gas Release and Physical Properties of Fuel Materials During Irradiation 81
   Steady-State Fission-Gas Release from UO_2 Single-Crystal Specimen Cl-19 82
   Low-Temperature, Knockout Release 85
   The Mixing of a Trace Gas in Flowing Helium 87
   Thermal Diffusivity of Single-Crystal UO_2 During Irradiation . . 92

[redacted]

[redacted]

SUMMARY

PART I. METALS AND CERAMICS DIVISION

1. Fuel Element Fabrication Development

We have continued our work with the flame reactor to produce submicron size powders of urania. The powder-collection system has been modified to improve the quality and type of product. We have made an initial experiment in which WF_6 was reduced simultaneously with UF_6. This technique may enable us to produce duplex structures of metal dispersed within the urania.

The experimental device in which we plan to make PuO_2 from PuF_6 has been altered to satisfy hazards review. Approval of that review is pending.

Chemical vapor deposition (CVD) of tungsten-rhenium binary alloys is directed toward the production of longer lengths of tubing by the direct deposition technique. Attempts to scale up the injector-moving mandrel technique were not successful. A second technique, called the external-coating method, is being pursued.

Evaluation of ORR fuel elements containing a 20% increase in fuel loading is being completed. These elements were irradiated to greater than 60% burnup with no deleterious effects noted during reactor operation. Postirradiation examination shows that the powder-metallurgy product exhibited less swelling than did the cast alloy.

2. Mechanical Properties

The creep-rupture properties of type 304 stainless steel at 650°C have been investigated in the presence of a neutron flux of 6×10^{13} neutrons cm^{-2} sec^{-1}, after irradiation, and in the unirradiated condition. No change in the creep rate was found that could be attributed to the effects of irradiation. However, as expected the rupture time and ductility were decreased.

Work has continued involving the introduction of helium into stainless steels using the Oak Ridge Isochronous Cyclotron. The results for

[redacted]

a 1 ppm He concentration in fine-grained and coarse-grained type 304 stainless steel show essentially the same grain-size effect as has been observed in reactor-irradiated type 304 stainless steel. Samples of the 0.2% Ti-modified stainless steel containing 1 ppm He exhibit no loss in ductility when tested in the fine-grained condition. However, the material annealed at 1038°C shows a slight decrease in ductility at test temperatures above 700°C.

Electron microscopic observations of helium bubbles in a titanium-bearing stainless steel have led to several interesting conclusions regarding their location in the metal, the most important of which is that bubbles do attach themselves to precipitates in the alloy.

A systematic study has been conducted of the mechanical properties of Hastelloy N irradiated in the ORR and the Molten-Salt Reactor Experiment to similar fluence. The results of tests from 20 to 850°C indicate that the effects produced were similar for both irradiation facilities.

Our experiments designed to measure the nuclear heating rate in EBR-II have been delivered to the EBR-II site and are awaiting insertion.

3. Nondestructive Test Development

We are developing new techniques and equipment for the nondestructive evaluation of materials and components. Major emphasis has been on eddy-current, ultrasonic, and penetrating-radiation methods.

Our analytical work on electromagnetic phenomena has included beginning approximation and evaluation of integrals for closed-form solutions and issuance of a report on calculation of forces. Improvements have been made to the temperature stability of the portable phase-sensitive instrument. Complete construction details for the instrument and probe coils have been completed.

In our work on electro-discharge machining of reference discontinuities we have continued to emphasize calibrated transverse notches in very small-diameter tubing. Comparison of response from various reference discontinuities in sheet is continuing with change in response being measured in decibels. A paper was prepared, presented, and is to be published summarizing the development of our optical system for viewing ultrasonics.

We evaluated data for the low-voltage radiography of graphite and generated charts showing the proper operating conditions for optimum radiography.

4. Sintered Aluminum Products Development

Aluminum oxide-strengthened alloys are high-strength alloys that have possible applications in several reactor systems. These alloys with high strength-to-weight ratios and low-neutron absorption cross sections could be used at temperatures less than 350°C.

Our program has been to investigate the problems and parameters related to primary billet fabrication of SAP. General process steps involve feed-powder characterization, dispersion preparation, and consolidation. We completed the preparation of specifications for atomized powder and ball-milled flake and have selected the billet consolidation process. We have found that the properties of the end product can be influenced by the manner in which the consolidated billet is reduced. Although one can produce a billet having properties consistent within a 5% level, the magnitude of these properties is altered by secondary fabrication.

Our nondestructive testing effort has been concerned with the development of systems and techniques for determination of flake thickness and oxide content of the aluminum powders. An air-settling device is being developed for the flake-thickness measurements and eddy-current techniques are being employed for the determination of oxide content.

5. Zirconium Metallurgy

The strains that occur in the diameter and wall thickness of uniaxially tested Zircaloy tubing are related to the crystallographic texture of the material. It is possible to use these strain data to study anisotropy and texture in tubing of any metal or alloy.

The crystallographic textures produced by rolling and drawing zirconium single crystals of selected orientations have been studied. In every instance the single-crystal specimens deformed by easily

[redacted]

identifiable sequences of twinning and slip. The textures formed are almost identical to those observed in fabricated polycrystalline zirconium.

Reflectivity measurements are being made on large grains of zirconium of known crystallographic orientation. These data should permit us to make texture determinations in polycrystalline material by an optical technique.

The oxidation weight gain of arc-melted crystal-bar zirconium in 500°C (15 psia) steam is reduced by a factor of 4 up to at least 750 hr of exposure by preanodizing in concentrated H_3PO_4.

6. Weldability of Nickel-Bearing Alloys

Melting and fabrication were completed on four series of special alloys for weldability testing both at Rensselaer Polytechnic Institute under subcontract and at ORNL. Chemical analyses are presented which point out the excellent quality and reproducibility obtained with the in-house melting and fabrication processes.

Testing at RPI has continued. VARESTRAINT results are presented for the high-purity Incoloy 800 alloys containing controlled additions of aluminum and titanium. The weldability versus compositional data currently are being programmed for computer analysis at RPI.

A preliminary study has been completed on the effect of energy input on the mechanical properties of austenitic stainless steel welds. Unlike welds in ferritic steels, changes in mechanical properties in these materials cannot be affected by refinement or coarsening of the microstructure during cycling through the face-centered cubic to body-centered cubic transformation range. Significant differences in ultimate tensile strength for various heat inputs were correlated with microstructures.

[redacted]

[redacted]

PART II. REACTOR CHEMISTRY DIVISION

7. Fission-Gas Release and Physical Properties of Fuel Materials During Irradiation

Fission-gas release measurements were obtained with the single-crystal specimen at temperatures up to 1700°C. Some effect of burnup was detected and it seems as if the gas-release mechanism is mainly by the migration of small defect clusters containing fission gas. No effects of grain growth were observed at 1700°C, as might be expected from a single-crystal specimen. Only a small fraction (4×10^{-4} R/B) of the ^{88}Kr generated was released at 1700°C.

A satisfactory theoretical treatment of the mixing of a trace gas in flowing helium was developed, based on experimental measurements.

The pulse method of measuring thermal diffusivity did not yield data of the required accuracy from a hollow cylinder, single-crystal specimen of UO_2. The specimen has been replaced with a slightly larger specimen of fine-grain UO_2 and the method will be tried again.

[redacted]

[redacted]

[redacted]

[redacted]

PART I.

METALS AND CERAMICS DIVISION

[redacted]

[redacted]

[redacted]

1. FUEL ELEMENT FABRICATION DEVELOPMENT

W. R. Martin

The direct conversion of fissionable halides to refractory fuel compounds by chemical vapor deposition (CVD) is being investigated for uranium and plutonium oxide fuels. We have studied techniques with application to the heavy-metal fluorides and chlorides. Our method of conversion has involved hydroreduction, reduction with hydrogen and alkali vapors of the halide, followed by oxidation of the heavy metal. Our CVD work is presently concentrating on the preparation of PuO_2 powder from PuF_6 and conversion of UF_6 to UO_2 using a high-temperature flame reactor.

We are continuing our work on the direct deposition of binary refractory-metal alloys with our current effort on the tungsten-rhenium system. Alloys in the form of tubing having a uniform composition are being investigated.

Investigation of research reactor fuel elements fabrication variables is under way. We are currently examining cast and powder-metallurgy produced uranium-aluminum alloys that have been irradiated as 240-g ^{235}U ORR fuel elements.

Conversion of UF_6 to UO_2 with a Flame Reactor

W. C. Robinson, Jr.

The water coolant coils were removed from the powder collector pan at the bottom of the reaction vessel. Previously, water formed in the conversion reaction had condensed in the pan and then adsorbed HF, which is also a product of the UF_6 reaction with hydrogen and oxygen. When the UO_2 powder landed in the H_2O-HF mixture, it was reconverted to UF_4. The removal of th the water coolant stopped the condensation of the water product. Two dry traps were added in an attempt to catch the UO_2 that passed the collection pan. They were successful in removing the bulk of the powder.

Four additional experiments were conducted with a variation in inlet flow rates. All runs utilized a fluorine rate of 670 cfm to establish a

flame front and the hydrogen was varied from 3000 to 3600 cfm, the UF_6 varied from 80 to 125 cfm, and the oxygen varied from 150 to 1000 cfm. The principal reaction products were identified as UO_2 and U_3O_8 in all experiments except at the extremes of maximum UF_6 and minimum oxygen in which UF_4 appeared. The experiments were all conducted within a pressure range of 3 to 4 torrs. The product of all runs is presently undergoing more thorough characterization.

Another experiment was performed with WF_6 also being introduced into the reaction chamber in an attempt to prepare a tungsten-UO_2 composite powder in which the tungsten is distributed within the urania matrix. This product is also being characterized.

Preparation of PuO_2 Powder from PuF_6 by Chemical Vapor Deposition

W. C. Robinson, Jr.

The previously existing design on the conversion apparatus was submitted to the General Engineering and Construction Division, who recommended several changes. All lines containing fluorine gas were changed from stainless steel to Monel. The design called for storage of the fluorine gas cylinder outside the building on a bottle rack. However, permission to place this large fluorine cylinder on the rack in proximity of other cylinders of hydrogen, argon, and oxygen was denied unless a brick enclosure was constructed around it. However, we have ordered a smaller cylinder of fluorine which may be placed inside the first glove box. Swagelok fittings were not allowed as connections on the lines. All fittings are presently being back-welded into place in the hydrogen lines. These changes were incorporated into the Hazards Review and resubmitted for approval.

Deposition of Tungsten-Rhenium Alloys

J. I. Federer

Chemical vapor deposition of tungsten-rhenium alloys by hydrogen reduction of WF_6 and ReF_6 has continued. The objective of these experiments is the preparation of tubing and flat stock for evaluation of

mechanical properties. Two experimental methods were used: (1) scale-up of the injector-moving mandrel technique for deposition on the inner wall of tubular mandrels[1] and (2) deposition on the outer wall of tubular or sheet-type mandrels. Nodular growths still characterize deposits made by the first method;[2] however, more satisfactory deposits have been prepared by the second method.

Eleven experiments were conducted using the injector-moving mandrel technique to deposit alloys containing nominally 5 and 25% Re. In these experiments the hydrogen-to-WF_6 + ReF_6 ratio was varied from 10 to 50 and the temperature from 650 to 950°C at a pressure of 5 torrs. The tubular mandrels were either 2 in. in inside diameter with a circular cross section or 2 in. in outside diameter with an octagonal cross section. The following results were obtained: (1) metal recoveries ranged between 95 and 100% of the metal content of the metered gases, (2) the composition of the deposits corresponded to the metal content of the metered gases and was nearly constant along the length, and (3) the grain structure and surface texture were nodular.

Thus, attempts to scale up the injector-moving mandrel technique were not successful due to the nodular growths that were characteristic of the deposits. This technique has been discontinued in favor of the external coating method.

The external coating method uses tubular or sheet-type mandrels that are resistance heated inside a relatively large cold-wall chamber. Tungsten tubes deposited in this apparatus had a constant wall thickness over a 40-in. length. Apparently the deposition rate on a deposit heated by self-resistance compensates automatically for thickness variations, the rate being inversely proportional to thickness for a given power input.

Alloys containing nominally 5 and 25% Re were deposited at 800 and 950°C, respectively, a hydrogen-to-WF_6 + ReF_6 ratio of 15, and a pressure of 5 torrs. The mandrels were steel sheet measuring 5/8 and 1 1/4 in.

---

[1]J. I. Federer and W. R. Martin, Fuels and Materials Development Program Quart. Progr. Rept. Dec. 31, 1966, ORNL-TM-1720, pp. 16–19.

[2]J. I. Federer and W. R. Martin, Fuels and Materials Development Program Quart. Progr. Rept. Mar. 31, 1967, ORNL-TM-1825, pp. 13–18.

[redacted]

wide, 0.030 in. thick, and 18 in. long. The deposition rate in alloy deposits, unlike that of tungsten, does not compensate automatically for thickness variations. Instead, the deposits were thickest near the gas inlet and decreased gradually along the length. The grain structures, however, were columnar and the surface textures were smooth. The thickness and rhenium content along the length of a typical deposit are as follows:

Distance from Gas Inlet (in.)	Rhenium Content (%)
2	3.30
6	3.19
10	3.35
14	3.51

These results show that the rhenium content was constant, even though the thickness decreased along the length, indicating that neither WF_6 nor ReF_6 was selectively reduced. The thickness variation may be due to simultaneous depletion of both WF_6 and ReF_6 and might be overcome by increasing flow rates. Alternatively, reversing the direction of flow over the mandrel during deposition might also improve the thickness uniformity.

Investigation of the A15-type phase in tungsten-rhenium alloys has been completed.[3] Characterization involved the following specific areas of study:

1. temperature and composition limits for formation;
2. metallographic delineation of the A15 phase coexisting with the tungsten-rich solid solution (beta phase);
3. hardness measurements to account for the brittleness of alloys containing the phase;
4. stability and transformation products of the phase during anneals at elevated temperatures;
5. confirmation of the crystal structure type and ordering arrangement, hence confirmation of the identity of the phase as an A15 type.

[3]J. I. Federer, Formation and Characterization of an A15-Type Phase in Chemical Vapor Deposited Tungsten-Rhenium Alloys, ORNL-TM-1888 (in press).

[redacted]

[redacted]

Phases present in alloys deposited in the temperature range of 1000 to 1500°C are shown in relation to a portion of the tungsten-rhenium phase diagram in Fig. 1.1. The homogeneity range of the A15 phase is relatively wide and is not centered about the nominal composition A_3B, the usual composition of A15-type phases. Annealing at temperatures from 1300 to 2000°C caused the A15 phase to transform to beta or to (beta plus sigma) phases. Transformation to these products at deposition temperatures (1300 to 1500°C) showed that the A15 phase was metastable and that the equilibrium phase boundaries involving beta and sigma phases can be extrapolated to 1300°C. The transformation was not always completed in various alloys after 700 hr at 1300°C, but in every case the amount of A15 phase was less than that in the as-deposited condition. These annealing studies show that a single-phase beta alloy can be obtained at no higher temperature than is required for wrought alloys.

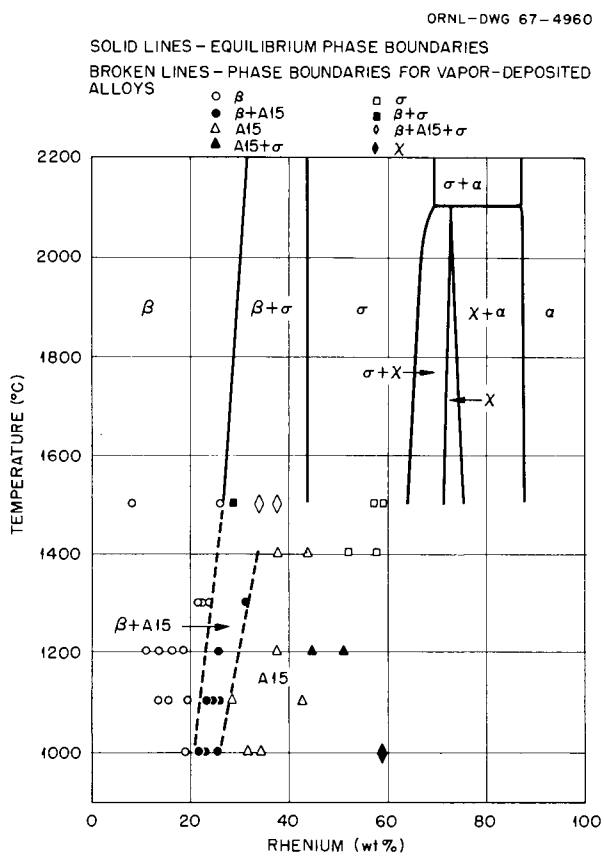

Fig. 1.1. Vapor-Deposited Phases Shown in Relation to the Tungsten-Rhenium Phase Diagram.

[redacted]

The microstructure of an alloy containing beta and a small amount of A15 phase is shown in Fig. 1.2. The hardness of the A15 phase (1950 DPH) is about 4 times that of beta (450 DPH), as shown by the relative size of the hardness impressions in Fig. 1.2, and about twice that of sigma (1030 DPH). The relatively high hardness of the A15 phase may limit the usefulness of alloys containing the phase as a major constituent. Electron microprobe analyses of the A15 phase coexisting with beta revealed no difference in composition between the two phases, which is additional evidence that the A15 phase is a metastable structural variation.

Fig. 1.2. Beta (Principal Phase) Plus A15 Phase Alloy Containing 26% Re Deposited at 1200°C.

The crystal structure was previously identified as an A15 type by x-ray diffraction experiments and was recently confirmed by a neutron diffraction experiment in which the ordering arrangement was determined.

A single-phase A15 alloy containing 38.9% Re was used in the latter experiment to avoid interference from the beta phase. In this alloy the atomic sites were occupied as follows: 73% of the normal tungsten sites occupied by tungsten, 27% of the normal tungsten sites occupied by rhenium, 79% of the normal rhenium sites occupied by rhenium, and 21% of the normal rhenium sites occupied by tungsten. Although not determined in this experiment, a stoichiometric tungsten-rhenium A15 phase W_3Re would probably be completely ordered.

In summary, the A15 phase in vapor-deposited tungsten-rhenium alloys is a metastable phase characteristic of the deposition process. The transformation products during annealing are the equilibrium beta and sigma phases. The A15 phase would not be expected to form in beta or (beta plus sigma) phase alloys subjected to service at elevated temperatures.

Irradiation Testing of 240-g Oak Ridge Reactor Fuel Elements

A. E. Richt W. R. Martin
J. H. Erwin

Because of potential savings in fuel costs, there is considerable incentive to increase the fuel loading of the ORR fuel elements from 200 to 240 g of ^{235}U. In order to ascertain that the heavier loaded elements would perform satisfactorily in service, we fabricated three 240-g fuel elements specifically for irradiation tests in the ORR. These elements, details of which are shown in Table 1.1, were irradiated at a process water temperature of 52°C to an average burnup of 60% depletion of ^{235}U (8.3×10^{20} fissions/cm^3) with no indications of failure. Two of the elements, NL-24 (Al–20% U) and NL-30S (Al–30% UAl_3 dispersion) are currently being examined in the hot cells. Examination of the third element (NL-26) awaits further decay.

Although we have not completed the examination of these elements, preliminary results indicate that both the alloy and intermetallic fuel elements performed quite satisfactorily in the ORR, even with the increased loadings. Dimensional measurements showed that the elements

Table 1.1. Details of ORR 240-g Irradiation Test Fuel Elements

Element Number	Type of Fuel	Cladding	Element Condition
NL-24	Al–22 wt % U alloy	1100 Al	20% cold worked
NL-26	Al–22 wt % U alloy	6061 Al	Fully annealed
NL-30S	Al–30 wt % UAl_3 dispersion	6061 Al	Fully annealed

had not bowed, warped, or twisted during irradiation. No evidence of significant changes in the width, height, or coolant channel spacings of the elements was found. The fuel plates of both elements had increased slightly in thickness as a result of irradiation. The thickness increase appeared to be directly proportional to burnup; however, at comparable burnup levels, plates fueled with the Al–22 wt % U alloy consistently showed slightly greater thickness increases than the plates fueled with the Al–30 wt % UAl_3 dispersion. At peak burnup areas (74% depletion of ^{235}U or 10.2×10^{20} fissions/cm^3), the alloy-fueled plates had increased approximately 0.0025 in. in thickness as compared to a 0.0015-in. thickness increase in the dispersion-fueled plates.

Metallographic examinations of sections from the irradiated elements indicate that changes in fuel plate thickness were a result of the combined effects of fuel swelling and the buildup of a corrosion-product film on the fuel plate surfaces. The greater thickness increase in the alloy-fueled plates can be attributed partially to a thicker oxide film on the surfaces of these fuel plates. However, our results also indicate that the alloy fuel swelled slightly more than the dispersion fuel at comparable burnup levels. The lower swelling of the dispersion fuel appears to be related to the porosity present in the UAl_3 particles of the as-fabricated fuel plate. During irradiation, swelling of the fuel particles is at least partially accommodated by consumption of this porosity. This effect is clearly shown in Fig. 1.3 where the voids in the UAl_3 particles of the as-fabricated fuel plate have completely disappeared after irradiation to a high burnup level. The alloy fuel, however, has essentially no pores in the as-fabricated condition and thus swells at the normal rate during irradiation.

[redacted]

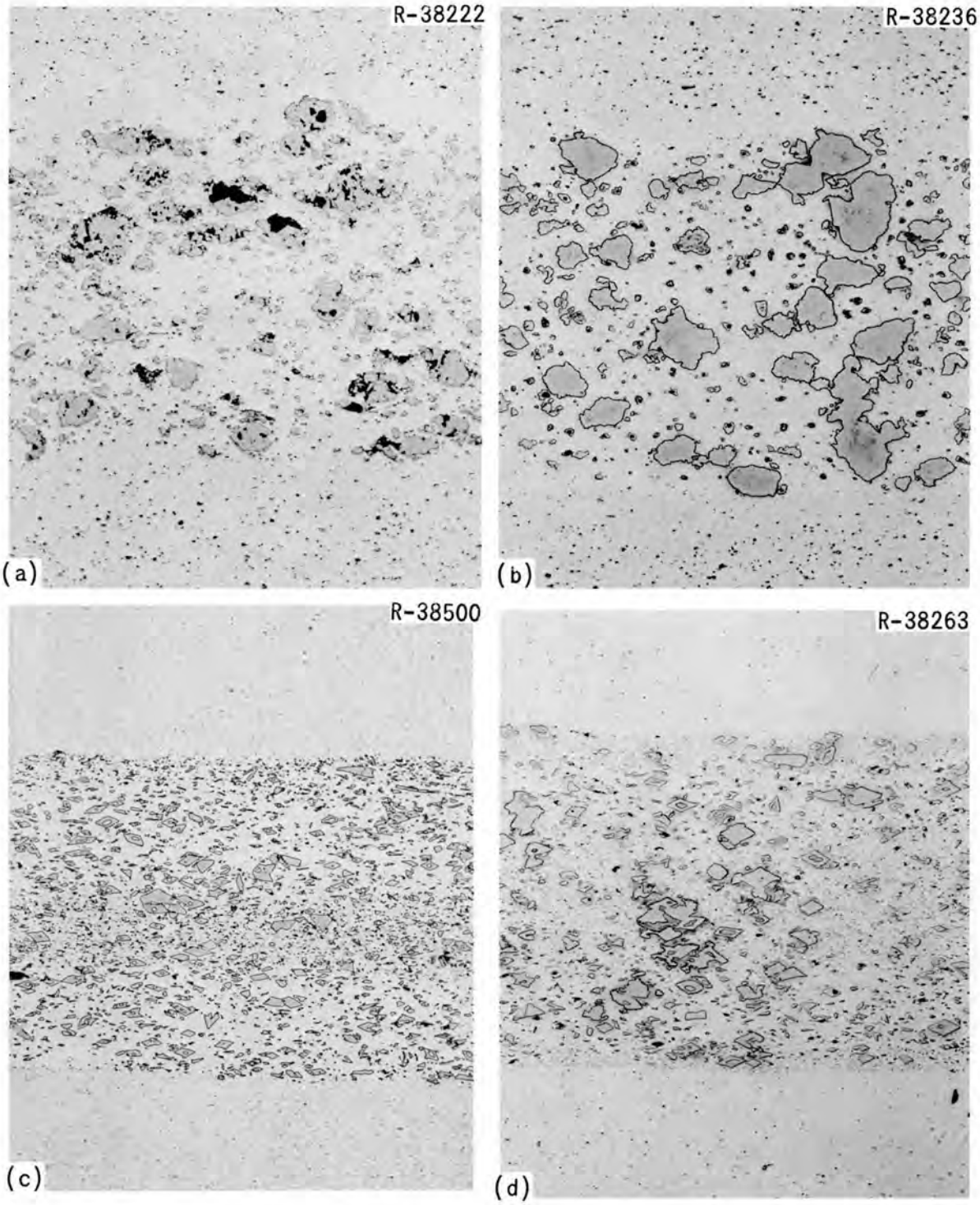

Fig. 1.3. Typical Microstructure of Fuel Plates from the 240-g ORR Fuel Elements. (a) Unirradiated Al–30 wt % UAl_3 dispersion, (b) Al–30 wt % UAl_3 dispersion after 10.2×10^{20} fissions/cm^3, (c) Unirradiated Al–22 wt % U alloy, (d) Al–22 wt % U alloy after 10.2×10^{20} fissions/cm^3. As polished. 100×.

[redacted]

[redacted]

Specimens cut from the minimum and maximum burnup regions of the fuel plates were subjected to postirradiation heat treatments to determine if there was any significant difference in the breakaway swelling temperature of the two types of fuel. As shown in Fig. 1.4, results of these tests indicate that the blistering temperature of the UAl_3 dispersion fuel is slightly higher than that of the alloy.

Although results of this examination program indicate that the UAl_3 dispersion is slightly more stable than the alloy, both types of fuel appear to be quite satisfactory for the 240-g ORR elements. Consequently selection of the fuel material for additional 240-g elements should probably be based upon economic considerations.

ORNL DWG. 67-8529

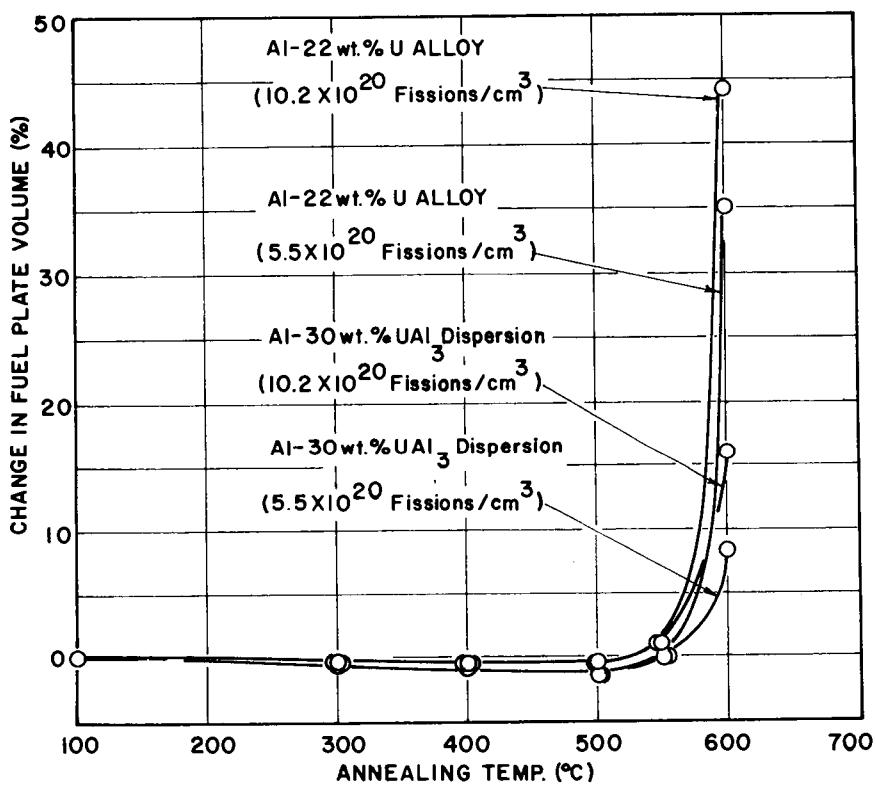

Fig. 1.4. Results of Postirradiation Heat Treatment on Dimensional Stability of ORR-type Fuel Plates.

[redacted]

2. MECHANICAL PROPERTIES

J. R. Weir, Jr.

One objective of this program is to determine the effect of irradiation on the mechanical properties of alloys of interest as fuel cladding and to find a metallurgical condition for the alloys that produces the least effect of subsequent irradiation on the mechanical properties. To accomplish this, our study concerns the interaction of radiation-induced defects and the substructure of the alloys, the effect of irradiation temperature, postirradiation test variables, and neutron dosimetry in the facilities used in the irradiations. The material selected for initial study is type 304 stainless steel and related compositions containing titanium. Additional materials will be studied including type 316 stainless steel, Incoloy 800, and three vanadium alloys. The Hastelloy N work is not supported by our Fuels and Materials Branch, but is added because of its general interest.

In-Reactor and Postirradiation Stress-Rupture Properties of Type 304 Stainless Steel

E. E. Bloom J. R. Weir, Jr.

The creep-rupture properties of type 304 stainless steel have been determined in the unirradiated condition and for irradiated specimens tested both during and after irradiation. Tests were performed at 650°C at stresses between 15,000 and 35,000 psi. The composition of the experimental alloy was as follows (by weight): 0.057% C, 0.76% Mn, 0.020% P, 0.016% S, 0.48% Si, 19.0% Cr, 8.9% Ni, and 2.2 ppm B. The final heat treatment prior to testing was a 1-hr anneal at 1038°C which developed a grain size of ASTM 6. In-reactor stress-rupture tests were conducted at a poolside position of the ORR. The thermal flux was 6×10^{13} neutrons cm^{-2} sec^{-1} and the fast ($E > 2.9$ Mev) flux 5×10^{12} neutrons cm^{-2} sec^{-1}. Postirradiation tests were performed on specimens irradiated at 650°C to a fluence of 2×10^{20} neutrons/cm^2 (thermal) and 2×10^{19} neutrons/cm^2 ($E > 2.9$ Mev).

Minimum creep rate and rupture life values for each test are listed in Table 2.1. The creep rates for both in-reactor and postirradiation

Table 2.1. Minimum Creep Rate and Rupture Life of Type 304 Stainless Steel[a]

Stress (psi)	Unirradiated		In-Reactor		Postirradiation	
	Minimum Creep Rate (%/hr)	Rupture Life (hr)	Minimum Creep Rate (%/hr)	Rupture Life (hr)	Minimum Creep Rate (%/hr)	Rupture Life (hr)
35,000	2.26	7.7				
30,000	0.92	9.0			0.50	12.0
27,500	0.33	44.1				
25,000	0.048	122.8	0.138	17.1	0.139	24.4
22,250	0.042	157.7				
20,750					0.014	123.4
20,000	0.0073	366.6	0.016	98.0		
17,000	0.0028	1876.0	0.0035	423.0	0.006	314.4
15,000	0.00032		0.0014		0.0018	956.9

[a]Tested at 650°C.

tests are a factor of 2 to 5 higher than those of the unirradiated alloy. It is important to note, however, that the irradiated specimens failed at times approximately equal to the time required for the establishment of secondary creep processes in the unirradiated alloy. Creep curves for irradiated and unirradiated specimens tested at a stress of 25,000 psi are shown in Fig. 2.1. Results of optical and electron metallography indicate that the primary effect of irradiation is an enhancement of the intergranular fracture process and that irradiation has little effect upon the deformation processes that occur during creep testing. It thus appears that the higher creep rates that were observed for the irradiated alloy were a result of fracture of the specimen while still in the primary stage of creep.

Ductility, as measured by elongation or reduction in area, was significantly reduced for both in-reactor and postirradiation tests. Figure 2.2 is a plot of ductility as a function of rupture life. For the stress levels used in this investigation, the loss of ductility became more severe as the stress (or strain rate) was reduced.

[redacted]

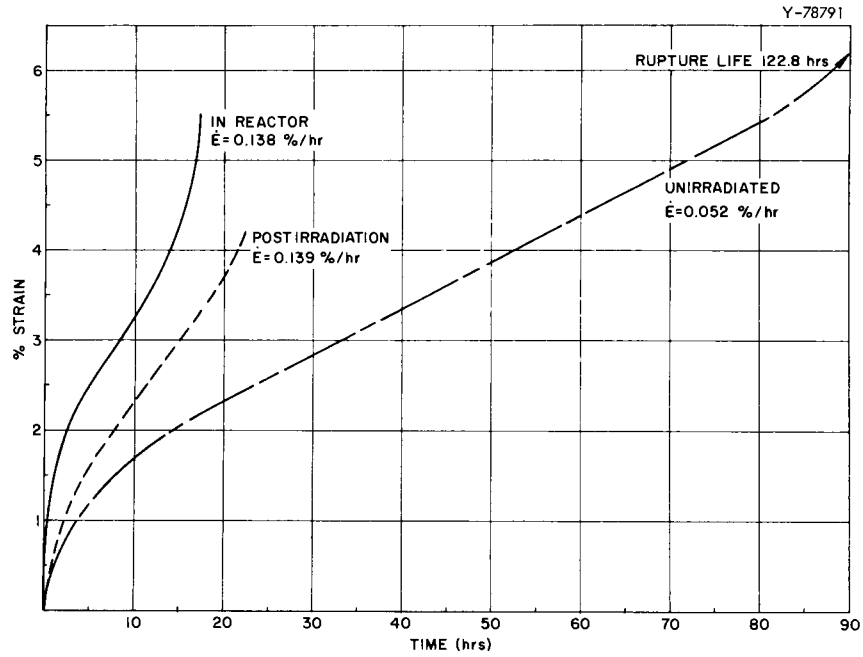

Fig. 2.1. Creep-Rupture Curves for Type 304 Stainless Steel Tested at 650°C and 25,000 psi.

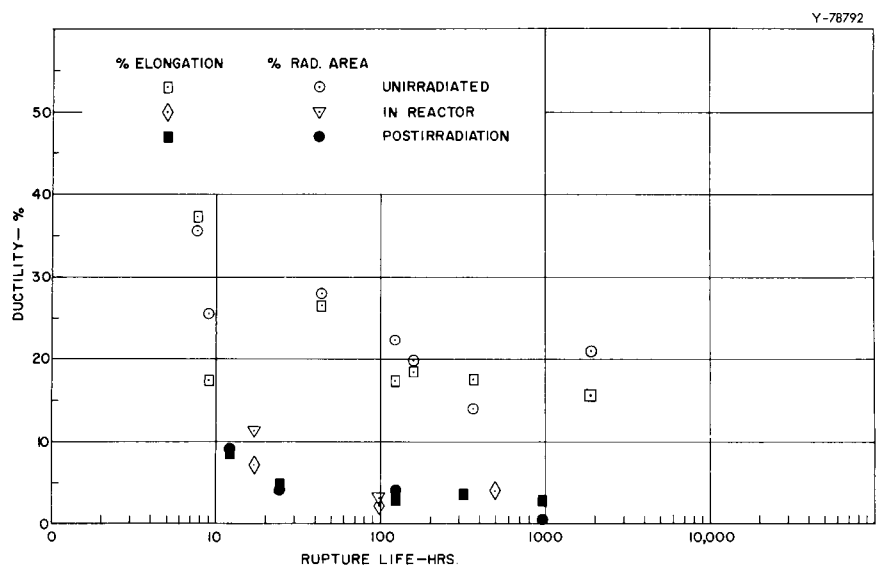

Fig. 2.2. Stress-Rupture Ductility of Type 304 Stainless Steel at 650°C.

[redacted]

[redacted]

Mechanical Properties of Type 304 Stainless Steel Containing Cyclotron-Injected Helium

R. T. King J. R. Weir, Jr.

In a previous report,[1] it was demonstrated that the presence of 0.1 ppm of cyclotron-injected helium caused significant reduction of the postbombardment tensile ductility of type 304 stainless steel. The loss of ductility occurred in samples tested at 700, 800, and 900°C at a strain rate of 0.026 min^{-1}.

Samples of the same material were prepared from 50% cold-rolled 0.010-in.-thick sheet and annealed for 1 hr in argon at 925 and 1038°C. They were bombarded in a scanning device to contain 1 ppm of helium, calculated from the measured beam current and known α-particle losses. These samples and control samples of the same material which were not bombarded have been tested in tension at 0.026 min^{-1} at 500, 600, 700, 800, and 900°C. The results of these tests are given in Table 2.2. Because no significant changes in yield stress, engineering ultimate stress, or uniform elongation were observed, only the total percent elongation to failure is reported.

[1]R. T. King, Quarterly Progress Rept.: Irradiation Effects on Reactor Structural Materials, BNWL-CC-883 (November 1966).

Table 2.2. Ductility of Type 304 Stainless Steel After Cyclotron Bombardment

Material Condition	Engineering Elongation (%) at Temperature (°C)				
	500	600	700	800	900
Annealed 1 hr at 1038°C, control	41.6	34.7	48.1	47.2	41.9
Annealed 1 hr at 1038°C, 1 ppm He	45.9	35.7	32.8	25.0	12.0
Annealed 1 hr at 925°C, control	42.1	44.3	69.6	77.2	68.6
Annealed 1 hr at 925°C, 1 ppm He	41.6	42.3	55.3	32.8	27.7

[redacted]

The results indicate that 1 ppm of uniformly dispersed helium does not affect the tensile ductility of type 304 stainless steel at 500 or 600°C. The ductility of bombarded samples is a monotonically decreasing function of test temperature in the range from 700 to 900°C. However, in this temperature range the ductility of the control sheet samples annealed for 1 hr at 925°C is significantly higher than that of control sheet samples annealed for 1 hr at 1038°C. The ductility of type 304 stainless steel containing 1 ppm of helium is higher for samples annealed for 1 hr at 925°C than for those annealed for 1 hr at 1038°C. In fact, the ratios of the ductility of bombarded samples to the ductility of control samples at a given temperature are the same for either annealing treatment to within ±0.11.

Further investigation of the microstructure of this material and comparisons with the results of neutron irradiation are in progress.

Mechanical Properties of 0.2 wt % Ti-Modified Type 304L Stainless Steel Containing Cyclotron-Injected Helium

R. T. King J. R. Weir, Jr.

The mechanical properties of a type 304L stainless steel modified with 0.2 wt % Ti have been investigated previously[1] after the injection of 0.1 ppm of helium using the Oak Ridge Isochronous Cyclotron. At this level of helium content, the tensile properties of the titanium-modified steel were not affected.

Samples of this material were prepared as before, except that intermediate anneals at 1200°C in argon were used to eliminate a second magnetic phase, presumably ferrite, from the microstructure. The material was finally cold rolled 50% to 0.010 in. thickness, samples were cut and then annealed for 1 hr at 925 and 1038°C in argon.

Control samples and samples bombarded in the scanning device to contain 1 ppm of helium were then tensile tested at 0.026 min^{-1} strain rate at 500, 600, 700, 800, and 900°C. As was the case for the type 304 stainless steel samples, the yield stress, engineering ultimate stress, and uniform elongations were not altered appreciably by the bombardment. The tensile ductilities of these samples are presented in Table 2.3.

Table 2.3. Ductility of 0.2 wt % Ti-Modified Type 304L Stainless Steel After Cyclotron Bombardment

Material Condition	Engineering Elongation (%) at Test Temperature (°C)				
	500	600	700	800	900
Annealed 1 hr at 1038°C, control	41.1	42.7	77.3	66.3	52.6
Annealed 1 hr at 1038°C, 1 ppm He	42.7	39.2	60.8	45.1	36.6
Annealed 1 hr at 925°C, control	36.3	38.7	72.4	74.7	78.1
Annealed 1 hr at 925°C, 1 ppm He	34.6	35.2	70.1	75.5	79.2

It is significant that 1 ppm of helium, uniformly dispersed in the titanium-modified steel annealed at 925°C, did not cause a decrease in the tensile ductility. However, 1 ppm of helium caused the ductilities of the samples that were annealed at 1038°C to decrease. The fractional loss of ductility of the titanium-modified type 304L stainless steel is lower at all test temperatures than that of type 304 stainless steel. These observations are in agreement with earlier data from neutron-irradiated materials.

There are several possible causes for the differences in behavior caused by different annealing treatments of this material and for the increased resistance to helium damage in this material in contrast to type 304 stainless steel.[2] Investigation of these differences is being pursued.

Electron Microscopy of Irradiated Stainless Steels

E. E. Bloom J. O. Stiegler
J. R. Weir, Jr.

Studies are continuing to determine the location and behavior of helium in irradiated stainless steels. Modified type 304L stainless steel containing 0.015 wt % C, 0.14 wt % Ti, and 0.001 to 0.0015 wt % B

[2]W. R. Martin and J. R. Weir, "Solutions to the Problems of High-Temperature Irradiation Embrittlement," paper presented at the 69th Annual Meeting of the American Society for Testing Materials, Atlantic City, N. J., June 27–July 1, 1966. To be published in the proceedings.

has been irradiated for three cycles in the B-8 position of the ORR [1.3×10^{21} neutrons/cm^2 (thermal), 1.0×10^{21} neutrons/cm^2 (E > 1 Mev)] at temperatures of 650 and 800°C. The calculated helium concentration in the irradiated alloy is 15×10^{-6} atom fraction. To date we have examined samples in the as-irradiated condition for the 800°C irradiation temperature. The irradiation temperature was above the solubility limit for carbon in the alloy and thus only a few precipitates were present. Helium bubbles as shown in Fig. 2.3 were found in several isolated areas of the irradiated samples. In the areas in which bubbles were found several important features were noted:

1. Bubbles that are present in the grain boundary are several times larger than those present within the matrix.

2. A necklace of bubbles is present along the triple-grain junction located in the lower left-hand corner of the figure. Since this boundary extends from the top of the foil to the bottom, the light circular regions must be bubbles that lie within the foil and cannot be a polishing effect on the surface.

3. Clusters of bubbles are attached to the surface of precipitates present within the matrix.

4. In several instances, the bubbles have a polyhedral shape, suggesting that equilibrium between surface tension and internal gas pressure is being approached. This is suggested by contrast variations in the large bubbles lying in the grain boundary of Fig. 2.3.

MSRE Surveillance Program — Hastelloy N

H. E. McCoy, Jr.

Several stringers of Hastelloy N test specimens were located in an axial position near the center line of the MSRE for surveillance purposes. These specimens were from heats 5085 (cylindrical vessel) and 5081 (miscellaneous parts). They were removed after 4800 hr at 645 ± 10°C during which the reactor had operated 7612 Mwhr. The peak thermal dose was 1.3×10^{20} neutrons/cm^2 and the peak fast dose (> 1.2 Mev) was 3×10^{19} neutrons/cm^2. The peak-to-minimum thermal flux over the length

OFFICIAL USE ONLY

Fig. 2.3. Type 304L Stainless Steel Containing 0.14 wt % Ti, Irradiated at 800°C, Containing 15×10^{-6} Atom Fraction Helium. 30,000×.

OFFICIAL USE ONLY

[redacted]

of the test specimen array was a factor of 5, but this was not found to be a significant variable in this evaluation. The surveillance control specimens were exposed to MSRE-type fuel salt and duplicated the thermal history of the in-reactor specimens.

Samples of both reactor and control specimens were examined metallographically. No evidence of attack or deposition was found within the gage lengths of any of the samples. However, all test specimens from heat 5085 (both irradiated and control) were found to have a surface layer on the 1/4-in.-diam portion of the samples on the sides that were in contact or near contact with the graphite. Such layers were not found on the smaller 1/8-in.-diam gage length of the specimens that were separated from the graphite by 1/16 in. Figure 2.4 shows the nature of

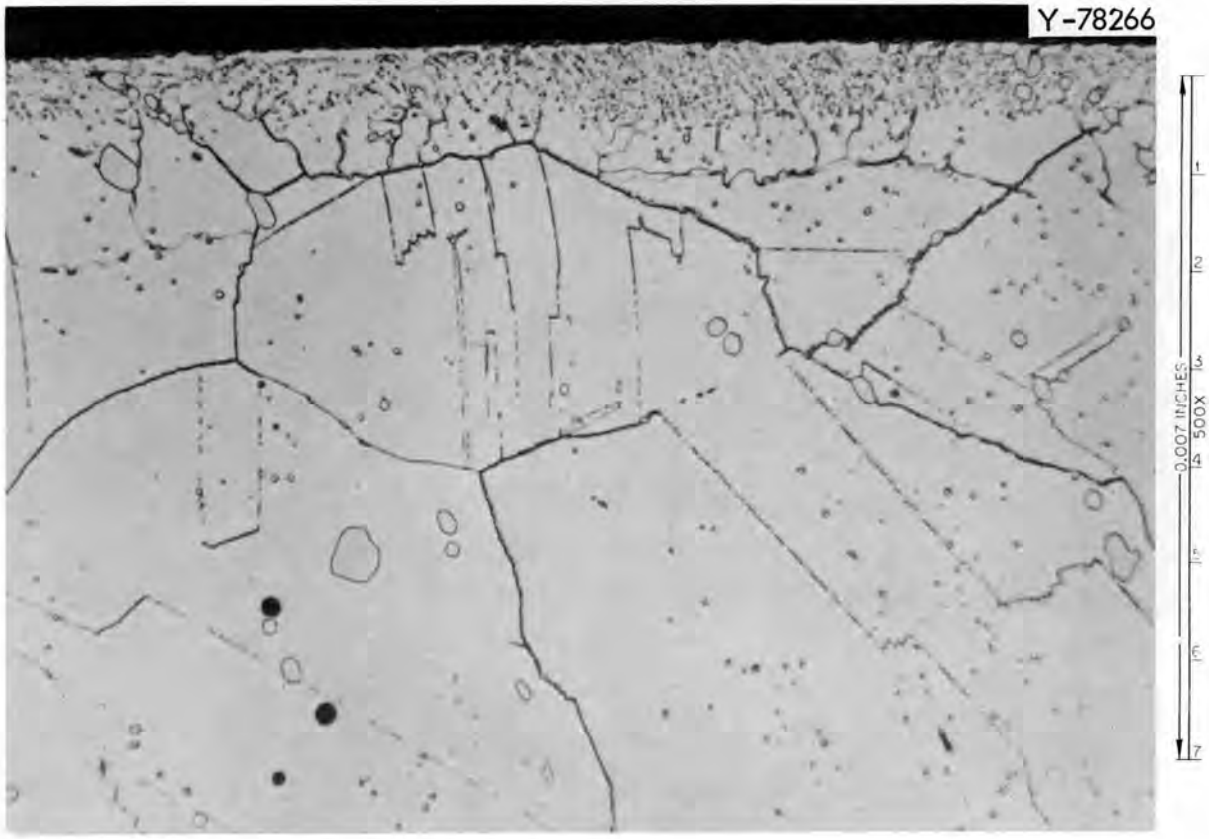

Fig. 2.4. Edge of Hastelloy N (heat 5085) Specimen Exposed to Molten Salt for 4800 hr at 650°C. Surface in intimate contact with graphite. Etchant: Glyceria regia.

[redacted]

the surface layer on these samples. Electron microprobe studies showed that the carbon content near the edge of the sample was from 0.3 to 0.5 wt % higher than the interior of the sample.

Both tensile and creep-rupture tests have been conducted on the surveillance specimens. The creep-rupture testing is not yet complete, so only the results of the tensile tests will be reported. The tensile results are given in Table 2.4.

The total elongation at fracture when deformed at a strain rate of 0.05 min^{-1} is shown as a function of temperature in Fig. 2.5. Both heats show some reduction in ductility in the irradiated condition with a greater reduction being observed for heat 5085. At temperatures above 500°C, the ductility of the irradiated and the control material decreases with increasing temperature, with the irradiated material showing a greater loss in ductility. At temperatures above 650 to 700°C, the control material exhibits improved ductility, whereas the ductility of the irradiated material continues to decrease.

Figure 2.6 compares the properties of the irradiated and control specimens at a lower strain rate, 0.002 min^{-1}. Qualitatively, the behavior is very similar to that noted at a strain rate of 0.05 min^{-1}. However, the loss in ductility is magnified at the lower strain rate. The variations in the properties of the two heats of material are minimal.

Figures 2.7 and 2.8 show how the ratio of the irradiated to the unirradiated tensile property varies for heats 5081 and 5085, respectively, as a function of temperature. For both heats, the yield strength is unchanged by irradiation. The ultimate tensile stress is reduced about 8% up to a temperature of about 500°C where the reduction becomes considerably greater. The reduction in ductility at room temperature and at elevated temperatures is also clearly demonstrated.

We have compared the irradiated and control surveillance specimens. Let us now look at how the properties of the control specimens have changed during their 4800 hr of thermal exposure to molten salt. Table 2.5 shows representative properties of heat 5085 after several different heat treatments. The first group of tests was run with the material in the as-received condition (mill annealed 1 hr at 1177°C). Annealing for 600 hr

Table 2.4. Postirradiation Tensile Properties of Several Heats of MSRE Hastelloy N After Irradiation in a Helium Environment

Heat No.	Condition	Boron Level (ppm)	Experiment No.	Irradiation Temp (°C)	*nvt*, Thermal Dose	Test Temp (°C)	$\dot{\epsilon}$	Yield Stress (psi)	Ultimate Stress (psi)	Uniform Elongation (%)	Total Elongation (%)	Reduction in Area (%)	Specimen No.
					$\times 10^{20}$								
5065	A.R.	20	ORR-149	43	8.5	25	0.05	102,900	135,100	31.5	35.5	52.0	570
5065	A.R.	20	ORR-149	43	8.5	200	0.05	82,300	119,600	36.1	39.2	54.8	571
5065	A.R.	20	ORR-149	43	8.5	650	0.05	44,600	76,600	26.3	27.3	24.5	572
5065	A.R.	20	ORR-149	43	8.5	650	0.002	40,800	57,400	12.2	13.1	21.9	574
5065	A.R.	20	ORR-149	43	8.5	871	0.05	33,500	36,400	1.7	1.8	3.25	573
5065	A.R.	20	ORR-149	43	8.5	871	0.002	23,200	23,400	0.9	1.8	6.07	575
5065	8 hr at 871°C	20	ORR-149	43	8.5	25	0.05	101,500	132,200	30.0	33.6	55.2	581
5065		20	ORR-149	43	8.5	200	0.05	78,600	118,300	37.3	39.8	45.9	582
5065		20	ORR-149	43	8.5	650	0.05	35,100	77,700	25.3	25.8	22.6	583
5065		20	ORR-149	43	8.5	650	0.002	38,100	66,200	13.7	14.3	17.3	585
5065		20	ORR-149	43	8.5	871	0.05	37,100	38,500	1.7	1.9	2.94	584
5065		20	ORR-149	43	8.5	871	0.002	25,900	25,900	0.8	1.6	5.26	586
5067	A.R.	20	ORR-155	500–700	1.4	25	0.05	59,000	123,700	49.4	51.2	45.4	2289
5067	A.R.	20	ORR-155	500–700	1.4	650	0.05	38,400	66,800	14.0	14.0	20.5	2290
5067	A.R.	20	ORR-155	500–700	1.4	650	0.002	36,400	59,900	9.6	9.6	16.0	2291
5085	A.R.	38	ORR-155	500–700	1.4	25	0.05	46,300	110,600	41.1	41.2	40.3	2285
5085	A.R.	38	ORR-155	500–700	1.4	650	0.05	30,800	64,400	18.0	21.2	19.1	2286
5085	A.R.	38	ORR-155	500–700	1.4	650	0.002	30,200	51,800	9.3	9.9	15.4	2287
5065	A.R.	20	ORR-155	500–700	1.4	25	0.05	50,100	117,000	54.4	56.1	53.2	1857
5065	A.R.	20	ORR-155	500–700	1.4	650	0.05	37,400	62,100	12.3	12.4	17.2	1858
5065	A.R.	20	ORR-155	500–700	1.4	650	0.002	34,800	49,100	6.4	6.5	15.3	1859
5065	A.R.	20	ETR-41-31	600 ± 100	3.5	550	0.002	49,100	68,600	9.1	9.4		1273
5065	A.R.	20	ETR-41-31	600 ± 100	3.5	600	0.002	42,200	56,300	8.2	8.5		1276
5065	A.R.	20	ETR-41-31	600 ± 100	3.5	650	0.05	41,200	59,000	10.8	11.3		1270
5065	A.R.	20	ETR-41-31	600 ± 100	3.5	650	0.002	42,600	51,800	5.9	6.1		1271
5065	A.R.	20	ETR-41-31	600 ± 100	3.5	760	0.002	41,900	46,000	2.8	2.8		1274
5065	A.R.	20	ETR-41-30	<150	5	650	0.05	46,700	76,200	21.6	22.2	28.8	383
5065	A.R.	20	ETR-41-30	<150	5	650	0.002	37,700	53,300	9.3	10.0	10.1	380
5065	A.R.	20	ETR-41-30	<150	5	650	0.002	40,000	57,500	11.4	11.6	17.5	384

[redacted]

ORNL-DWG 67-2452

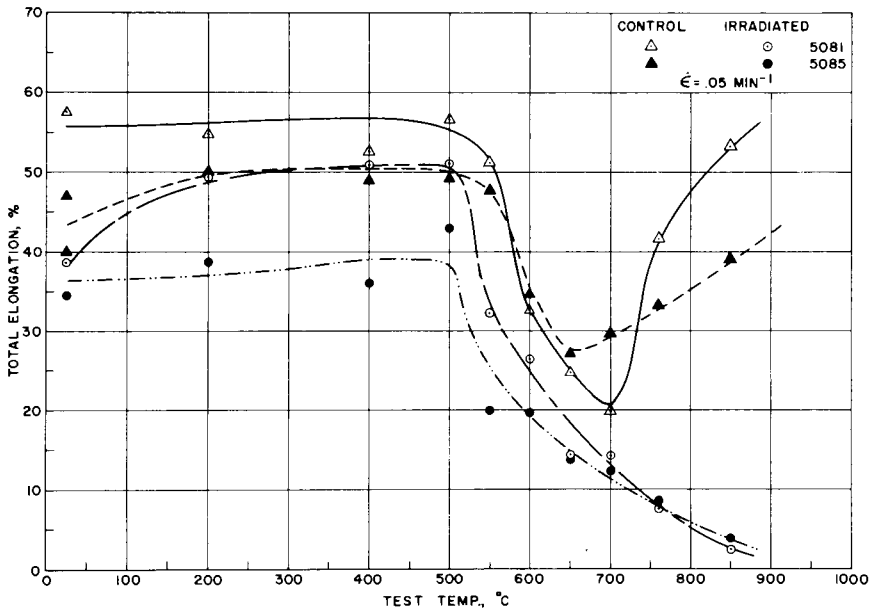

Fig. 2.5. Comparative Tensile Ductilities of MSRE Surveillance Specimens and Their Controls at a Strain Rate of 0.05 min^{-1}.

ORNL-DWG 67-2453

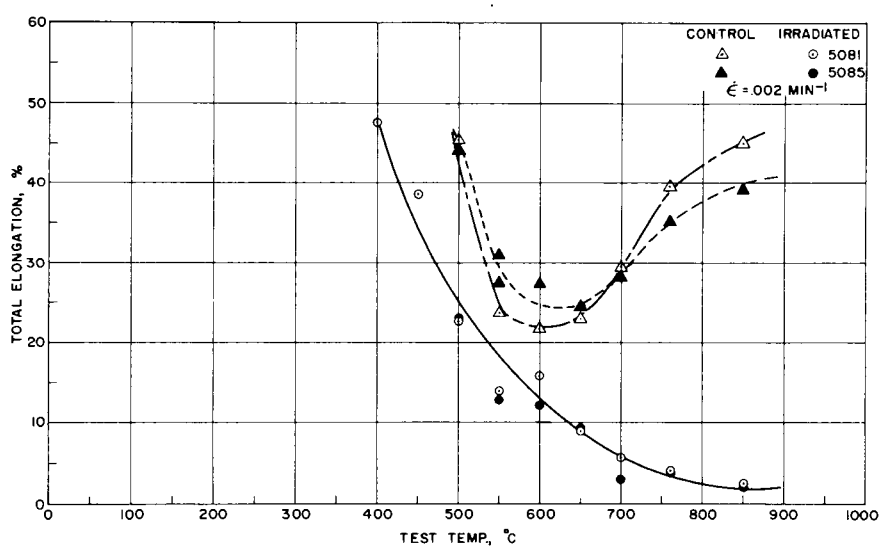

Fig. 2.6. Comparative Tensile Ductilities of MSRE Surveillance Specimens and Their Controls at a Strain Rate of 0.002 min^{-1}.

[redacted]

[redacted]

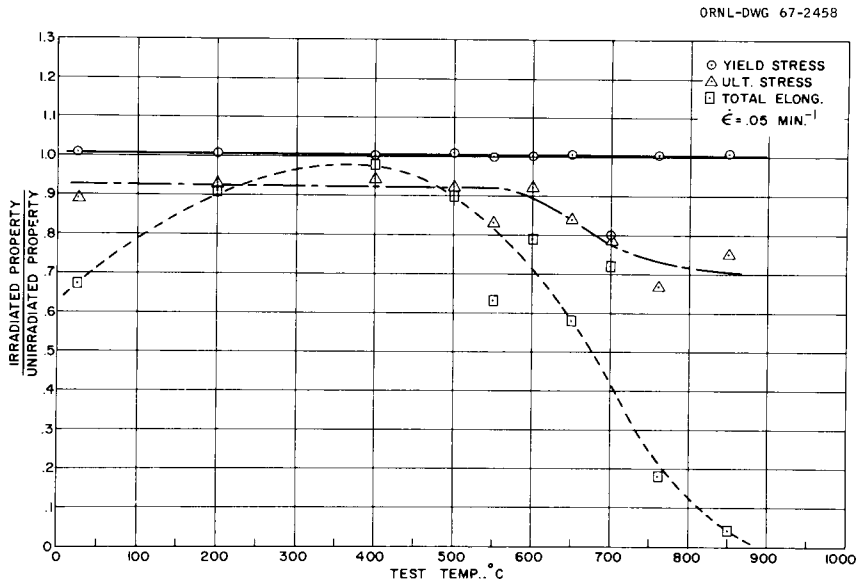

Fig. 2.7. Comparative Tensile Properties of Irradiated and Unirradiated MSRE Surveillance Specimens, Heat 5081.

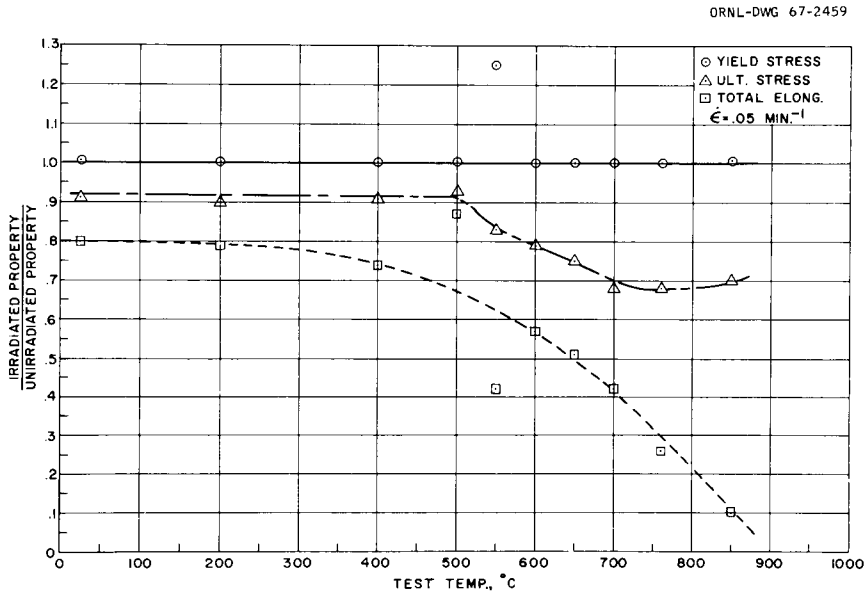

Fig. 2.8. Comparative Tensile Properties of Irradiated and Unirradiated MSRE Surveillance Specimens. Heat 5085.

[redacted]

[redacted]

Table 2.5. Tensile Properties of Hastelloy N — Heat 5085

Specimen No.	Heat Treatment	Test Temp (°C)	Strain Rate (min^{-1})	Yield Stress (psi)	Ultimate Stress (psi)	Uniform Elongation (%)	Total Elongation (%)	Reduction in Area (%)
76	As received	25	0.05	52,200	116,400	51.3	52.5	56.3
77	As received	427	0.05	30,700	102,900	57.6	59.4	49.9
284	As received	600	0.02	32,200	85,100	46.6	47.6	40.4
78	As received	650	0.05	28,700	80,700	35.5	36.7	33.2
285	As received	650	0.02	31,900	65,000	25.8	31.8	27.2
283	As received	650	0.002	30,500	64,300	22.6	24.1	28.8
79	As received	760	0.05	32,100	61,500	24.7	27.0	31.9
80	As received	871	0.05	30,700	42,300	9.0	31.8	33.4
81	As received	982	0.05	23,100	23,100	1.8	40.2	43.9
1339	A.R. + 600 hr at 650°C	25	0.05	41,100	115,700	52.5	52.8	41.7
1340	A.R. + 600 hr at 650°C	650	0.05	33,800	76,000	36.8	37.5	36.4
4295	A.R. + 2 hr at 900°C	25	0.05	41,500	120,800	52.3	53.1	42.2
4298	A.R. + 2 hr at 900°C	500	0.05	32,600	94,800	51.2	54.1	40.9
4299	A.R. + 2 hr at 900°C	500	0.002	33,500	100,200	52.0	53.3	41.7
4296	A.R. + 2 hr at 900°C	650	0.05	29,600	75,800	31.7	33.7	34.6
FC-3	A.R. + 2 hr at 900°C + 4800 hr in MSRE salt at 650°C	25	0.05	45,500	111,200	46.8	46.8	31.5
DC-19		500	0.05	33,600	94,300	48.8	49.3	41.5
DC-26		500	0.002	33,400	91,700	43.3	44.3	37.8
DC-14		650	0.05	31,800	70,100	25.8	26.8	30.0
DC-25		650	0.002	31,500	62,500	22.8	24.3	27.2

at 650°C had no appreciable effects on the properties. The MSRE surveillance specimens were given a 2-hr anneal at 900°C before insertion into the reactor and the properties of the material in this state are also indicated in Table 2.5. The properties at 25°C were unchanged and slight reductions in tensile strength and ductility were noted at a test temperature of 650°C. After exposure to salt for 4800 hr at 650°C, there is a further reduction of 10% in the tensile strength and the ductility. Table 2.6 shows that heat 5081 underwent similar changes at elevated temperatures, but did not suffer the reduction in ductility at 25°C noted for heat 5085.

Some of the test specimens have been examined metallographically. Figure 2.9 shows the microstructure of control specimen AC-8 from heat 5081 that was tested at 25°C. This specimen exhibited good ductility and this is reflected in the intragranular, shear-type fracture and

[redacted]

Table 2.6. Tensile Properties of Hastelloy N — Heat 5081

Specimen No.	Heat Treatment	Test Temp (°C)	Strain Rate (min^{-1})	Yield Stress (psi)	Ultimate Stress (psi)	Uniform Elongation (%)	Total Elongation (%)	Reduction in Area (%)
4300	A.R. + 2 hr at 900°C	25	0.05	52,600	125,300	56.7	59.5	50.5
4303	A.R. + 2 hr at 900°C	500	0.05	32,000	100,300	57.8	60.7	44.4
4301	A.R. + 2 hr at 900°C	650	0.05	32,200	81,800	31.7	33.9	29.9
4302	A.R. + 2 hr at 900°C	650	0.002	32,900	74,900	29.0	29.5	31.8
AC-8	A.R. + 2 hr at 900°C + 4800 hr in MSRE salt at 650°C	25	0.05	47,700	118,700	55.9	57.6	48.8
AC-19		500	0.05	35,800	97,800	53.6	56.6	46.2
BC-9		500	0.002	36,200	95,300	46.2	47.0	38.1
AC-27		650	0.05	32,400	68,400	23.8	24.6	23.1
AC-17		650	0.002	33,600	66,700	22.8	23.2	21.6

the lack of intergranular cracking. Figure 2.10 shows the irradiated specimen from the same heat that was tested at 25°C. The fracture is largely intergranular and there are numerous intergranular cracks. The control and irradiated specimens from heat 5085 tested at 25°C exhibited the same general characteristics as those illustrated in Fig. 2.10. The other specimens examined were tested at 650°C. The failures were all intergranular with the irradiated specimens exhibiting the typical characteristics of a high-temperature, low-ductility, intergranular fracture.

We compared the ductilities of the surveillance specimens with those for specimens irradiated in other experiments without salt present. Heat 5081 had been irradiated previously in the ORR.[3] The ORR experiment was run at 700°C to a thermal dose of 9×10^{20} neutrons/cm^2 and the material was in the as-received condition. The MSRE surveillance specimens were run at 650°C to a thermal dose of 1.3×10^{20} neutrons/cm^2 and the preirradiation anneal was different. However, none of these differences are thought to be particularly significant and the results compare rather well. Figure 2.11 shows that the postirradiation ductilities of heat 5081 after both experiments are very similar.

[3]W. R. Martin and J. R. Weir, "Effect of Elevated-Temperature Irradiation on Hastelloy N," Nucl. Appl. 1(2), 160–167 (1965).

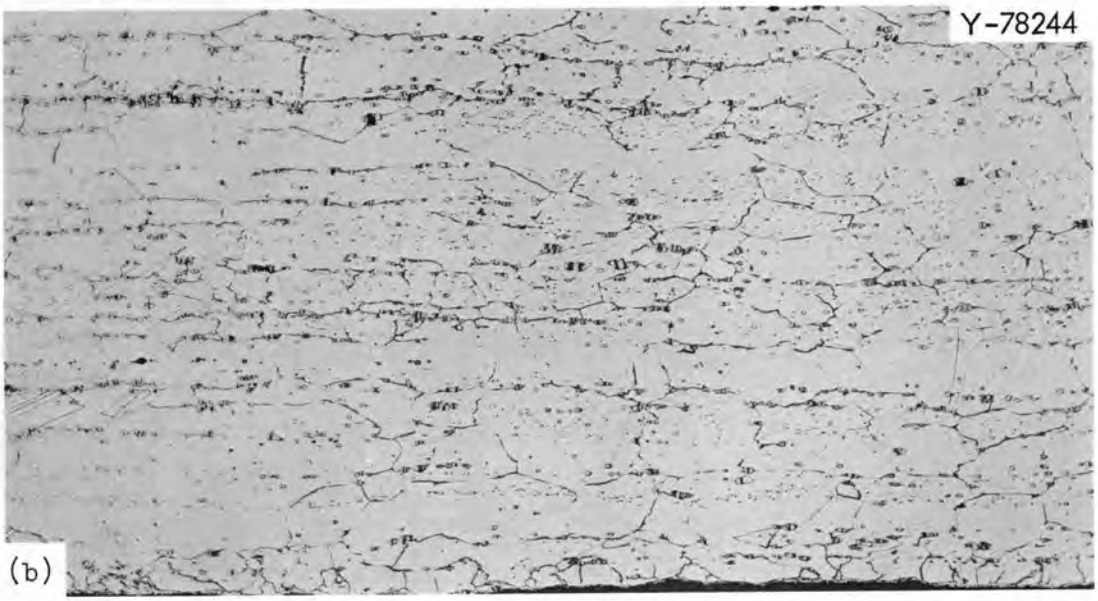

Fig. 2.9. Microstructure of Hastelloy N (Heat 5081) Exposed to Salt for 4800 hr at 650°C. Tested at 25°C at a strain rate of 0.05 min^{-1}. Etchant: glyceria regia. (a) Fracture. (b) Edge about 1/2 in. from fracture.

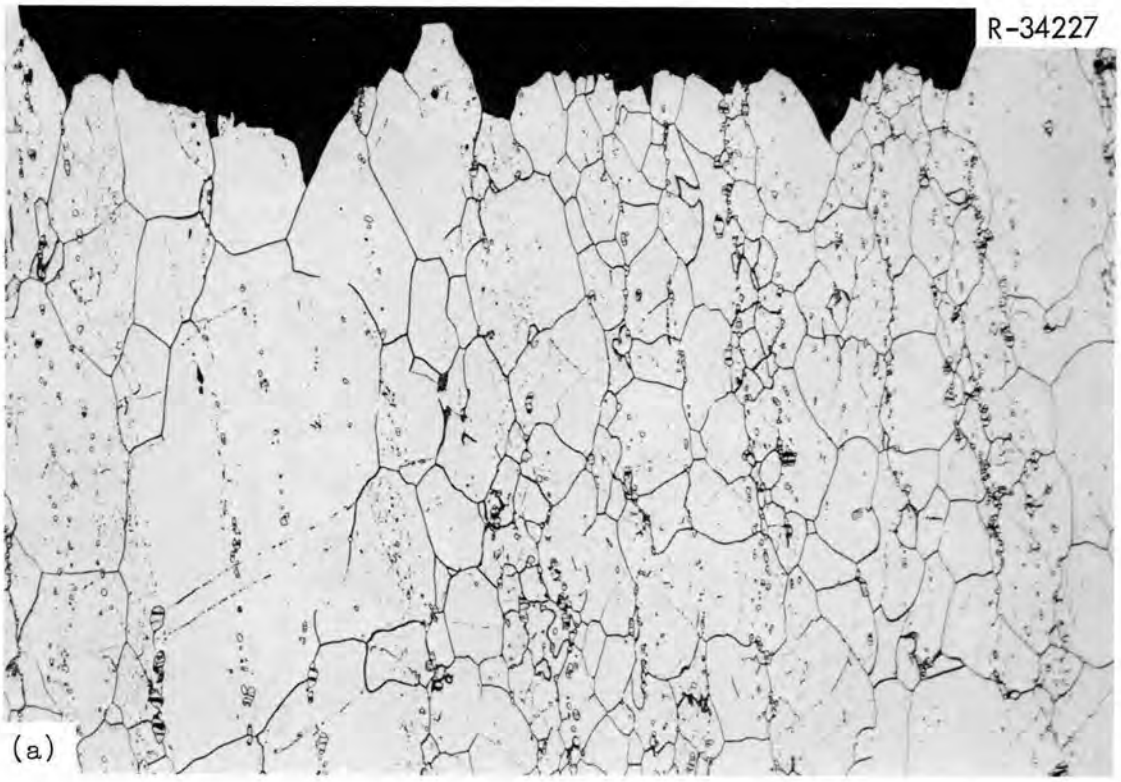

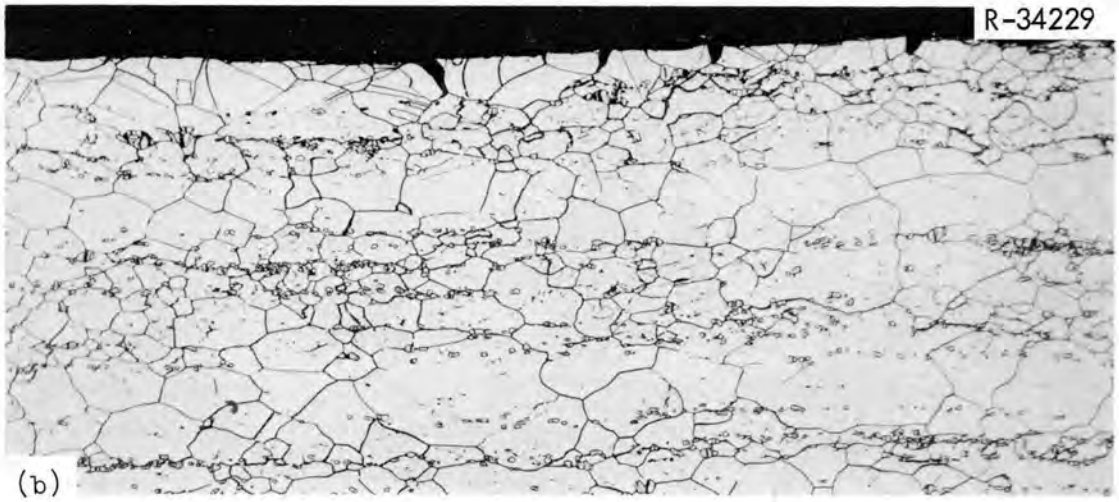

Fig. 2.10. Microstructure of Hastelloy N (Heat 5081) Exposed for 4800 hr in the MSRE at 650°C. Tested at 25°C at a strain rate of 0.05 min^{-1}. (Specimen D-16) Etchant: glyceria regia. 100×. (a) Fracture. (b) Edge about 1/2 in. from fracture.

[redacted]

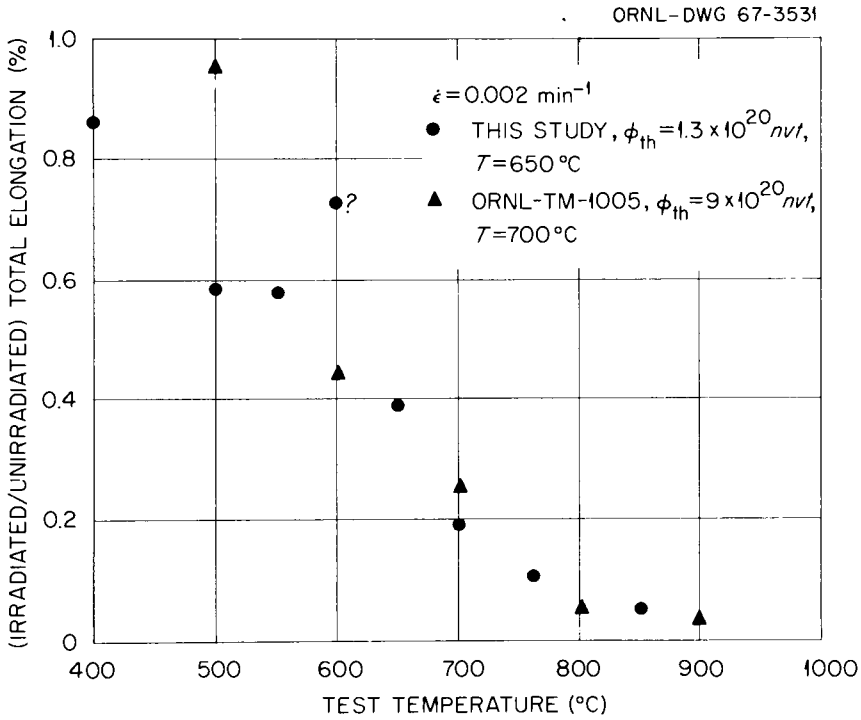

Fig. 2.11. Comparative Effects of Irradiation in MSRE and ORR on the Ductility of Hastelloy N — Heat 5081.

Measurement of the Nuclear Heating Rate in EBR-II

E. E. Bloom A. F. Zulliger[4]
J. R. Weir, Jr.

An experiment has been designed and constructed to measure the axial distribution of nuclear heating in nonfissionable materials in row 2 and row 7 positions of the EBR-II. These positions are representative of those to be used in subsequent ORNL materials irradiations. Nuclear heat susceptors, shown schematically in Fig. 2.12, will be placed in the central pin of Mark B-7 subassemblies. The gas composition, gas size, and susceptor material were selected on the basis of heat transfer calculations performed on an IBM system 360 computer. The code for determining susceptor temperature includes radial heat transfer from the susceptor by conduction and radiation and accounts for axial conduction losses through the specimen and support pins. Thermal conductivity, susceptor dimensions, and emissivity values as a function of

[4]General Engineering and Construction Division.

[redacted]

ORNL-DWG 67-5928

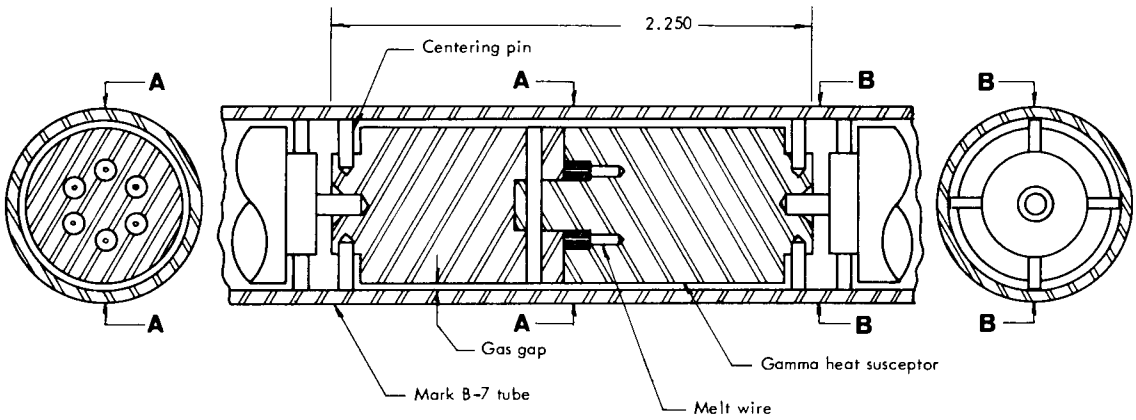

Fig. 2.12. Schematic of Gamma Heat Susceptor.

temperature are incorporated into the program. Susceptors were designed on the basis of published heat rates to produce susceptor center-line temperatures between 500 and 800°C. Melt wires having melting points both above and below the design temperature (to cover the range of ±50% of the published heating rate) were placed in each susceptor as shown in the photograph in Fig. 2.13. The irradiation will consist of bringing the reactor to the desired power level followed by an irradiation time of approximately 24 hr. Postirradiation examination will place the actual operating temperature between a lower value (determined by the melt wire of highest melting point that has melted) and an upper value (determined by the melt wire of lowest melting point that has not melted). It will then be possible, through calculations based on temperature and susceptor dimensions, to calculate the nuclear heating rate of ±10%. The results of this experiment will allow subsequent materials irradiations to be conducted at ±25°C of the desired irradiation temperature when a susceptor of identical design but containing mechanical properties test specimens is used. Figure 2.14 is a schematic diagram of the specimen holder.

OFFICIAL USE ONLY

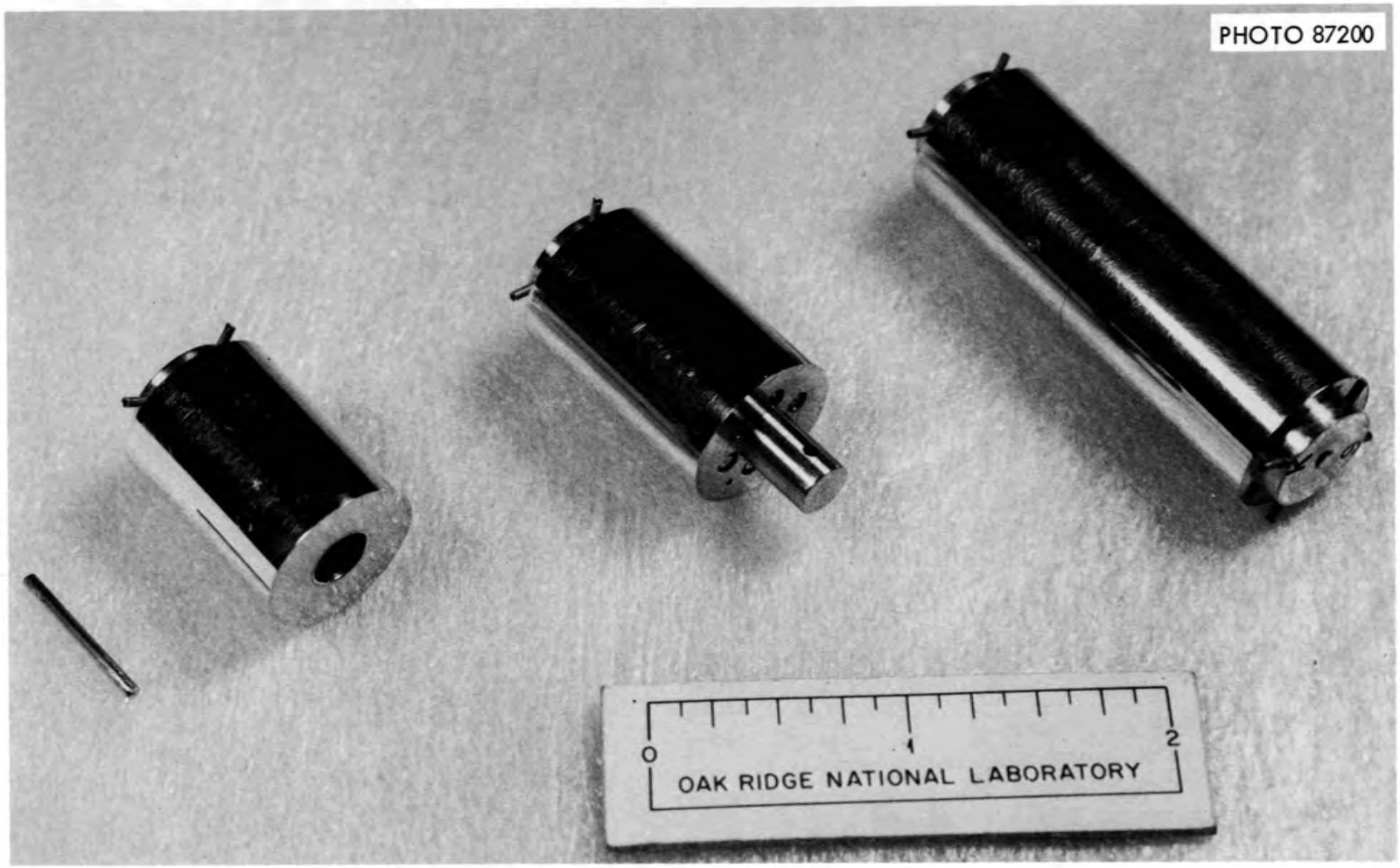

Fig. 2.13. Photograph of Nuclear Heating Susceptor.

OFFICIAL USE ONLY

ORNL-DWG 67-5927

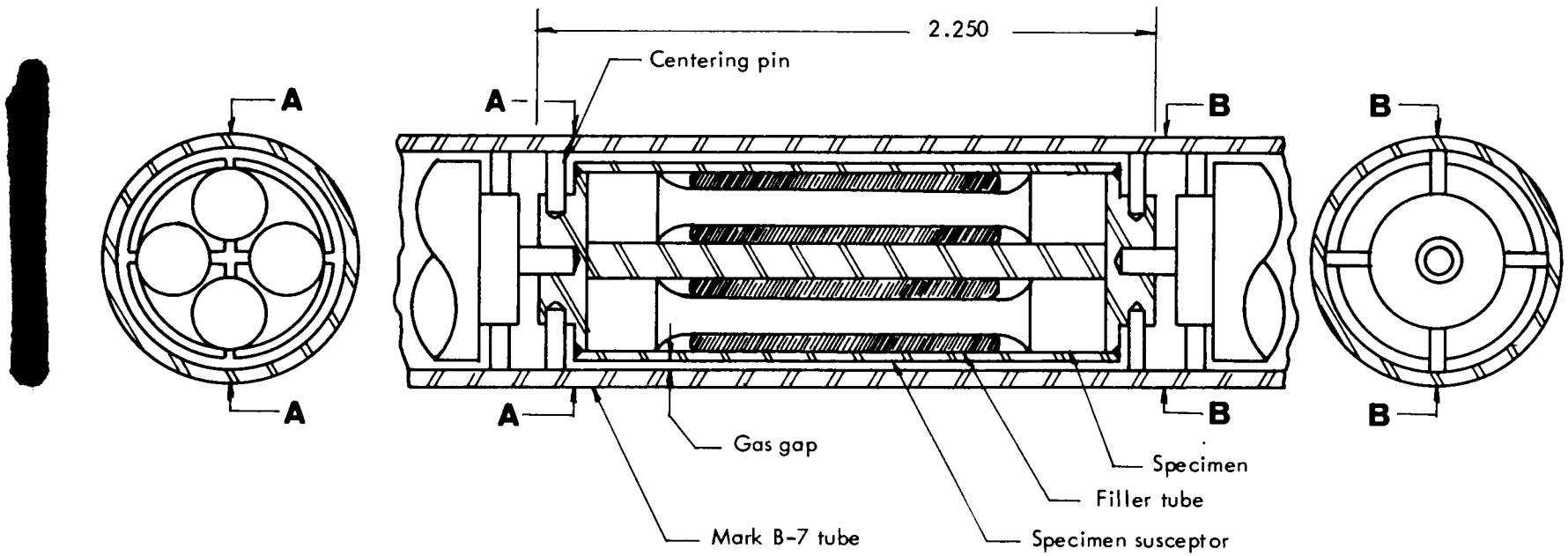

Fig. 2.14. Schematic of Specimen Holder.

[redacted]

A second objective of this experiment is to measure the axial neutron flux distribution in the row 2 and row 7 subassemblies. One tube of the row 2 and one tube of the row 7 subassembly are being used for this purpose. Titanium, iron, nickel, and cobalt flux monitors are being used.

A third objective is to determine the combined effects of fast neutron flux and irradiation temperature upon the dynamic recovery of lattice displacement damage. Type 304 stainless steel and high-purity nickel will be irradiated at temperatures between ambient sodium and 650°C at neutron fluxes between 3×10^{15} neutrons cm^{-2} sec^{-1} (axial mid-plane row 2) and 2×10^{13} neutrons cm^{-2} sec^{-1} (axial extreme row 7). Postirradiation examination will consist of hardness measurements and electron microscopy studies to determine the effect of irradiation temperature upon the recovery of irradiation-induced displacement damage.

[redacted]

3. NONDESTRUCTIVE TEST DEVELOPMENT

R. W. McClung

This program is intended to develop new and improved methods of nondestructively evaluating reactor materials and components. To achieve this we are studying various physical phenomena, developing instrumentation and other equipment, devising application techniques, and designing and fabricating reference standards. Among the methods being actively pursued are electromagnetics (with major emphasis on eddy currents), ultrasonics, and penetrating radiation. These and other methods are being evaluated for both normal and remote inspection.

Electromagnetic Test Methods

C. V. Dodd

Analytical Studies

We have continued research and development on both analytical and empirical bases. We have obtained a "closed form" solution of the vector potential for the case of a rectangular coil above one conductor clad on another, and for the case of a rectangular coil encircling a rod clad with another conductor. The solution in both cases is in terms of integrals of Bessel functions. We are now attempting to approximate and evaluate these integrals.

A report[1] based on the relaxation technique has been prepared and released. It will be useful in solving problems related to magna forming, induction pumping, and ultrasonic pulses generated by eddy-current forces. The abstract is presented below.

> Relaxation averaging formulae are derived for magnetic induction problems involving axially symmetric fields with sinusoidal or pulsed time dependence in media which may be linear or nonlinear, homogeneous, or inhomogeneous. Solutions have been

[1]C. V. Dodd and W. E. Deeds, Electromagnetic Forces in Conductors, ORNL-TM-1835 (May 1967).

obtained from a high-speed digital computer for time-harmonic fields in linear, inhomogeneous media. From these solutions, the electromagnetic forces are calculated and compared with experimental measurements. It is found that the computed and measured values agree quite well and that most of the discrepancy can be explained by the fact that the permeability of the ferrite used in the measurements was different from that assumed in the calculations.

Phase-Sensitive Eddy-Current Instrument

The temperature stability of the phase-sensitive eddy-current instrument has been improved considerably. The temperature drift of the instrument and the coils has been stabilized separately over a temperature range from −17 to +55°C. At 50 kilohertz the temperature drift corresponds to a conductivity change of 0.3%/°C.

A series of measurements has been made for various metal thicknesses and at various conductivities to demonstrate the sensitivity of the instrument.

A more complete set of construction details has been prepared, including coil construction details, and sent to the ORNL Office of Industrial Cooperation for external distribution.

Ultrasonic Test Methods

K. V. Cook

Fabrication of Reference Notches

We are continuing to work on the problems encountered in tubing inspection by ultrasonic methods. A major problem is the establishment of realistic ultrasonic notch standards for calibration. Since electrical-discharge machining (EDM) appears to be a reliable method for making both inner- and outer-surface notches, we are continuing our notch fabrication studies.

The transverse electrode arms mentioned previously,[2] in addition to a third arm which allows the machining of transverse notches with

[2]K. V. Cook, Fuels and Materials Development Program Quart. Progr. Rept. Mar. 31, 1967, ORNL-TM-1825, pp. 20–21.

1/32-in. lengths, have been used to generate calibration curves for type 304 stainless steel. The minimum inner diameter in which we have placed the 1/32-in.-long transverse notches is 0.210 in.; however, we feel that the limit will approach an inner diameter value of approximately 0.180 in.

Reference Standards

We have initiated a study that will attempt to correlate ultrasonic response from EDM notches, drilled holes, and flat-bottomed holes of various sizes machined in thin materials. At the present time, we are working with sheet material, and we plan to make a similar study with small-diameter tubing.

A previous report[3] briefly described the aluminum and stainless steel sheets and the reference discontinuities machined in them. Our last report[2] indicated that data had been generated which related the incident angle of the ultrasonic beam to the amplitude of the reflected ultrasonic energy from the reference discontinuities. Further evaluation of this method for compiling data revealed that the general shape of the curves being generated varied simply by changing from one ultrasonic instrument to another, even though the instruments were of the same type and basic design. This condition may be caused by variations in the amplifier characteristics of the different instruments. Regardless of the cause, we demonstrated that most of the variations could be deleted by incorporating into the system a decibel attenuator and then relating incident angle and the decibel insertion necessary to produce an indication having a constant reproducible amplitude. A standard, 1/4-in. cone collimator was employed for the preliminary data. In addition, we are also generating the same type of data using a focused transducer and a collimator normally employed for tubing inspection.

---

[3]K. V. Cook, Fuels and Materials Development Program Quart. Progr. Rept. Dec. 31, 1966, ORNL-TM-1720, pp. 30–31.

[redacted]

Optical Visualization of Ultrasound (K. V. Cook, H. L. Whaley)

A paper[4] summarizing work with our optical system was presented at the Fifth International Conference on Nondestructive Testing. The abstract is given below:

> The schlieren and photoelastic methods for viewing continuous and pulsed ultrasonic waves propagating in transparent media were investigated. Limitations, possible applications, and results of the investigation of each system are discussed. Emphasis is placed on equipment improvements for the development of optimum systems for nondestructive testing applications.

Penetrating Radiation Methods

R. W. McClung

We continued our quantitative studies for the low-voltage radiography of graphite in thicknesses from 0.100 to 1.650 in. The principal activities were evaluation of exposure data, generation of comprehensive exposure charts, and calculations to determine optimum operational conditions. Figure 3.1 is a graph relating x-ray energy (kvp) to exposure factor (milliampere-sec) for various thicknesses of graphite and both helium and air atmospheres. Figure 3.2 displays the conditions under which a 10% change in exposure requirement will be achieved by removal of the specified absorber.

---

[4]H. L. Whaley, K. V. Cook, R. W. McClung, and L. S. Snyders, "Optical Methods for Studying Ultrasonic Propagation in Transparent Media," paper presented at the 5th International Conference on Nondestructive Testing held May 21–26, 1967, in Montreal, Canada. To be published in the proceedings.

[redacted]

[redacted]

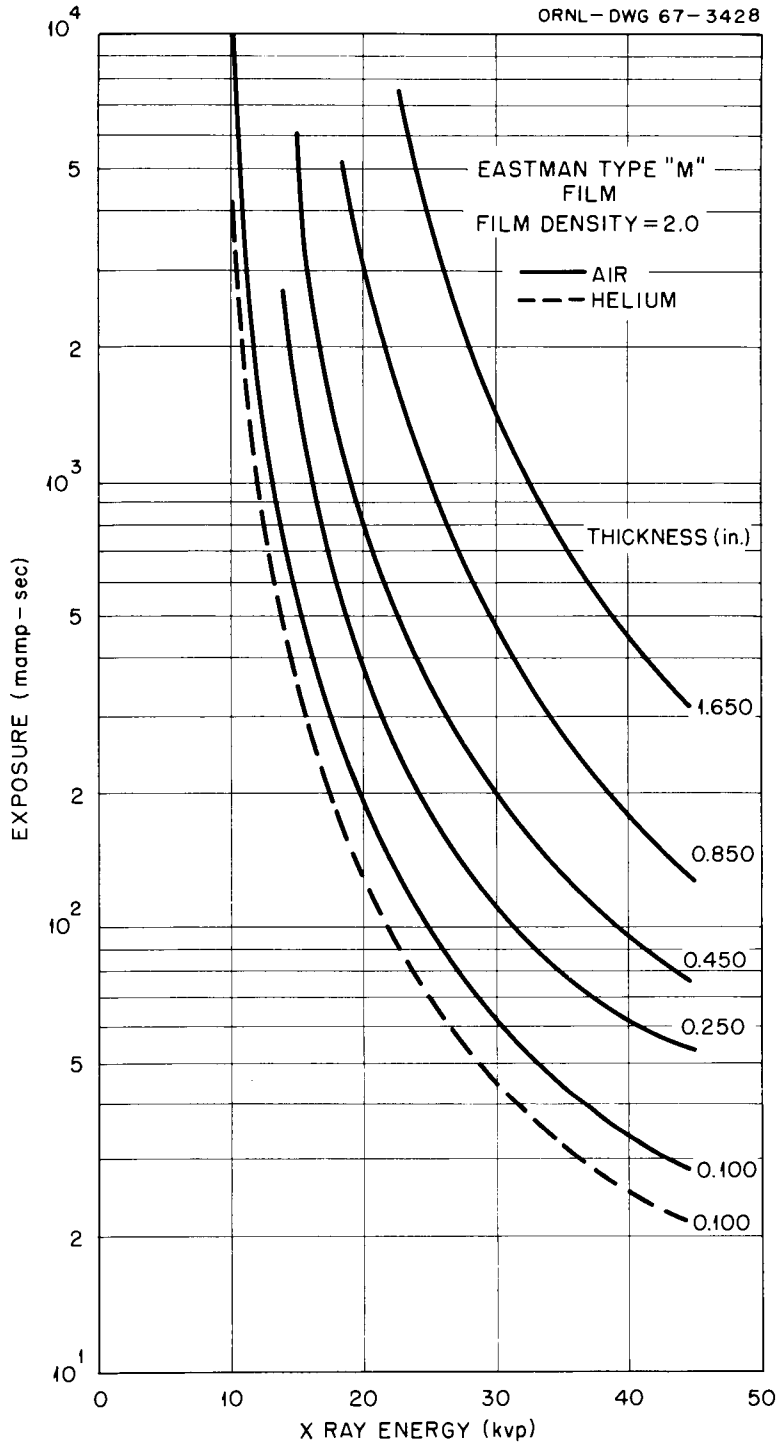

Fig. 3.1. Exposure Chart for Various Thicknesses of Graphite with Air and Helium.

[redacted]

[redacted]

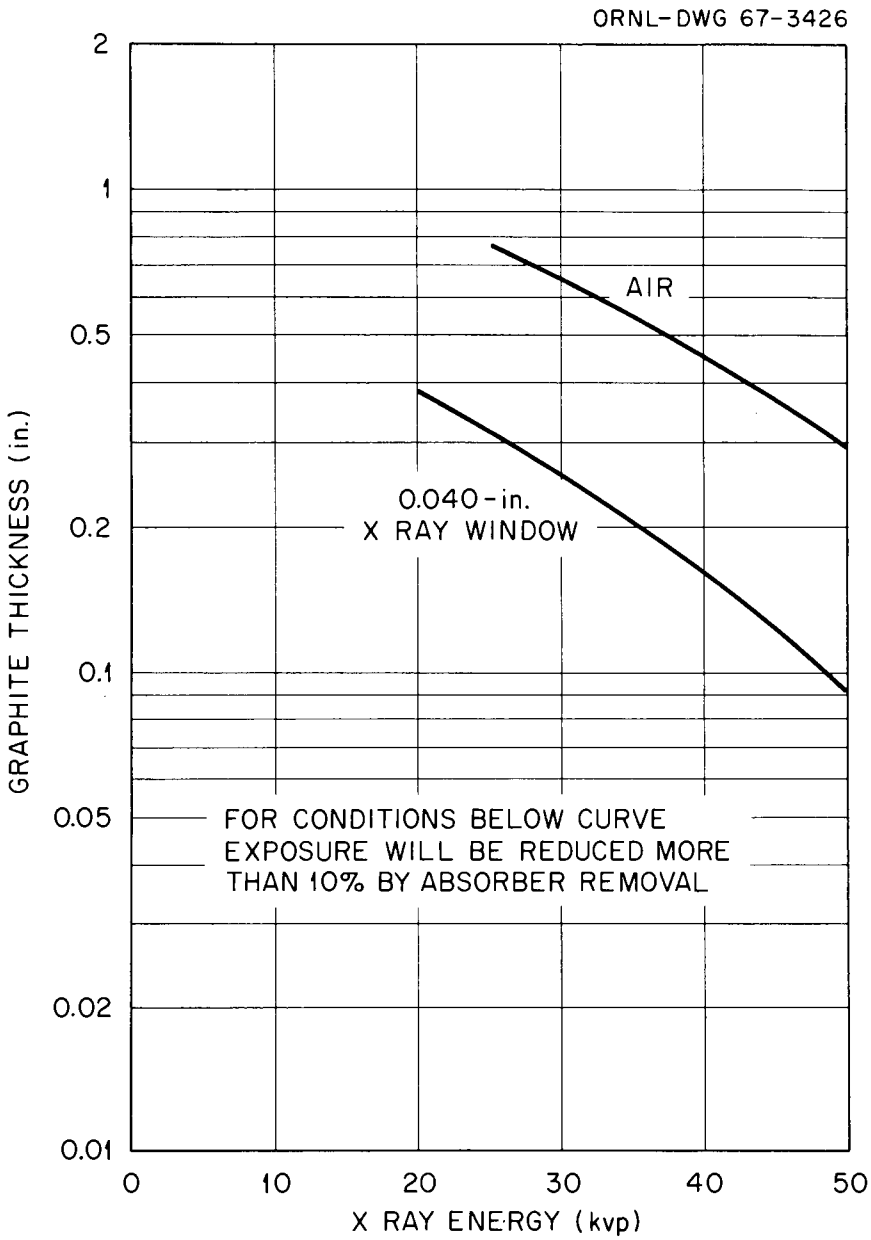

Fig. 3.2. Conditions under Which Absorber Removal Will Effect 10% Change in Exposure Requirement for Radiography of Graphite.

[redacted]

[redacted]

4. SINTERED ALUMINUM PRODUCTS DEVELOPMENT

W. R. Martin

Sintered aluminum products are powder-metallurgy-produced alloys that consist of aluminum oxide dispersed within an aluminum matrix. These alloys have a high strength-to-weight ratio, and this beneficial effect is stable up to temperatures approaching the melting point of aluminum.

Although this alloy is attractive for applications in several reactor systems, commercial SAP products lack the reproducibility of properties needed for many nuclear components. Our program was initiated to investigate the problems and parameters related to primary billet fabrication of SAP for HWOCR fuel rods and pressure tubes. General process steps involve feed-powder characterization, dispersion preparation, and consolidation.

Dispersion Preparation

G. L. Copeland

The parameters for producing nominal 9% oxide flake in the 36-in.-diam pilot plant mill have been determined. The mill is ribbed and filled to 33% of its volume, with 1/2-in.-diam hardened steel balls. The 27-lb charge is −100 mesh air-atomized aluminum powder amounting to 4% of the weight of the balls. Mineral spirits equal to twice the weight of the aluminum powder and stearic acid amounting to 3% of the weight of the aluminum powder serve as the milling vehicle and lubricant. The mill rotates at the critical speed of 44 rpm and is water cooled to maintain a temperature of approximately 40°C. Air is circulated through the mill to assure a normal air atmosphere during milling.

As shown in Fig. 4.1, the oxide content is a linear function of milling time up to 12% oxide. A series of ten batches run under essentially identical conditions for milling times of 20 hr indicates that the oxide content is reproducible within the precision of the measurement techniques. The mean and expected deviations for 20-hr-milling

[redacted]

[redacted]

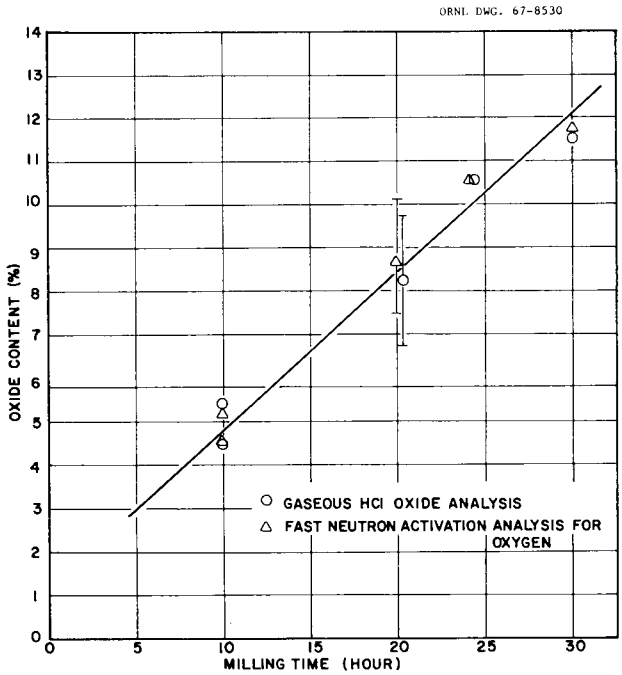

Fig. 4.1. Oxide Content as a Function of Milling Time for the 36-in.-Diam Mill with Reference Process.

time are 8.70 ± 2.80% oxide by the fast neutron activation analysis and 8.22 ± 1.54% oxide by the gaseous HCl dissolution technique.

We believe these parameters apply to the longer 36- and 48-in.-diam mills used in the commercial production of aluminum flake, since the important dimension for milling action is the diameter. Figure 4.2 shows that the oxide content increases linearly with mill diameter from 10 to 48 in., with constant milling conditions and times. The milling conditions were those listed above, except for a 6% Al powder loading. The milling in the 48-in.-diam mill was done in a 48- by 6-in.-long laboratory mill by Reynolds Metals Company to ORNL specifications.

The coarse particle analysis for aluminum pigment in ASTM-D480 was investigated as a possible process control check for ball milling. Several runs from the 36- and 48-in.-diam pilot plant mills were tested for +325 mesh particles. Figure 4.3 shows the relation of +325 mesh fraction and oxide content. The ten 20-hr runs have (3.25 ± 2.14%) +325 mesh fraction. The expected deviations for these runs are indicated by the box in Fig. 4.3. Although there is some scatter in the data, the test is simple and quick to perform and may prove useful as an early indication of process control.

[redacted]

[redacted]

ORNL DWG. 67-8531

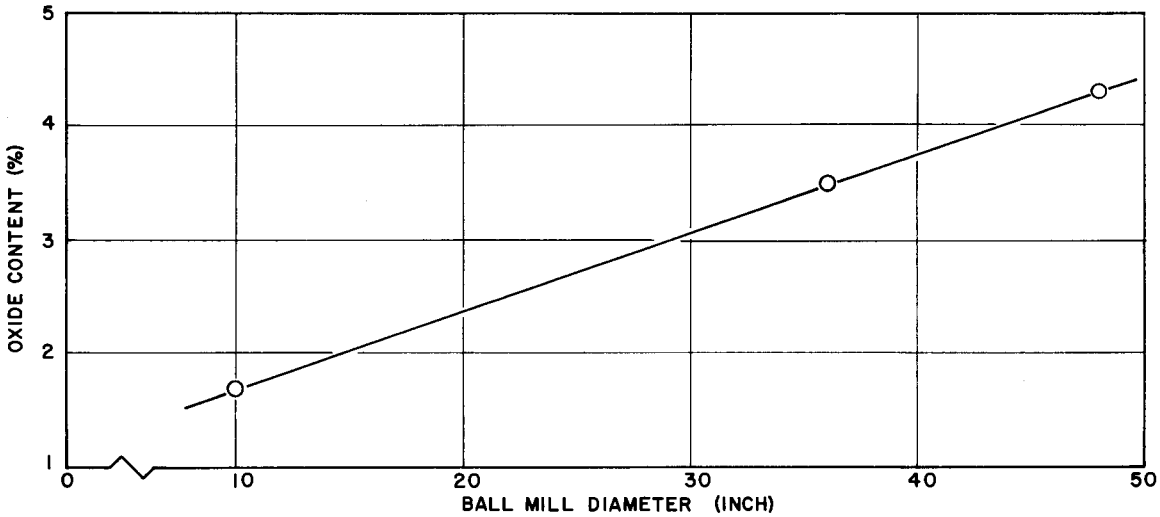

Fig. 4.2. Effect of Ball-Mill Diameter on Oxide Content of Aluminum Flake Milled under Constant Conditions and Times.

ORNL DWG. 67-8532

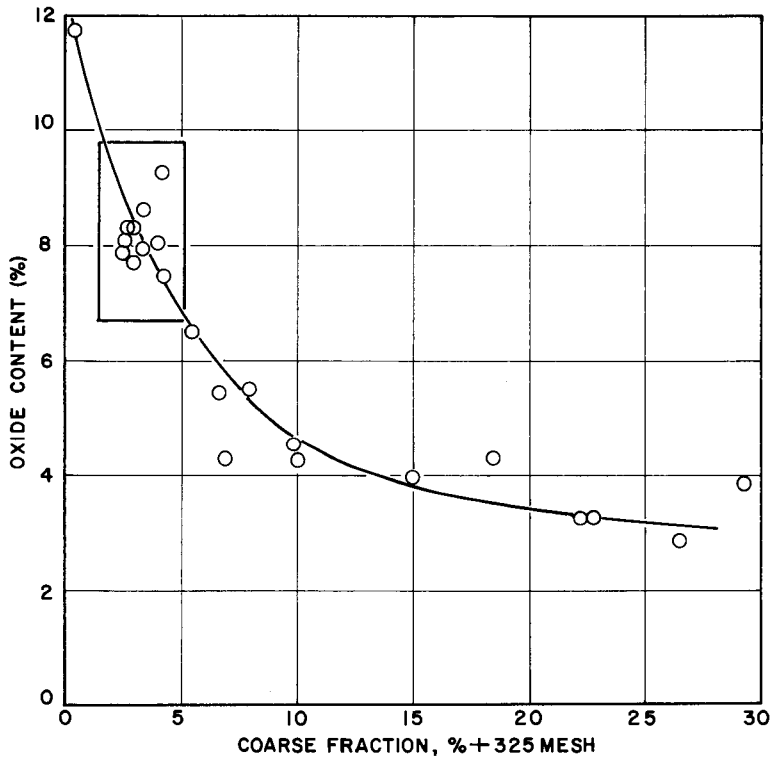

Fig. 4.3. Correlation of Coarse Fraction of Flake with Oxide Content.

[redacted]

The use of steel balls and mills results in inclusion of approximately 0.3% Fe in the flake powder. This iron has successfully been removed on a small scale. However, the small gravity-fed magnetic filter proved inefficient for processing the ball-mill slurry, due to clogging after only a few minutes in operation. A pressure filter may handle the slurry more efficiently.

Powder Consolidation

G. L. Copeland M. M. Martin

On the basis of superior mechanical properties with minimum variability, we selected vacuum hot pressing for more detailed evaluation and scale-up for pilot production of 10% Al_2O_3-SAP billets. Our aim is to achieve a product that is equivalent to commercially available SAP 895, which contains approximately 10% oxide. Parameters that are currently under investigation involve the temperature for vacuum annealing the powder; the density of the consolidated billets; permissible levels of iron, carbon, and hydrogen impurities; and the necessity of vacuum annealing the billets after consolidation.

The primary purpose of vacuum annealing SAP flake is to convert the aluminum oxide hydrate to a stable form of Al_2O_3 and to remove volatile contaminants. To select optimum heat treatment parameters of time and temperature, commercial Al–6% Al_2O_3 and ORNL's ball-milled powder containing 10% Al_2O_3 were subjected to vacuum thermal gravimetric analysis. The study included exposure of degassed materials to 1 atm of moist air.

Figure 4.4 shows the cumulative weight loss for a 5-g sample of ORNL's product at all stages of the experiment. Before the initial heating, the analytical system was evacuated to slightly less than 10^{-3} torr. The reduced pressure permitted approximately 60% of the maximum weight loss of 56 mg/g of sample to occur during the pumpdown at room temperature.

Figure 4.5 depicts the differential weight loss curve that was determined for ORNL's product upon heating to 600°C at a rate of 100°C/hr; the commercial flake behaved similarly. The peak shown in Fig. 4.5 at

[redacted]

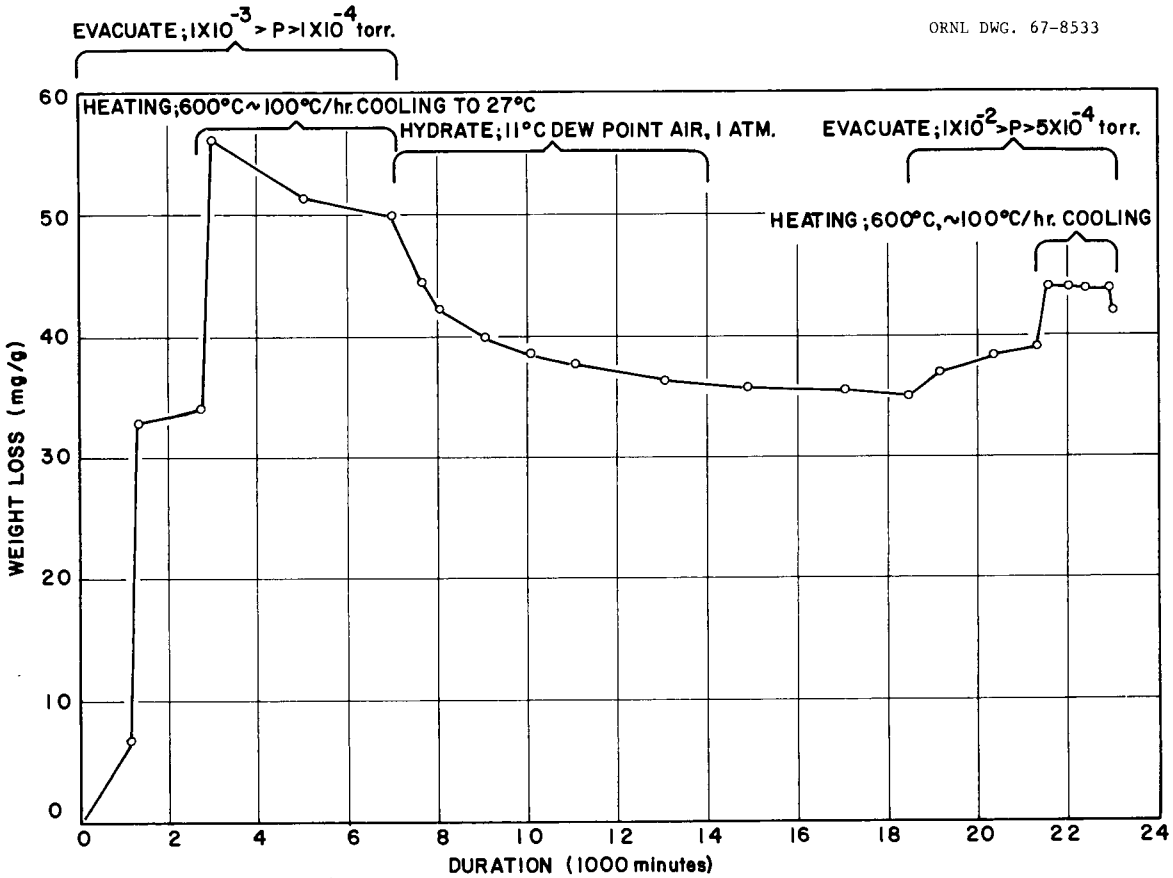

Fig. 4.4. Thermal Gravimetric Analysis of Experimental SAP Flake Containing 10 wt % Al_2O_3.

about 165°C results primarily from the release of loosely attached water and carbonaceous materials. Approximately 50% of the carbon-bearing products from ball milling are released at this temperature. The aluminum hydrate decomposes around 365°C, although some volatile hydrocarbons are still being evolved during this period of rising temperature. The temperature must be raised to 600°C to reduce the carbon level to less than 0.5%.

The oxide on identical SAP powder that had also been annealed in vacuum at 600°C was concentrated in aqueous HCl for x-ray analysis. The residue contained only chi and eta phases, which are believed to be the stable forms of Al_2O_3 on the ball-milled flake.

[redacted]

[redacted]

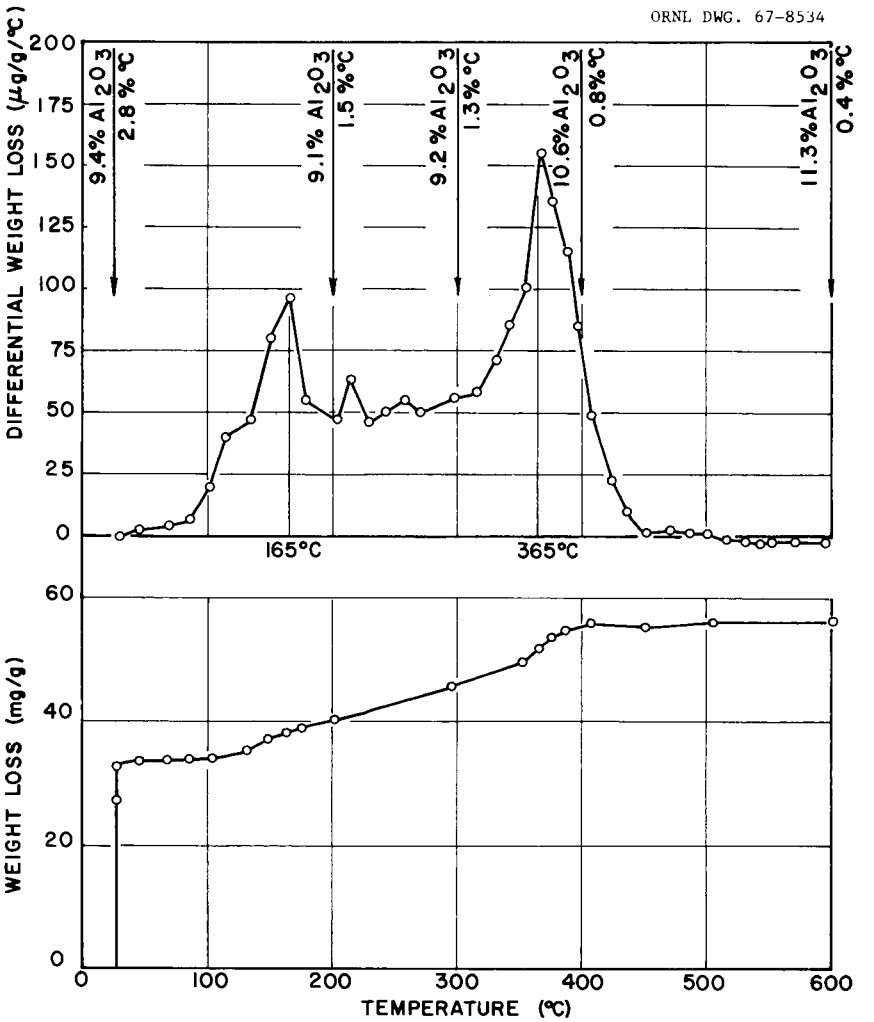

Fig. 4.5. Effect of Temperature on Degassing Experimental SAP Flake at Approximately 5×10^{-4} Torr.

When exposed to 11°C dew-point air, the degassed material gains weight at the rate of 18 μg/g-min as depicted in Fig. 4.6. With further exposure, the rate of adsorption decreases exponentially to about 0.5 μg/g-min at the end of 120 hr. As shown in Fig. 4.4, the material loses approximately 50% of this weight gain upon reheating to 600°C. Heating to above the melting point did not produce an additional weight change.

In preparing SAP billets, two techniques for converting the oxide are being evaluated on the basis of level and reproducibility of ultimate tensile strength of extruded products. The present "reference" process entails heat treating the powder before vacuum hot pressing. The

[redacted]

[redacted]

ORNL DWG. 67-8535

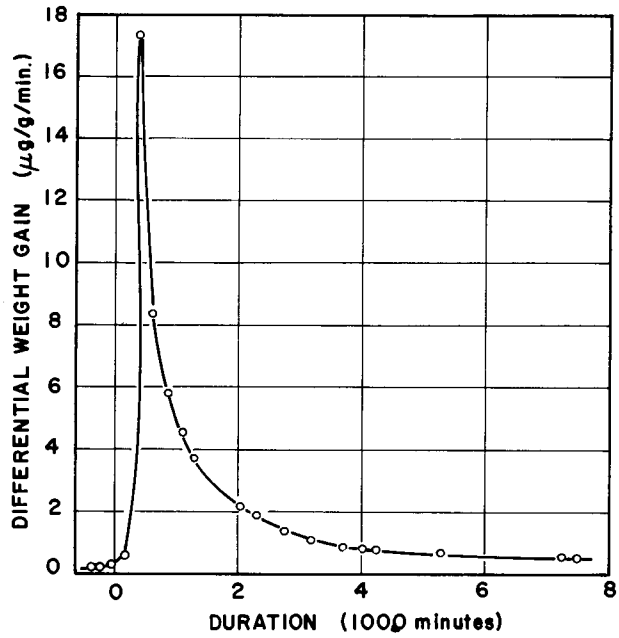

Fig. 4.6. Rate of Water Adsorption on Degassed Experimental SAP Flake when Exposed to 11°C Dew-Point Air.

alternative procedure is to consolidate "as-received powder" and then vacuum anneal the billets immediately prior to extrusion. As reported previously,[1] we prepared billets of various initial densities by both techniques for evaluation of mechanical properties. The results are presented in graphic form in Fig. 4.7. The solid lines and I bars depict the average ultimate tensile strengths at 450°C and 0.002 min^{-1} strain rate and statistical variations found in the extrusions. Line A is for 2-in.-diam billets extruded through a shear die at 30:1 reduction in area; the B and C lines represent extrusions of 4-in.-diam billets that were first reduced 5.2:1 with shear dies and then reextruded through conical dies for a total reduction in area of 156:1. Line B shows the data for vacuum-annealed billets that contained 6% Al_2O_3-SAP powder. Because of the quantity of material required, the billets for the reference process were made from a different batch of flake containing 5% Al_2O_3.

[1]M. M. Martin and D. H. Turner, Fuels and Materials Development Program Quart. Progr. Rept. Mar. 31, 1967, ORNL-TM-1825, pp. 26–32.

[redacted]

[redacted]

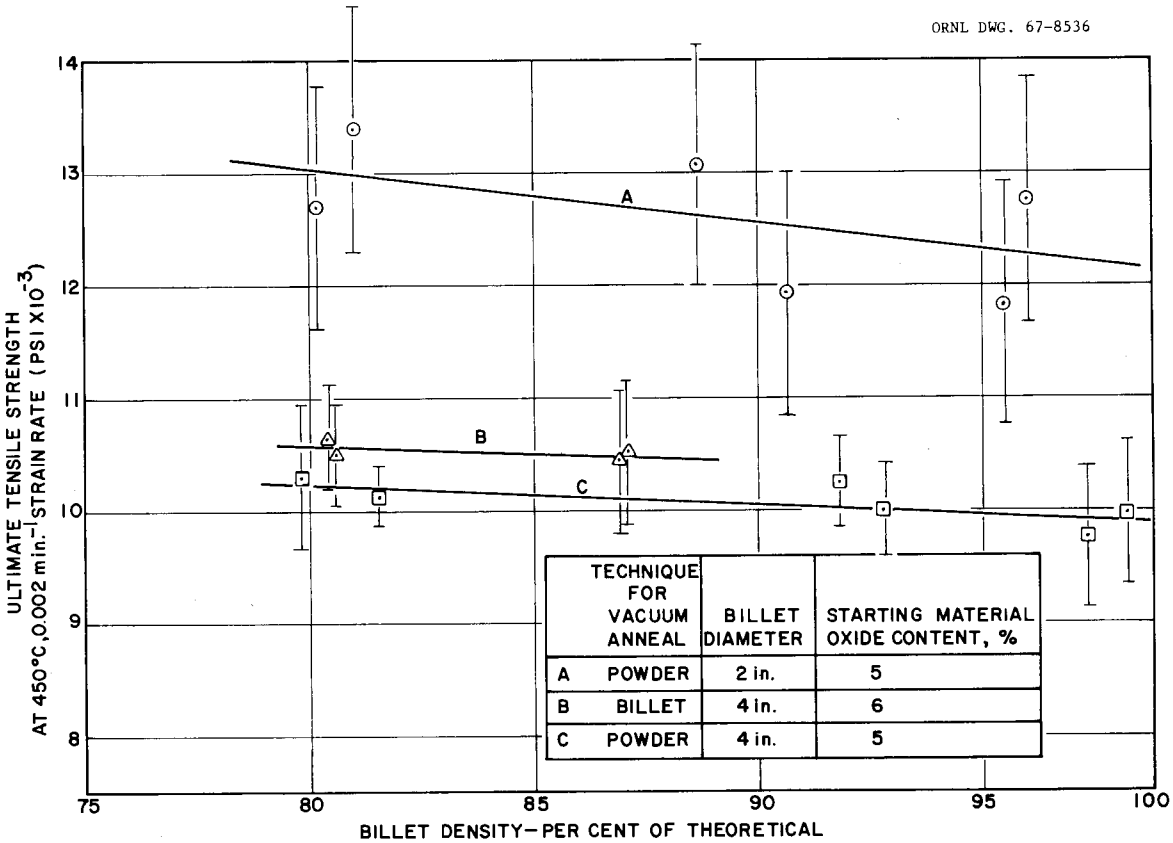

Fig. 4.7. Strength Evaluation of SAP Rods Extruded from 2- and 4-in.-Diam Billets.

Analysis of the tensile data and subsequent oxide content of each tensile specimen from the 2-in.-diam series showed no correlation of strength with initial billet density, distance from the nose of the extrusions, and Al_2O_3 content. As illustrated in Fig. 4.7, these rods exhibited expected variations of ±1200 psi. We found that the oxide concentration of the specimens depended strongly upon the lengthwise location in the extrusions. Their dependence, however, fails to account for the large strength variations.

In view of the higher oxide content for line B than for line C in Fig. 4.7, the two vacuum annealing techniques do not appear to differ significantly in their effect on the strength of the extruded rods.

The tensile results of this 4-in.-diam series also showed no correlation of strength with initial billet density and distance from the nose of the extrusions. In this case, the oxide concentration of the tensile specimens, however, was independent of their lengthwise location along

[redacted]

the length of the rods. Within a particular rod, the extrusions further exhibited excellent uniformity of strength; the total expected variations are less than 5% of the average tensile values. It now appears that the variability in strength of the 2-in.-diam series extrusions is associated with the oxidation of the porous 2-in.-diam compacts. All future evaluation of materials will use at least 4-in.-diam billets to minimize the exposed surface area-to-volume ratio.

Comparison of lines A and C in Fig. 4.7 shows that secondary working reduces significantly the ultimate tensile strength. An expected decrease in tensile strength at high reduction ratios has been reported previously for SAP materials.[2] We plan to verify this observation on billets consolidated from ORNL's produced flake containing 10% Al_2O_3. In this series, the vacuum heat treatment technique will also be reevaluated for the high oxide material.

Fracture Studies of SAP Alloys (D. G. Harman, T. A. Nolan[3])

The initiation of fracture of SAP alloys continues to be of interest. Previous reports have included fractographic analyses of the very fine-scale topographic features of fracture surfaces.

Surface markings indicative of macrodefects have been observed on ruptured rod and tube specimens of commercial SAP products. These markings appear as an "x" oriented along the maximum shear directions and varying in size from a mil to as large as a tenth of an inch.

Tensile specimens of XAP-001 were polished longitudinally and subsequently tensile tested. One specimen that had been strained at room temperature until necking was obvious was studied for surface markings. Figure 4.8 shows several light micrographs of the specimen surface marking at magnifications of 2 to 450× and a reflection electron micrograph at 1000×. Figure 4.9 shows the shear "x" at higher magnifications. The reflection micrographs show that the material apparently

[2]P. B. Ferry, Effects of Fabrication on the Mechanical Properties of SAP, AI-CE-TDR-1032 (Jan. 11, 1966).

[3]Physics Group, Technology Division, ORGDP.

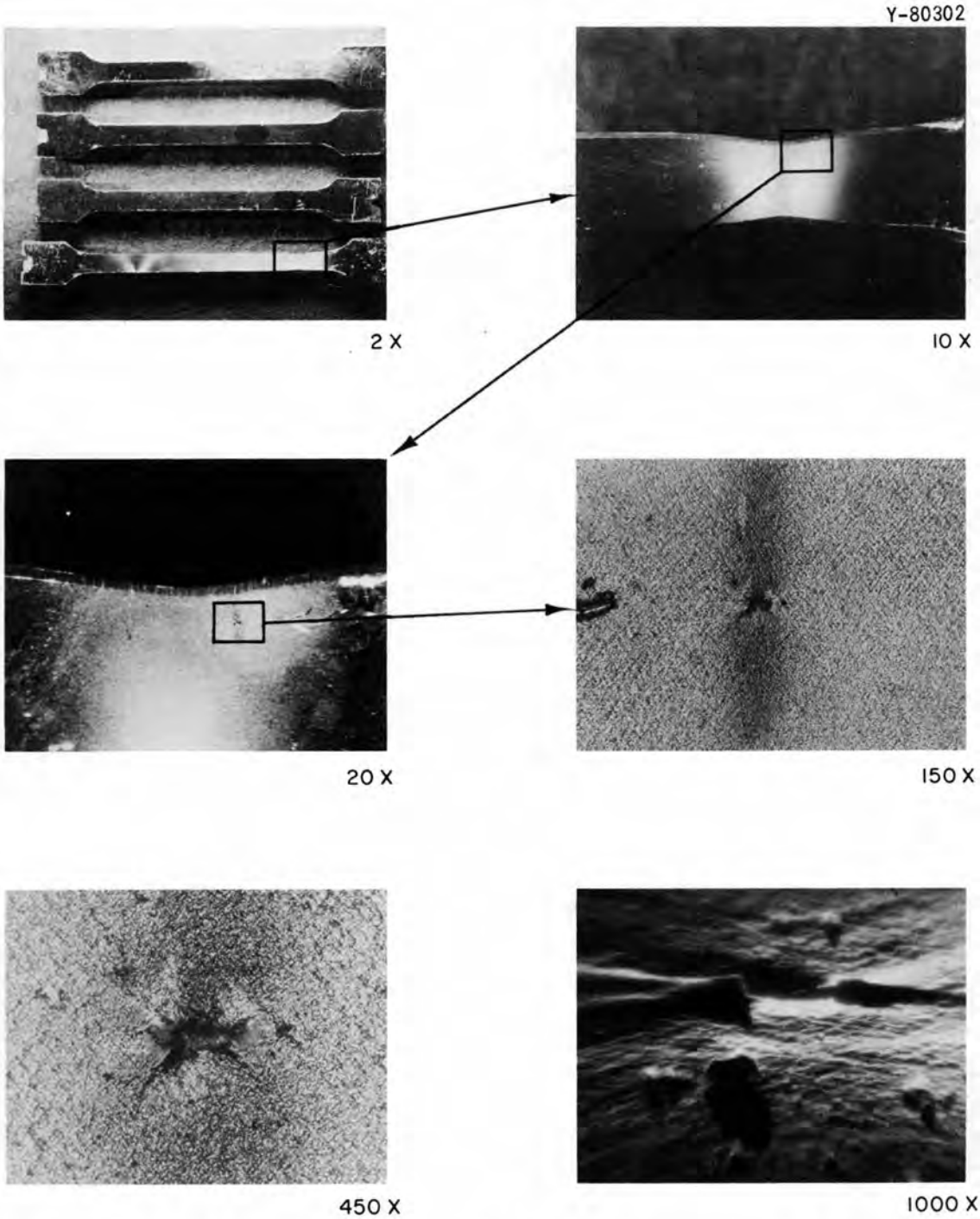

Fig. 4.8. Light and Reflection Electron Micrographs of a Shear "x" on a Tensile Specimen of XAP-001 SAP Alloy.

[redacted]

Y-80307

2700X

SPECIMEN AXIS

4200X

Fig. 4.9. Reflection Electron Micrographs of a Shear "x" on a Tensile Specimen of XAP-001 SAP Alloy.

[redacted]

extruded from the surface along the projection of the conical shear zones emanating from the cracked region. The axes of the shear cones are coincident with those of the specimen axis and their surfaces are parallel with the fine-scale shear markings as shown in Fig. 4.9.

Similar surface markings observed on tensile specimens of a titanium bi-alloy (alloy-alloy composite)[4] were shown to originate as cracks in the brittle high-strength component that were arrested in the ductile alloy matrix. It is thought that the markings on SAP specimens indicate cracks starting at internal defects such as voids, inclusions, or oxide agglomerates. The size of the "x" varies as the proximity of the "defect" to the specimen surface. To date efforts to examine the internal surface of the cracked portion have been unsuccessful.

Nondestructive Testing (H. L. Whaley)

We have been concerned with the development of systems and techniques for determination of flake thickness and oxide content of the aluminum powders. An air-settling device is being developed for the flake-thickness measurements, and eddy-current conductivity measurements on fused compacts of SAP are being employed on the oxide content problem.

Samples of MD-3100 as-received powder have been successfully dispersed and collected at the following pressures: −20 in. of mercury (0.30 atm); −25 in. (0.17 atm); −26.5 in. (0.12 atm); −27 in. (0.10 atm); and −28 in. (0.07 atm). Measurement of particle thickness (μ) collected as a function of settling distance (inch) generated linear curves as expected. The slope of $\frac{0.03\ \mu}{\text{in.}}$ for 0.07 atm was the greatest slope, and the intercept on the thickness axis was near 1.0 μ for each curve.

Current plans are to operate at even lower pressures to increase the slope and to work with some ball-milled flake produced in an experimental mill at ORNL.

Work is progressing on the fused wafer technique for rapid determination of oxide content in SAP powder using eddy currents. In the last

[4]Stanley Abkowitz, "Micro-Quenched Age-Formed Ti Alloys and Ti Bi-Alloy Composites," J. Metals 18(4), 458–464 (April 1966).

report a 3% apparent oxide variation over a wafer surface and a 4% apparent oxide difference over the set of six wafers from the same powder batch were reported. These variations were cut in half by cold pressing the wafers in addition to the fusing. Another fused set made the same way to check reproducibility is near completion.

Photomicrographs of surfaces of the six fused wafers normal to their faces have been made. At 50× these show extensive cracking parallel to the surfaces which undoubtedly contributes to the variations in conductivity from point to point on the wafer surfaces.

SAP-UC Compatibility Experiments (J. T. Venard)

A series of experiments to investigate the compatibility reaction between SAP and UC has been performed. These experiments tested 10 wt % oxide SAP against hypostoichiometric, stoichiometric, and hyperstoichiometric uranium monocarbide over the temperature range 450 to 625°C.

The spring-loaded compatibility capsules used in these experiments did not produce as much reaction product as had been observed by other experimenters. The amount of reaction product observed and the capsule loading conditions are, however, probably representative of a fuel rod in an unpressurized reactor.

The activation energy for the growth of the reaction product in 4.8 wt % C samples was found to be 83.6 kcal/mole. The corresponding value for 5.1 wt % C samples is 92.4 kcal/mole. Results for 4.6 wt % C samples were very erratic, presumably because of the presence of free uranium, and have not given any useful information.

A report covering the details of these experiments and their analysis has been drafted and is expected to be issued shortly.

[redacted]

5. ZIRCONIUM METALLURGY

P. L. Rittenhouse

Several zirconium-base alloys are in use or of potential use as fuel cladding and pressure tubing in nuclear reactors. It is of considerable economic importance that the strength properties and corrosion resistance of these materials be improved. To achieve the first objective — increased strength — we are studying the very substantial strength advantage that can be realized by control of crystallographic texture. A very promising method of improving corrosion properties by surface treatment has developed from our investigation of the mechanisms of the oxidation process and is under continuing study.

Anisotropy in Zircaloy

P. L. Rittenhouse

Tubing Tests

A contract has been let for the construction of the external-pressure modification of the tubing tester. This, when completed, will give us the capability of determining a complete yield locus and testing under hydrostatic pressure.

A second solid-state model servo-controller has been received and installed. Hopefully, this will solve the problems we have encountered with instability of hydraulic flow. The grip system for testing in biaxial modes has been redesigned and is being machined.

Strain Behavior in Uniaxially Tested Zircaloy Tubing

The strains that occur normal to the test axis of both round cross-section and sheet-type tensile specimens of Zircaloy can be used to characterize the anisotropy of the material.[1] The same should be true for tubing specimens. To satisfy ourselves that this is indeed true, we

[1]P. L. Rittenhouse, "Determination of Anisotropy of Yielding and Flow in Zircaloy-2 from a Single Test," to be published in Journal of Nuclear Materials.

[redacted]

[redacted]

have measured diameter and wall-thickness strains on tubing specimens tested in tension. The data obtained were plotted versus the axial strain to determine the k values (slopes of the plots of diameter and thickness strains versus axial strain).[2] Data for two materials are shown in Fig. 5.1.

Material Y-2 has a texture such that most of the basal poles are parallel or near parallel to the tube radius. Both the axial elongation and diameter reduction can be accomplished by prism slip, $\{10\bar{1}0\}\langle 11\bar{2}0\rangle$, but the operation of this deformation mechanism gives no component of strain parallel to the radius. Any such strain must occur by $\{11\bar{2}2\}$ twinning in grains aligned as above, or by prism slip in the much fewer number of grains with basal poles near the tangential direction. The tubing will resist change in wall thickness and $\bar{\epsilon}_{Z\theta}$ will be greater than $\bar{\epsilon}_{ZR}$. Therefore, $k_{Z\theta} > k_{ZR}$.

If, however, most of the basal poles are parallel to the tangential direction (material W-7), the opposite is true. Elongation and wall-thickness reduction will occur readily by prism slip, but the diameter will be resistant to change. In this case $\bar{\epsilon}_{Z\theta} < \bar{\epsilon}_{ZR}$ and $k_{Z\theta} < k_{ZR}$.

It is obvious from the above that it should be possible to correlate the relative diameter and wall-thickness strains with some measure of texture. The concentration of basal poles in any direction, expressed as a multiple of that in a random sample, provides a convenient measure of texture. This is usually referred to as the basal texture coefficient, $TC_{(0001)}$. The ratio of the texture coefficient in the radial direction to that in the tangential direction is shown in Table 5.1 to correlate well with the ratio $k_{Z\theta}/k_{ZR}$.

When there are an equal number of basal poles in the radial and tangential directions (an equal distribution in the plane perpendicular to the tube axis), the k's will be equal to −0.50. If the texture coefficient is greater at either the radial or tangential direction, a $k < -0.50$ will be observed for that direction. The k's, then, are a

---

[2]P. L. Rittenhouse and M. L. Picklesimer, "Research on the Mechanical Anisotropy of Zircaloy-2," Electrochem. Technol. 4(7–8), 322–329 (July–Aug. 1966).

[redacted]

[redacted]

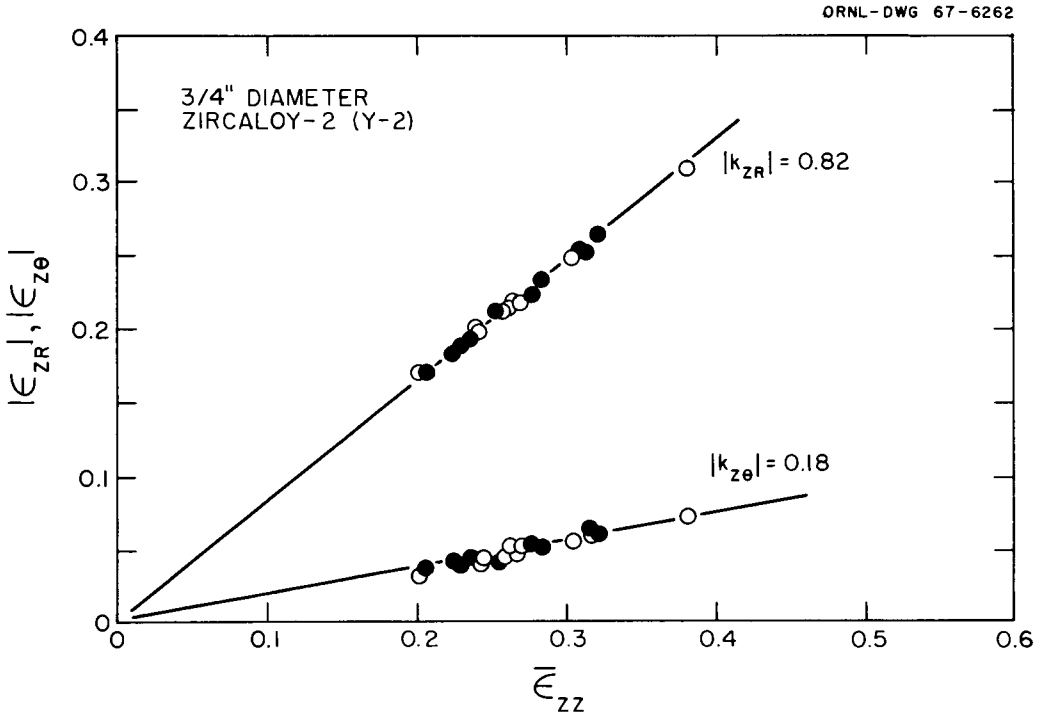

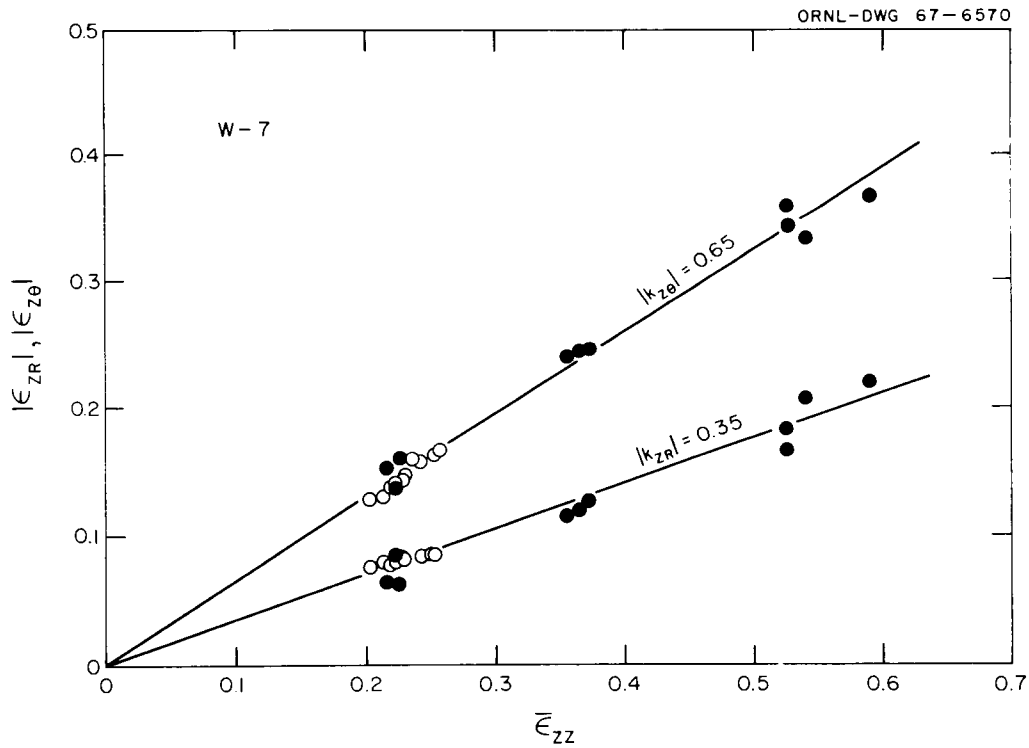

Fig. 5.1. Diameter and Wall-Thickness Strains Versus Axial Strain for Zircaloy Tubing. Material Y-2 and material W-7. The diameter strain is $\bar{\epsilon}_{Z\theta}$, the wall strain $\bar{\epsilon}_{ZR}$.

[redacted]

Table 5.1. Correlation of Texture Coefficients and k's

Tubing Code	$TC_{(0001)_R}/TC_{(0001)_\theta}$	$k_{Z\theta}/k_{ZR}$
S-1	1.6	1.4
S-2	1.6	1.2
T-1	1.8	1.6
U-2	1.0	0.9
W-7	1.6	1.8
Y-1	3.2	2.7
Y-2	0.31	0.22

measure of the relative resistance to flow and reflect the texture present in the material through its anisotropy of properties.

The method described here is not peculiar to the material and could be used to study anisotropy and texture in tubing of any material. To correlate the k's with any particular component of the texture, as we have the basal pole, the crystallographic deformation behavior of the material must be known.

Texture Development in Single-Crystal Zirconium

D. O. Hobson

Our goal in this work is to control the textures of fabricated zirconium and zirconium alloys and, thereby, utilize their directionality of mechanical properties. To do this we must know what effects various fabrication operations have on the textures of the material. The textures produced in commercially fabricated sheet and tubing are well known and, thanks to the increasing cooperation of commercial vendors, more detailed fabrication history is becoming available. Trying to design fabrication procedures to produce "tailored" textures from a knowledge of what previous schedules have produced, however, is a highly empirical approach. Instead, we are starting from basic considerations of the effects that various stress and strain systems have on the available deformation systems of

the material being fabricated. It has been demonstrated by Reed-Hill[3] that polycrystalline zirconium deforms to a large extent as if each grain were acting as a single crystal under the applied stress. It follows, therefore, that if one "fabricates" an oriented single crystal, it will deform in much the same way that a grain with identical orientation will deform in a polycrystalline matrix. We have deformed single crystals by straight rolling, wire drawing, and tube drawing over a mandrel. The texture changes were followed by x-ray and polarized-light microscope techniques.

The common, idealized rolling texture of zirconium is one in which the basal poles lie 35 to 40° from the normal of the rolling plane toward the transverse directions. The usual tubing textures, again idealized, are: (1) the majority of the basal poles in the tangential direction of the tubing when the tubing is drawn by sinking; and (2) an approximately 50-50 distribution of poles between the tangential and the radial directions for tubing drawn over a mandrel (ironing). Our initial interest has been to see if the textures produced by fabricating single crystals approach the idealized fabrication textures found in polycrystalline material.

Rolling Textures

Single-crystal specimens of four starting orientations or textures have been rolled to various reductions. The initial orientations of the specimens can be described by standard texture nomenclature where the first set of indices refers to the plane parallel to the rolling plane and the second to the direction parallel to the rolling direction. These orientations are $(11\bar{2}0)[0001]$, $(0001)[10\bar{1}0]$, $(0001)[11\bar{2}0]$, and $(11\bar{2}0)[10\bar{1}0]$. For purposes of illustration the results of a common reduction of 20% in thickness will be discussed.

When the $(11\bar{2}0)[0001]$ specimen was rolled we found that the [0001] rotated to positions 36–40° on each side of the normal to the rolling

[3] R. E. Reed-Hill, "Role of Deformation Twinning in the Plastic Deformation of a Polycrystalline Anisotropic Metal," pp. 295–330 in Deformation Twinning, Gordon and Breach, New York, 1964.

plane toward the transverse directions (i.e., into the ideal rolling texture). We know that $\{10\bar{1}2\}$ twinning rotates the basal pole 86° to positions 30° on each side of the normal. This is within 6 to 10° of the required position, a distance easily covered by rotation due to slip or kinking.

Rolling the $(0001)[10\bar{1}0]$ and $(0001)[11\bar{2}0]$ specimens produced textures that were explainable by a combination of first- and second-order twinning. Basal pole concentrations were found in positions near 30 and 70° from the rolling plane normal toward the original $\langle 11\bar{2}0\rangle$ directions. The basal pole concentration at 70° was the result of $\{11\bar{2}2\}$ twinning. This would be expected since the $\{11\bar{2}2\}$ twinning system operates by compression along the basal pole. Part of the 70° texture was shifted again, by $\{10\bar{1}2\}$ and/or $\{11\bar{2}1\}$ secondary twinning, to the 30° position. Both of these systems operate by tension along the basal pole. There was considerable spread around the 30° position toward the normal and the original $\langle 11\bar{2}0\rangle$ directions. This could be due to rotation by slip or by kinking, but complete analysis must wait until the specimens can be examined on a texture diffractometer.

The $(11\bar{2}0)[10\bar{1}0]$ specimen was rolled to determine if the "easy glide" orientation would allow the specimen to deform without a change in texture; that is, without twinning. It did. A back-reflection Laue pattern taken off the (0001) surface is shown in Fig. 5.2. The small amount of asterism is due to specimen bending resulting from a side-to-side difference in thickness. Figure 5.3 shows some previously existing small twins caused by hand polishing. Before the specimen was rolled, the traces were at included angles of 60° from one another. Following rolling the trace angle was reduced to 37°. Slip line traces were also seen with included angles of 53 rather than 60°. The slip traces are seen to intersect the twins.

The foregoing data show us that the stresses and resulting strains of rolling are equivalent to simple compression normal to the rolling plane and tension in the rolling direction.

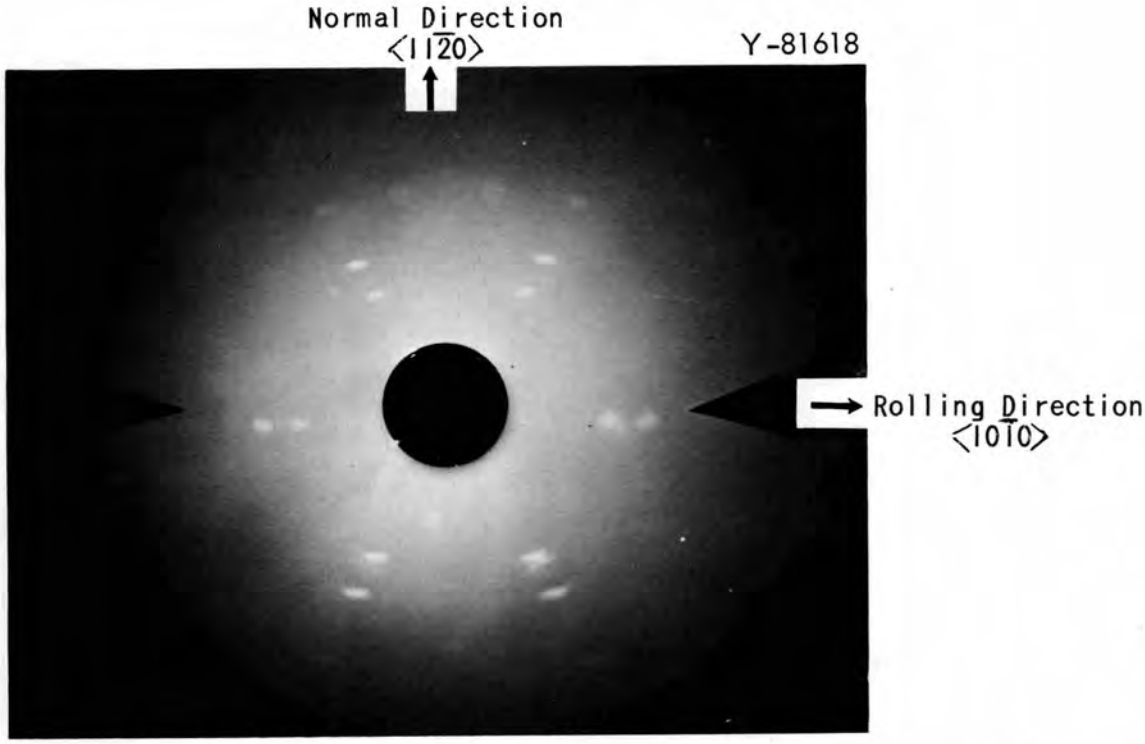

Fig. 5.2. Back-Reflection Laue Pattern Taken on (0001) Surface of the (11$\bar{2}$0)[10$\bar{1}$0] Rolling Specimen.

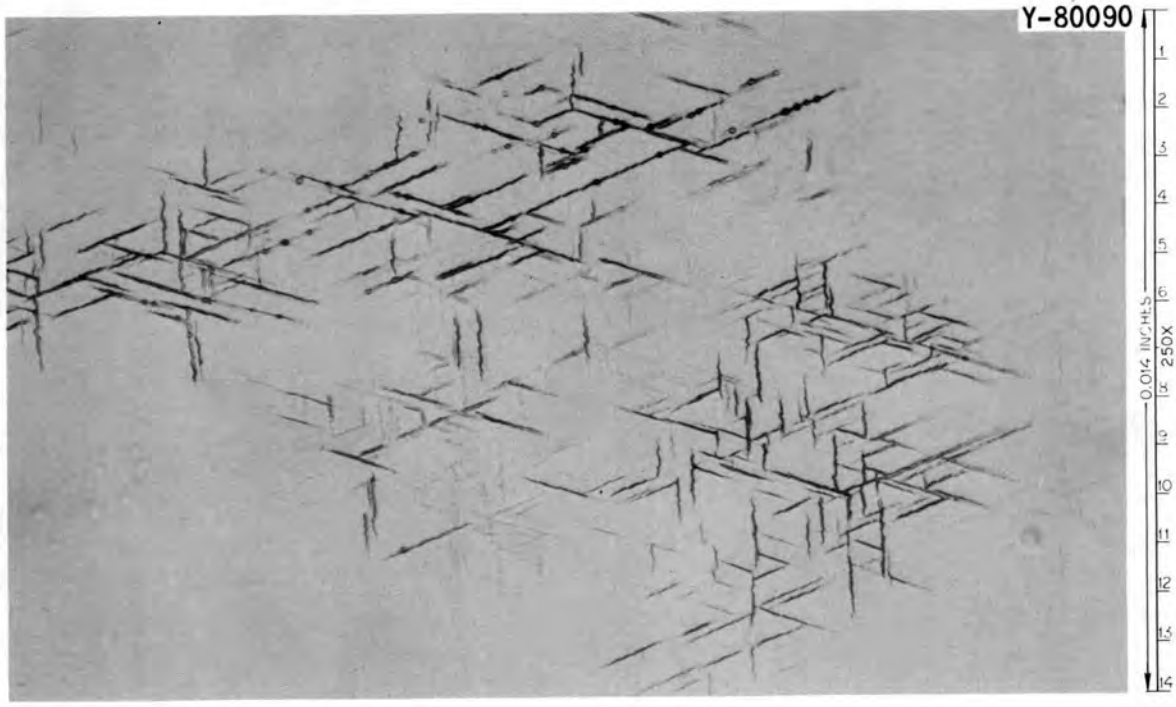

Fig. 5.3. Small Twins on the (0001) Surface of the (11$\bar{2}$0)[10$\bar{1}$0] Rolling Specimen. The twins were produced by hand polishing of the surface before rolling. The included angle between the twins decreased from 60 to 37° during rolling.

[redacted]

Drawing Studies

We have tube drawn (over a steel mandrel) one single crystal in the <0001> direction, and we rod drew another in the $\langle 11\bar{2}0\rangle$ direction. Both were reduced 5%. Figure 5.4 shows the tube drawn specimen surface perpendicular to the drawing direction. This was originally the (0001) surface, but only a very small fraction of the original surface orientation remained after drawing. As expected, the specimen twinned by the $\{10\bar{1}2\}$ and $\{11\bar{2}1\}$ systems, both of which require tension on the

Fig. 5.4. Surface Perpendicular to the Drawing Direction of a Zirconium Single Crystal. 15×.

[redacted]

basal pole. The largest volume fraction of twinned material was due to $\{10\bar{1}2\}$ twinning. The $\{10\bar{1}2\}$ twins are the large irregular twins which occur every 60° around the specimen. The $\{11\bar{2}1\}$ twins account for only a very small fraction of the specimen volume and are seen as thin lines occurring every 60° around the specimen, 30° from the $\{10\bar{1}2\}$ twin traces.

The other single crystal was oriented to produce compression on the basal pole and, indeed, the $\{11\bar{2}2\}$ compression twin predominated. Also present, however, were $\{10\bar{1}2\}$ tension twins. This indicates that uniform compression on a plane perpendicular to the $\langle 11\bar{2}0\rangle$ can produce a complex stress situation that is equivalent to tension on the basal pole.

These studies have shown us the following very important fact: No matter how complex the deformation method seems to be, whether by rolling or by drawing, the specimens deform by simple, easily identifiable twinning sequences and by slip to achieve the required final shape. The twinning systems operate to provide the proper orientations for further deformation by slip and thereby produce the texture of the material. Knowing the above and assuming that the grains in polycrystalline zirconium tend to act independently of one another, we are ready to extend our analysis to large-grained polycrystalline zirconium. If, as we suspect, the deformation systems in each grain respond predominately to the strain requirements produced by the particular fabrication operation being used and not to the influences of surrounding grains, we should be able to predict the texture changes that will occur in specimens of smaller and smaller grain sizes. Rolling specimens are presently being cut that will have grains up to 1/4 in. in diameter extending through the thickness of the specimen. We will determine the orientations of these grains, calculate how they should deform when rolled, and then study their actual orientations after rolling. The difference between the actual texture and the predicted texture will indicate the influence of surrounding grains. If we can predict the textures that will result from these fabrication operations, we will know that there is an excellent chance of controlling and "tailoring" textures in fabricated reactor parts.

[redacted]

Optical Properties of Zirconium Alloys

L. T. Larson[4]

The optical properties of zirconium and its alloys that are used in determining crystallographic orientation have been described and discussed in earlier reports.[5–7] In particular, the apparent angle of rotation (A_r) has been determined for zirconium and Zircaloy-2. Since A_r for zirconium differs from that of Zircaloy-2, it is possible that composition variations may be approximated by optical measurements.

An even more fundamental optical property of metals is reflectivity (R). Numerous investigators[8–10] consider reflectivity to be the most important optical property of a reflecting surface. Accurate reflectivity measurements on well-prepared large zirconium grains will provide crystallographic orientation data that, when standardized, should permit relatively rapid texture determinations to be made for fine-grained polycrystalline material. Reflectivity measurements can also provide information from which the indices of refraction (n) and the coefficients of absorption (k) may be calculated. Such information is of value in formulating an understanding of the electron band configuration of metals.

---

[4]Consultant, Department of Geology, the University of Tennessee.

[5]L. T. Larson and M. L. Picklesimer, Fuels and Materials Development Program Quart. Progr. Rept. Sept. 30, 1966, ORNL-TM-1700, pp. 45–48.

[6]L. T. Larson and M. L. Picklesimer, "Determination of the Basal Pole Orientation in Zirconium by Polarized Light Microscopy," Trans. Met. Soc. AIME 236, 1104–1106 (August 1966).

[7]L. T. Larson and M. L. Picklesimer, Fuels and Materials Development Program Quart. Progr. Rept. Dec. 31, 1966, ORNL-TM-1720, pp. 66–69.

[8]H. Piller and K. v. Gehlen, "On Errors of Reflectivity Measurements and on Calculations of Refractive Index n and Absorption Coefficient k," Am. Mineralogist 49, 867–882 (1964).

[9]M. Berek, in: RINNE-Berek, Anleitung zu optischen Untersuchungen mit dem Polarisationmikroskop, 2nd ed., Schweizerbart, Stuttgart, 1953.

[10]E. N. Cameron, "Optical Symmetry from Reflectivity Measurements," Am. Mineralogist 48, 1070–1079 (1963).

[redacted]

The instrumental array necessary for making reflectivity measurements on zirconium has been described.[7] Work to date has been directed principally toward: (1) calibration of the instrumentation and (2) measurement of reflectivity values for zirconium specimens of varied orientations (in air) at a single wavelength of light (668 mμ).

Zirconium is an optically uniaxial substance (hexagonal) and its reflective properties may be described in terms of two indices of refraction (n_1, n_2) and two coefficients of absorption (k_1, k_2). The resulting indicatrix is complex and consists of two surfaces, one giving the indices of refraction for sections of differing orientations through the crystal and the other the coefficients of absorption. The equations relating the reflectivities of the two principal optical directions to the indices of refraction and the coefficients of absorption are:

$$R_1 = \frac{(n_1 - n_o)^2 + k_1^2}{(n_1 + n_o)^2 + k_1^2} ;$$

and

$$R_2 = \frac{(n_2 - n_o)^2 + k_2^2}{(n_2 + n_o)^2 + k_2^2} ,$$

with

k_1 and k_2 = the absorption coefficients corresponding to the principal ray directions in the crystal,

n_1 and n_2 = the refractive indices corresponding to the principal ray directions in the crystal,

n_o = the refractive index of the immersion medium (air = 1).

The <u>bi-reflectance</u> is the difference between R_1 and R_2 for any given set of experimental conditions and is a function of the crystallographic orientation of the specimen. For a complete treatment of reflective light theory see Berek,[9] Cameron,[10] and Piller and K. v. Gehlen.[8]

The experimental conditions for the reflectivity values given in Table 5.2 are as follows: (1) instrumental array as described by Larson and Picklesimer;[7] (2) 20× Vickers microplan flat field, strain-free objective, 1.5× internal microscope magnification, and a 10× ocular for

[redacted]

a total field magnification of 300×; (3) air immersion media; and (4) monochromatic light of 668 mμ wavelength.

All reflectivity values given in Table 5.2 are relative to standards agreed upon by the International Commission on Ore Microscopy. The specific standards used are polished sections of metallic silicon and germanium. The sections were prepared in this laboratory and then sent to E. N. Cameron at the University of Wisconsin for calibration with standards provided by the National Physical Laboratory of Great Britain. Our standards agree with those of Cameron to within ±0.2% of reflectivity. Metallic chromium, with a reflectivity of approximately 50%, has been provisionally agreed upon as a standard by the ICOM. A section of chromium has been prepared and sent for calibration but has not yet been returned. The reflectivities of silicon and germanium in light of 668 mμ wavelength are 34.3 and 46.1%, respectively.

The minimum reflectivity of zirconium under the experimental conditions described above is 59.0 ± 0.3%. The bi-reflectance of zirconium

Table 5.2. Bi-Reflectance as a Function of Crystallographic Orientation of Zirconium[a]

Crystallographic Orientation[b]		Bi-Reflectance (%)
by A_r (deg)	by Laue (deg)	
< 5	1.5	0
38	40	5.15
44	47	5.9
56		7.0
60	65	7.15
71		8.7
83	88	10.4
90	90	10.5

[a]Immersion media air, n = 1.0; light of 668 mμ wavelength.

[b]In degrees from the basal pole. A_r measurements are ±3° and Laue orientations are within 2°.

[redacted]

sections having different crystallographic orientations is given in Table 5.2. The orientations of these sections were determined by measurement of the apparent angle of rotation (A_r) and by Laue x-ray patterns.

Several potential sources of error in reflectivity measurements have been enumerated and evaluated by Piller and K. v. Gehlen.[8] Of those discussed, our most persistent and difficult problem has been obtaining a polished surface that is uniform from one grain orientation to another. It is estimated that, with the polishes presently being obtained, an error of as much as 0.3% may be present. An additional problem encountered is the uncertainty of the reflectivity values of our standards in immersion media other than air. These values are particularly important when attempts are made to measure the reflectivity of zirconium with oil immersion — a necessary step in the calculations of the index of refraction and the coefficient of absorption. It is hoped that standard values will be made available by the National Physical Laboratory in the near future.

Work is proceeding on obtaining a more uniform polish to diminish the error estimated above. In addition, measurements of reflectivity are being made on zirconium grains with orientations other than those given in Table 5.2. The measurements will be made in air and in immersion media with indices of 1.33 and 1.56. It is also intended that reflectivity measurements be made on single crystals of one or two other metals in the near future.

Inhibition of Oxidation by Anodic Films

J. C. Wilson

We have continued to study the inhibiting action of preanodizing,[11] in phosphate-containing solutions, on subsequent thermal oxidation of zirconium in 500°C (15 psia) steam. Following a suggestion of R. E. Pawel,

[11] J. C. Wilson, Fuels and Materials Development Program Quart. Progr. Rept. Mar. 31, 1967, ORNL-TM-1825, p. 49.

who has conducted similar experiments on tantalum, we used concentrated phosphoric acid at the highest possible anodizing voltage to maximize the effects.

Figure 5.5 shows the results for times up to 750 hr. A factor of 4 reduction in weight gain is observed for specimens preanodized at 120 v in concentrated H_3PO_4 (anodized film thickness approximately 2500 A or 4 mg/dm^2). Lesser effects are seen for 60 v films in H_3PO_4 and an organic-base H_3PO_4 solution.[12] Preanodizing of Zircaloy-2 (at only 50 v in 7 M H_3PO_4, because of the difficulty of forming films in the concentrated acid) shows little effect up to 488 hr, the longest test completed.

After 268 hr in 500°C steam, two of the five control (unanodized) specimens were anodized at 150 v in 14 M H_3PO_4. The anodizing current fell almost to zero in a few seconds so the amount of anodized film formed was extremely small. But, as Fig. 5.5 shows (dashed curves), either the anodization or adsorbed H_3PO_4 caused a transient reduction in oxidation rate for at least 200 hr. The spread in data may be due to the different handling of the specimens; the thermally formed oxide had to be ground off one corner to make electrical contact for anodizing.

The curves for zirconium preanodized in the organic-H_3PO_4 solution also show a break at 268 hr; these specimens were adjacent to the control specimens that were anodized at 268 hr. We suspect, therefore, that there is some transfer of phosphorus during oxidation. Further, results from zirconium preanodized in aqueous KOH (1%) solutions have shown variable results that we tentatively attribute to transfer of phosphorus during oxidation. These suspicions will be checked by oxidizing in completely separate systems. The problems above also suggest that addition of H_3PO_4 to the steam might be effective in reducing oxidation.

Preliminary oxidation results from specimens preanodized in H_2SO_4, K_2SO_4, and K_3PO_4 solutions of various concentrations showing no inhibiting effects comparable to anodizing in H_3PO_4.

---

[12] M. L. Picklesimer, Anodizing as a Metallographic Technique for Zirconium-Base Alloys, ORNL-2296 (April 26, 1957).

[redacted]

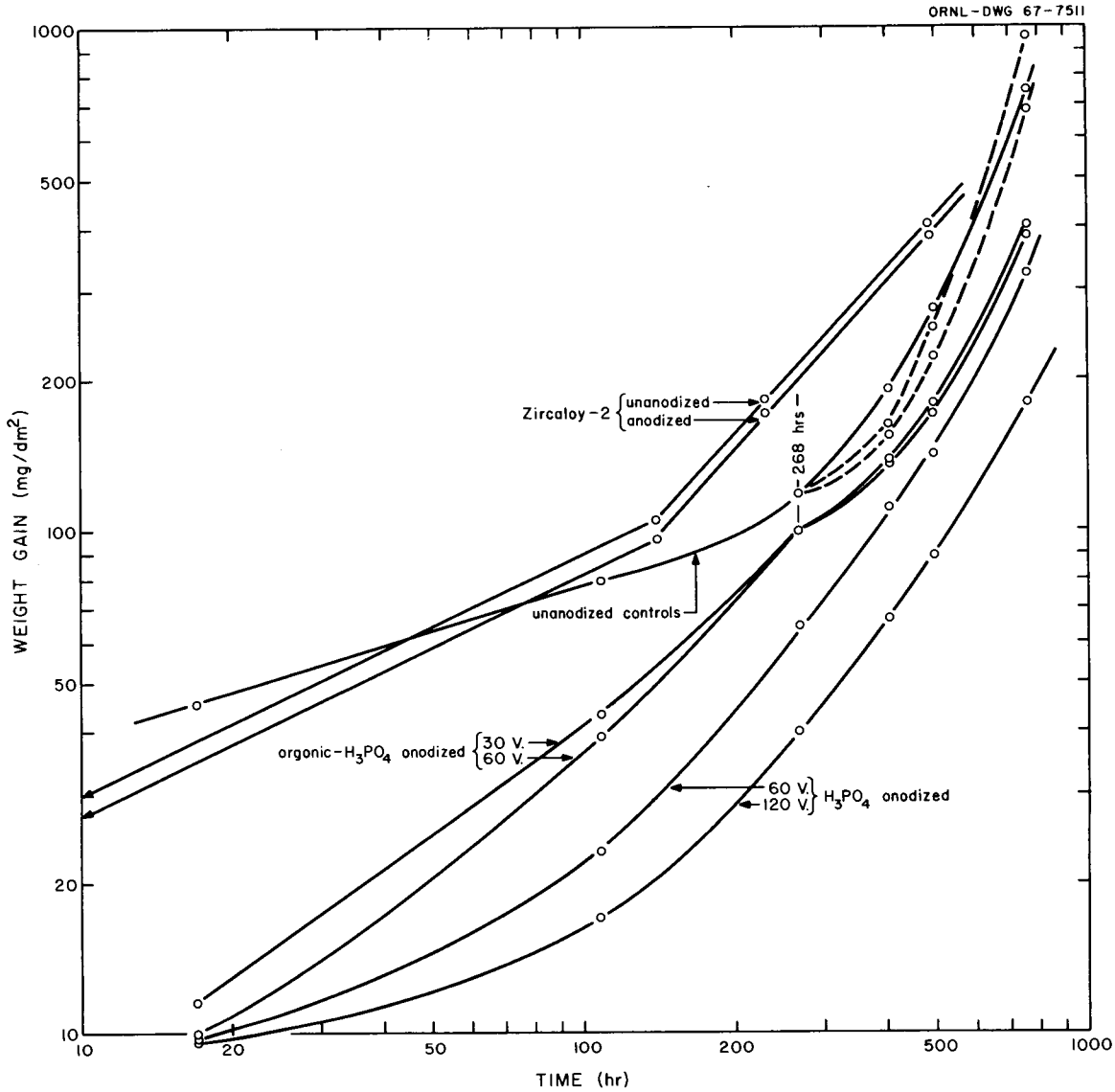

Fig. 5.5. Oxidation Weight Gain of Zirconium and Zircaloy-2. The inhibition of oxidation of vacuum-annealed (4 hr at 800°C) arc-melted crystal-bar zirconium and annealed (2 hr at 730°C) Zircaloy-2 in 500°C steam (15 psia) is shown. The anodizing solutions for zirconium were concentrated H_3PO_4 and an organic-H_3PO_4 solution; for Zircaloy-2 7 M H_3PO_4 was used. The dashed curves represent two of the original five control specimens that were anodized at 150 v in H_3PO_4 after 268 hr of exposure to steam. The zirconium specimens were electropolished; Zircaloy-2 specimens were chemically polished.

[redacted]

6. WELDABILITY OF NICKEL-BEARING ALLOYS

G. M. Slaughter

Studies are well under way on the program to determine the effects of minor elements, individually and combined, upon the cracking behavior and mechanical properties of welds in nickel-bearing alloys. Much of the effort in this reporting period, as well as the last, has been aimed at procuring high-purity raw materials and at fabricating special alloys for weldability testing both at Rensselaer Polytechnic Institute under subcontract and at ORNL. These materials procurement and alloy preparation phases of the investigation are relatively time-consuming and involve long lead times; the welding experiments are proceeding concurrently as specimens become available.

The properties of materials are greatly affected by structure. Energy input is one welding parameter which alters the structure of weld deposits. We are investigating heat input as a possible way of controlling the mechanical properties of weld metal in nickel- and iron-base alloys.

Special Alloy Fabrication

W. J. Werner D. A. Canonico
R. E. McDonald

Melting and fabrication have been completed for the first phase of the nickel- and iron-base alloy weldability program and specimens are being prepared for the various phases of the testing program. Excellent quality, reproducibility, and fabricability were obtained for all the alloys with the in-house melting and fabrication processes.

The iron-base alloy, Incoloy 800 (Fe—32.5 Ni, 21.0 Cr, wt %), was selected for weldability evaluation both at Rensselaer Polytechnic Institute under subcontract using the VARESTRAINT test[1] and at ORNL using the Duffer's Gleeble. VARESTRAINT specimens were made from pure

[1]Department of Materials Engineering, Rensselaer Polytechnic Institute, Troy, N. Y. Subcontract is funded jointly with BONUS Core II Superheater Research and Development.

ternary alloys, alloyed with aluminum and titanium within the range permitted by ASTM (0.60 max, weight percent of each). Table 6.1 shows the Incoloy 800 compositions selected for VARESTRAINT testing.

Alloys for hot-ductility testing were extended to include (in addition to the VARESTRAINT compositions) systematic additions of sulfur and phosphorus at intermediate aluminum and titanium levels. Table 6.2 shows the chemical analyses of the Incoloy 800 alloys for the hot-ductility tests.

The nickel-base alloy, Inconel 600 (Ni–8 Fe, 15.5 Cr, wt %) was also selected for weldability testing both at Rensselaer and at ORNL. In this case, the VARESTRAINT experiments are based on a factorial design and the special alloys include several levels of the residual elements, C, S, P, Mn, and Si. Six 125-lb heats of the pure ternary Inconel 600-base material were melted in-house and extruded and rolled at DuPont for this purpose.

Alloys for hot-ductility testing were based on a nominal composition containing 0.03 C, 0.04 Cu, 0.20 Mn, and 0.20 Si (wt %) together with systematic additions of sulfur and phosphorus. Table 6.3 shows the chemical analyses of these Inconel 600 type alloys.

VARESTRAINT Testing Performed Under Subcontract at Rensselaer Polytechnic Institute (W. F. Savage, C. D. Lundin)[1]

Testing at 1% augmented strain was completed on all the alloys shown in Table 6.1. The results of these tests are given in Table 6.4. A computer regression analysis study along with the results obtained previously on two commercial heats of Incoloy 800 will be carried out in an attempt to correlate the degree of cracking with the chemical analyses of the various heats. The analysis will include, as independent variables, all of the contaminants shown in Table 6.1 as well as their binary combinations. Dependent variables will be the four types of data obtained from crack measurement (Table 6.4). Hopefully, the computer study will indicate which elements or combinations of elements affect hot cracking. Electron microscopy and microprobe work can then be judiciously initiated.

Table 6.1. Nominal and Actual Compositions of the Incoloy 800 VARESTRAINT Specimens

Alloy Designation	Composition, wt %														ppm	
	Ni	Cr	Fe	C	H_2	N_2	O_2	S	P	Si	Al	Mn	Cu	Ti	B	Pb
800-1 nominal	32.5	21.0	bal													
(CVO-53)actual	32.7	20.9	45.9	0.004	0.0015	0.0026	0.019	0.004	0.004	<0.01	<0.05	<0.005	<0.01	<0.01	0.2	<2
800-2 nominal	32.5	21.0	bal								0.15			0.15		
(CVO-69)actual	33.6	20.8	45.0	0.007	0.0015	0.0026	0.010	0.004	<0.001	<0.01	0.21	<0.005	<0.01	0.17	1	<2
800-3 nominal	32.5	21.0	bal								0.60			0.60		
(CVO-77)actual	32.5	21.5	44.5	0.007	0.0016	0.0028	0.0079	0.004	<0.001	<0.01	0.81	<0.005	<0.01	0.52	0.6	<2
800-4 nominal	32.5	21.0	bal								0.38			0.38		
(CVO-82)actual	32.0	21.9	44.0	0.008	0.0007	0.0031	0.045	0.004	<0.001	<0.01	0.69	<0.005	<0.01	0.43	<0.2	<2
800-5 nominal	32.5	21.0	bal								0.38			0.15		
(CVO-94)actual	33.4	20.7	44.9	0.01	0.0007	0.0031	0.024	0.004	0.001	<0.01	0.48	<0.005	<0.01	0.13	0.2	<2
800-6 nominal	32.5	21.0	bal								0.38			0.60		
(CVO-162)actual	32.2	21.2	45.1	0.009	0.0009	0.0035	0.011	0.004	0.001	<0.01	0.39	<0.005	<0.01	0.54	<0.2	<2
800-7 nominal	32.5	21.0	bal								0.15			0.38		
(CVO-163)actual	33.1	19.6	45.9	0.007	0.0008	0.0022	0.034	0.003	0.001	<0.01	0.17	<0.005	<0.01	0.37	1	<2
800-8 nominal	32.5	21.0	bal								0.60			0.38		
(CVO-164)actual	35.2	21.4	42.1	0.006	0.0006	0.0011	0.0098	0.002	0.002	<0.01	0.57	<0.005	<0.01	0.29	1	<2

Table 6.2. Nominal and Actual Compositions of the Incoloy 800 Hot-Ductility Specimens

Alloy Designation	Composition, wt %														ppm	
	Ni	Cr	Fe	C	H_2	N	O_2	S	P	Si	Al	Mn	Cu	Ti	B	Pb
800-1 nominal	32.5	21.0	bal													
(CVO-53)actual	32.9	21.2	46.3	0.007	0.0004	0.0026	0.013	0.004	0.002	0.03	<0.05	0.02	<0.01	<0.01	4	<2
800-2 nominal	32.5	21.0	bal								0.15			0.15		
(CVO-175)actual	35.0	20.7	44.6	0.007	0.0003	0.0008	0.014	0.002	0.001	0.01	0.13	0.03	0.013	0.095	<0.2	<2
800-3 nominal	32.5	21.0	bal								0.38			0.38		
(CVO-176)actual	33.8	21.2	43.9	0.007	0.0005	0.0008	0.018	0.002	0.001	0.02	0.43	0.03	<0.01	0.44	<0.2	<2
800-4 nominal	32.5	21.0	bal								0.60			0.60		
(CVO-177)actual	33.8	21.0	43.2	0.006	0.0025	0.0004	0.021	0.002	0.002	0.03	0.52	0.03	<0.01	0.51	0.8	<2
800-5 nominal	32.5	21.0	bal								0.38			0.15		
(CVO-143)actual	34.6	20.6	44.0	0.007	0.0019	0.0022	0.024	0.004	0.001	<0.01	0.38	<0.005	<0.01	0.13	0.2	<2
800-6 nominal	32.5	21.0	bal								0.38			0.60		
(CVO-144)actual	32.2	22.0	44.0	0.009	0.0031	0.0035	0.043	0.004	0.001	≤0.01	00.35	<0.005	<0.01	0.54	4	<2
800-7 nominal	32.5	21.0	bal								0.15			0.38		
(CVO-145)actual	32.7	21.5	45.2	0.009	0.0018	0.0026	0.021	0.004	0.001	0.01	0.17	<0.005	<0.01	0.37	1	<2
800-8 nominal	32.5	21.0	bal								0.60			0.38		
(CVO-146)actual	31.9	21.9	44.7	0.008	0.0020	0.0030	0.022	0.004	0.001	<0.01	0.54	<0.005	<0.01	0.35	<0.2	<2
800-9 nominal	32.5	21.0	bal					0.01			0.38			0.38		
(CVO-184)actual	33.2	20.8	44.3	0.006	0.0022	0.0011	0.013	0.007	0.001	<0.01	0.37	<0.005	<0.01	0.35	0.2	<2
800-10 nominal	32.5	21.0	bal					0.015			0.38			0.38		
(CVO-185)actual	32.0	21.3	44.9	0.006	0.0014	0.019	0.022	0.010	0.001	<0.01	0.30	<0.005	<0.01	0.33	0.3	<2
800-11 nominal	32.5	21.0	bal					0.02			0.38			0.38		
(CVO-186)actual	32.6	21.1	43.8	0.005	0.0002	0.0004	0.012	0.015	0.001	≤0.01	0.33	<0.005	1.6	0.31	0.3	<2
800-12 nominal	32.5	21.0	bal						0.01		0.38			0.38		
(CVO-187)actual	33.1	21.2	43.7	0.007	0.0002	0.0002	0.012	0.003	0.011	<0.01	0.33	<0.005	<0.01	0.33	<0.2	<2
800-13 nominal	32.5	21.0	bal						0.015		0.38			0.38		
(CVO-188)actual	32.5	21.3	45.4	0.007	0.0002	0.0009	0.0083	0.002	0.010	0.05	0.34	0.07	<0.01	0.38	0.2	<2
800-14 nominal	32.5	21.0	bal						0.02		0.38			0.38		
(CVO-189)actual	32.3	21.1	44.8	0.006	0.0005	0.0007	0.020	0.002	0.015	≤0.01	0.32	0.02	<0.01	0.31	0.2	<2
800-15 nominal	32.5	21.0	bal					0.01	0.01		0.38			0.38		
(CVO-190)actual	33.3	21.6	45.2	0.006	0.0004	0.0007	0.023	0.008	0.010	≤0.01	0.36	<0.005	<0.01	0.33	0.2	<2
800-16 nominal	32.5	21.0	bal					0.015	0.015		0.38			0.38		
(CVO-191)actual	31.9	21.6	44.8	0.006	0.0003	0.0018	0.020	0.010	0.013	<0.01	0.40	<0.005	0.015	0.40	≤0.2	<2

Table 6.3. Nominal and Actual Compositions of the Inconel 600 Gleeble Specimens

Designation	Composition, wt %														ppm	
	Ni	Cr	Fe	C	H_2	N_2	O_2	S	P	Si	Al	Mn	Cu	Ti	B	Pb
600-1 nominal	bal	15.5	8													
(CVO-147)actual	75.2	15.9	8.13	0.004	0.0011	0.0004	0.019	0.003	0.001	0.01	<0.05	0.007	<0.01	<0.01	1	<2
600-2 nominal	bal	15.5	8	0.03						0.20		0.20	0.04			
(CVO-148)actual	75.6	16.1	8.55	0.028	0.0002	0.0010	0.0081	0.002	0.002	0.2	<0.05	0.11	0.026	<0.01	1	<2
600-3 nominal	bal	15.1	8	0.03				0.005		0.20		0.20	0.04			
(CVO-149)actual	75.2	16.0	8.40	0.028	<0.0001	0.0004	0.0005	0.006	0.001	0.2	<0.05	0.11	0.022	<0.01	1	<2
600-4 nominal	bal	15.5	8	0.03				0.010		0.20		0.20	0.04			
(CVO-150)actual	74.7	15.5	8.04	0.025	0.0002	0.0005	0.0025	0.010	0.002	0.2	<0.05	0.15	0.029	<0.01	2	<2
600-5 nominal	bal	15.5	8	0.03				0.015		0.20		0.20	0.04			
(CVO-151)actual	74.5	15.7	8.32	0.026	0.0005	0.0010	0.0061	0.012	0.002	0.2	<0.05	0.12	0.18	<0.01	<0.2	<2
600-6 nominal	bal	15.5	8	0.03					0.005	0.20		0.20	0.04			
(CVO-152)actual	70.9	15.9	12.1	0.027	0.0008	0.0013	0.0079	<0.002	0.006	0.2	<0.05	0.23	0.021	<0.01	0.3	<2
600-7 nominal	bal	15.5	8	0.03					0.010	0.20		0.20	0.04			
(CVO-153)actual	73.7	15.8	9.33	0.026	0.0029	0.0018	0.017	<0.002	0.011	0.2	<0.05	0.20	0.021	<0.01	0.3	<2
600-8 nominal	bal	15.5	8	0.03					0.015	0.20		0.20	0.04			
(CVO-154)actual	72.6	15.9	10.4	0.023	0.0025	0.0028	0.082	<0.002	0.015	0.3	<0.05	0.17	0.018	<0.01	0.3	<2
600-9 nominal	bal	15.5	8	0.03				0.0025	0.0025	0.20		0.20	0.04			
(CVO-155)actual	72.6	16.2	11.4	0.034	0.0021	0.0016	0.0075	0.003	0.004	0.2	<0.05	0.16	0.024	<0.01	0.4	<2
600-10 nominal	bal	15.5	8	0.03				0.005	0.005	0.20		0.20	0.04			
(CVO-156)actual	72.3	16.2	11.5	0.026	0.0029	0.0011	0.018	0.003	0.006	0.2	<0.05	0.17	0.023	<0.01	0.7	<2
600-11 nominal	bal	15.5	8	0.03				0.0075	0.0075	0.20		0.20	0.04			
((CVO-157)actual	73.7	16.1	8.98	0.026	0.0019	0.0007	0.0079	0.006	0.008	0.2	<0.05	0.17	0.018	<0.01	0.2	<2
600-12 nominal	bal	15.5	8	0.03				0.010		0.20		0.40	0.04			
(CVO-158)actual	75.6	16.2	8.28	0.033	0.0009	0.0015	0.0086	0.009	0.002	0.2	<0.05	0.32	0.021	<0.01	0.2	<2
600-13 nominal	bal	15.5	8	0.03				0.010		0.20		0.60	0.04			
(CVO-159)actual	75.4	15.9	8.11	0.022	0.0012	0.0015	0.012	0.009	0.002	0.2	<0.05	0.48	0.024	<0.01	0.4	<2
600-14 nominal	bal	15.5	8	0.03				0.010		0.20		0.80	0.04			
(CVO-160)actual	75.2	16.0	9.05	0.026	0.0002	0.0013	0.016	0.009	0.002	0.2	<0.05	0.84	0.029	<0.01	0.4	<2
600-15 nominal	bal	15.5	8	0.03				0.010	0.010	0.20		0.80	0.04			
(CVO-161)actual	72.5	16.6	11.3	0.026	0.0005	0.0008	0.011	0.008	0.007	0.2	<0.05	0.80	0.022	<0.01	0.5	<2

[redacted]

Table 6.4. Results of VARESTRAINT Testing of Special Incoloy 800 Compositions[a]

Alloy Designation	Sample Preparation			
	As-Welded		Polished	
	Crack Length		Crack Length	
	Total	Maximum	Total	Maximum
800-1	206	21	19	19
(CVO-59)	297	21	0	0
800-2	459	65	187	46
(CVO-69)	427	50	250	40
800-3	414	73	187	54
(CVO-77)	536	83	293	70
800-4	355	52	342	52
(CVO-82)	359	50	349	51
800-5	241	41	258	34
(CVO-94)	159	33	371	35
800-6	334	75	358	63
(CVO-162)	338	60	330	60
800-7	117	52	154	49
(CVO-163)	164	43	206	50
800-8	170	38	118	20
(CVO-164)	98	27	125	21
Commercial	769	100	590	190
Heat No. 1786	441	100	404	100

[a]Duplicate samples tested at 1% augmented strain.

Test Development

A second-generation VARESTRAINT-type device, nicknamed the "TIG-A-MA-JIG," has been designed to utilize the good points of its predecessor and to add several refinements. A sketch of the apparatus is shown in Fig. 6.1. Basic operation is similar to the VARESTRAINT in that an augmented strain is imposed on the sample while a gas tungsten-arc weld is being made. However, the new test specimen is considerably smaller than its predecessor and is, therefore, more economical to prepare. The weld is of the stationary tungsten-arc type. Provisions are included for automatic loading of the sample after an adjustable preset welding time of 2 to 120 sec. A timer is included in the control circuit to delay weld current cutoff for a period of up to 1 sec after loading.

[redacted]

[redacted]

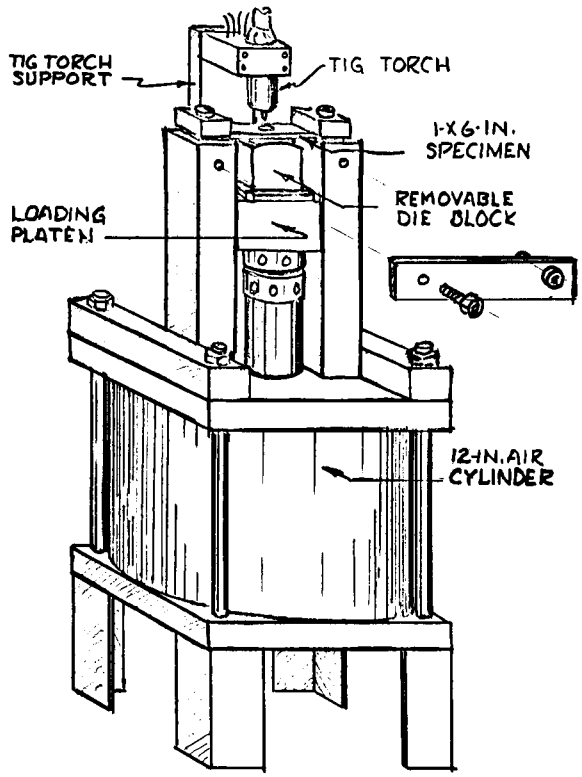

Fig. 6.1. Sketch of the "TIG-A-MA-JIG." (Rennselaer Polytechnic Institute drawing).

The Effect of Energy Input on the Mechanical Properties of Austenitic Stainless Steel Welds

D. A. Canonico W. R. Martin

The mechanical properties of carbon- and low alloy-steel welds are significantly affected by variations in welding parameters. These changes in mechanical properties are largely related to refinement or coarsening of the ferritic microstructure during cycling through the face-centered cubic to body-centered cubic allotropic transformation range. Unlike welds in ferritic steels, austenitic stainless steel welds do not undergo allotropic transformations and, therefore, cannot be affected in this way.

However, one possible way of controlling the mechanical properties of weld metal in such an alloy is by changing the mode of solidifications. To evaluate the influence of weld energy input on the solidification mode in tungsten-arc welds, a cursory bead-on-plate study was undertaken using

[redacted]

welding conditions producing 10,000, 20,000, and 40,000 joules/in. Type 308 stainless steel filler metal was deposited on type 304 stainless steel-base metal, using a cold-wire feed mechanism. The results of this study showed that obvious microstructural differences (i.e., dendrite spacing, delta ferrite distribution, etc.) did indeed prevail; furthermore, microhardness studies indicated that strength differences should exist between welds made with the three energy inputs.

The program was then extended to actual butt welds on highly restrained plates. The joint designs were selected to provide both transverse all-weld-metal and transverse weldment (base metal, heat-affected zone, and weld metal) specimens. The weldment specimens and one set of all-weld-metal specimens were made with one heat of filler metal (W-1). A second set of all-weld-metal specimens were made with a different heat of filler metal (W-2). An additional energy input level, 60,000 joules/in., was also added for this second study. The analyses of the two filler wires indicated that they both possessed about 8% of delta ferrite as determined from the Schaeffler diagram.[2]

The effect of heat input on the W-2 weld-metal microstructure is shown in Fig. 6.2. The white phase seen in these photomicrographs is austenite, while the darker and more defined phase is delta ferrite. The approximate intercellular distances for the microstructures are 7, 12, 16, and 20 μ, respectively, for the 10,000, 20,000, 40,000, and 60,000 joules/in. welds.

Metallographic samples of these welds were also scanned in the quantitative television microscope (QTM) wherein relative amounts of each phase are directly measured. The results indicated that the ferrite level for a given heat input ranged from approximately 4 to 9%.

The effect of heat input on the ultimate tensile strength of both heats of weld metal is shown in Fig. 6.3. There is approximately a 10,000-psi difference at room temperature between the welds made at 10,000 and those made at 60,000 joules/in. This advantage decreased as the testing temperature increased.

---

[2]A. L. Schaeffler, "Selection of Austenitic Electrodes for Welding Dissimilar Metals," Welding J. (N.Y.) 26(10), 601-s–620-s (October 1947).

[redacted]

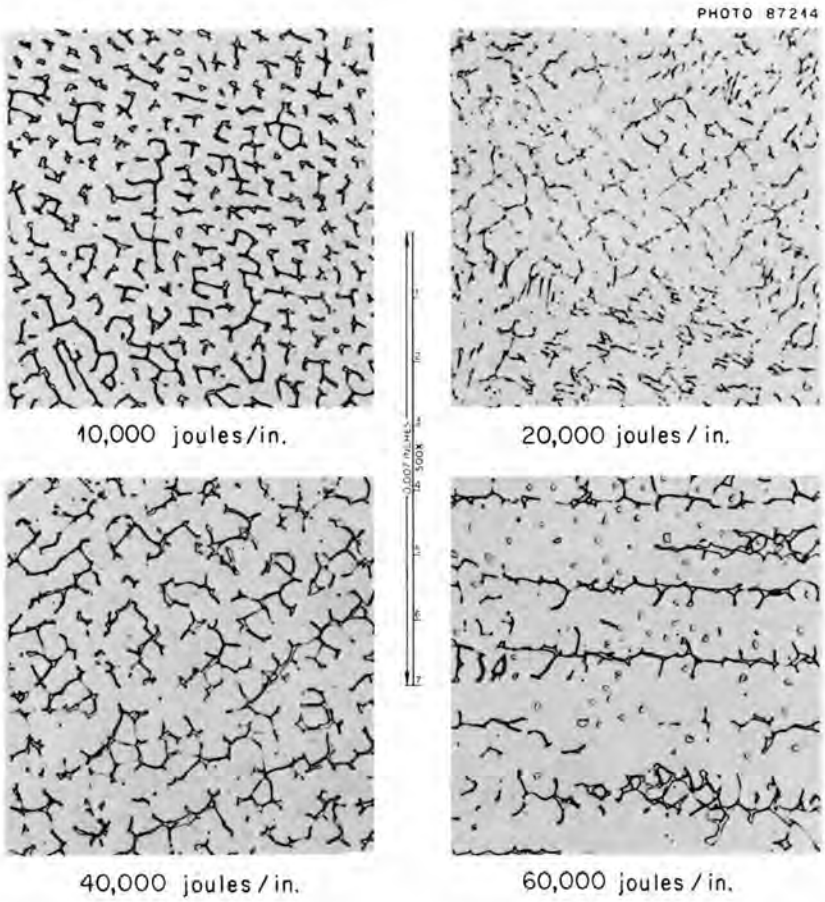

Fig. 6.2. Effect of Heat Input on Type 308 Stainless Steel Weld Metal Microstructure.

The ductility measurements for the two welds were quite similar at the 10,000 and 20,000 joules/in. energy inputs. However, they were conspicuously different for the higher levels of heat input. At the 40,000 value, the W-1 welds had a ductility (as measured by elongation) considerably less than that obtained for W-2. A metallographic investigation showed that the W-1 weld deposited at 40,000 joules/in. contained no ferrite. An analysis of the deposited weld metal showed a distinct loss of chromium in this 40,000 joules/in. W-1 weld; the lower chromium content will result in a marked decrease in the amount of delta ferrite in the weld metal.

[redacted]

[redacted]

ORNL-DWG 67-3956R

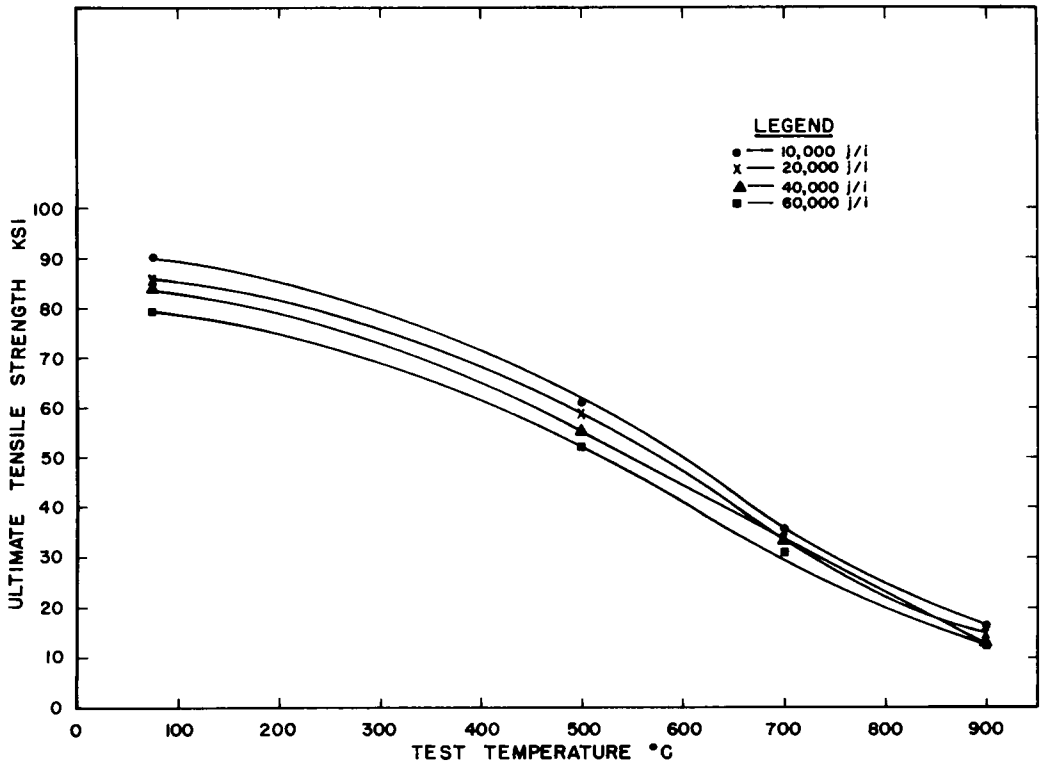

Fig. 6.3. The Effect of Heat Input on the Ultimate Tensile Strength of Weld Metal.

The results of this study indicate that heat input significantly affects the mechanical properties of stainless steel weld metal. This effect is probably related to such factors as intercellular distance and actual delta ferrite content.

[redacted]

[redacted]

PART II.

REACTOR CHEMISTRY DIVISION

[redacted]

[redacted]

[redacted]

7. FISSION-GAS RELEASE AND PHYSICAL PROPERTIES OF FUEL MATERIALS DURING IRRADIATION

R. M. Carroll R. B. Perez[1]
J. G. Morgan O. Sisman

Fission-gas release from UO_2 is being studied in an effort to determine the mechanism by which the gas migrates and escapes from the fuel. From these studies we hope to develop a model to make engineering calculations of noble gas escape from operating fuel materials. Our experimental method is to irradiate carefully selected and characterized specimens in an irradiation facility where the neutron flux and temperature are controlled independently. Fission gas released from the specimen is entrained in a moving stream of sweep gas and carried outside the reactor where it is analyzed by gamma-ray spectrometry.

A defect-trap model of fission-gas release has been developed and two methods are used to evaluate the coefficients of the model. One is the steady-state method, wherein the gas release is measured while irradiation conditions are constant. In the other method the specimen is oscillated sinusoidally in the reactor so as to oscillate the neutron flux and the specimen temperature. Waves of fission-gas release are produced by the oscillations, and analyses of these waves gives the necessary additional degree of freedom in fitting a model to the data.

This oscillation method offers promise of being a good way to measure thermal diffusivity during irradiation since the time lag between a change of fission heating and the resultant change of temperature depends on the diffusivity of the specimen. For this reason, a hollow cylinder specimen of single-crystal UO_2 was used to develop the instrumentation and techniques for both the thermal diffusivity and the dynamic fission-gas release method.

---

[1]Consultant from the University of Florida.

[redacted]

Steady-State Fission-Gas Release from UO_2 Single-Crystal Specimen C1-19

The specimen has been irradiated for an estimated 8.6×10^{19} fissions/cm^3 total burnup, about one-half the original ^{235}U content. Measurements were made just after irradiation began and later after about 8×10^{19} fissions/cm^3 burnup. At the beginning of irradiation, the temperature was limited to 1400°C lest we damage the specimen for thermal diffusivity measurements. After the thermal diffusivity experiments, we were free to operate at temperatures up to 1700°C.

As expected by the defect-trap theory, we found that the fission-gas release was not strongly influenced by the fission rate while the specimen was at high temperatures (see Fig. 7.1). This specimen had a somewhat larger geometric surface area than the disk specimens we have been irradiating (8.7 compared to approximately 6 cm^2). Also, the manufacturing method of the hollow-cylinder specimen produced a rougher surface than that on the disk specimens, resulting in a considerably larger total surface area.

At the beginning of irradiation the gas release was about as expected of a specimen of single-crystal UO_2 with an approximate 9 cm^2 geometric surface area. After about 8×10^{19} fissions/cm^3 burnup we observed three changes: (1) the fission-gas release rate had increased; (2) the activation energy for release had changed; and (3) the gas release now had a strong dependence on the immediate irradiation history. The first two points are illustrated in Fig. 7.1.

Past experiments have shown that at the start of irradiation the fission-gas release decreases with burnup. This is a result of a buildup of trapping sites. In the present experiment we have observed an increase of gas release which we believe to be caused by the specimen breaking because of thermal stresses, thus increasing the surface area of the specimen.

[redacted]

[redacted]

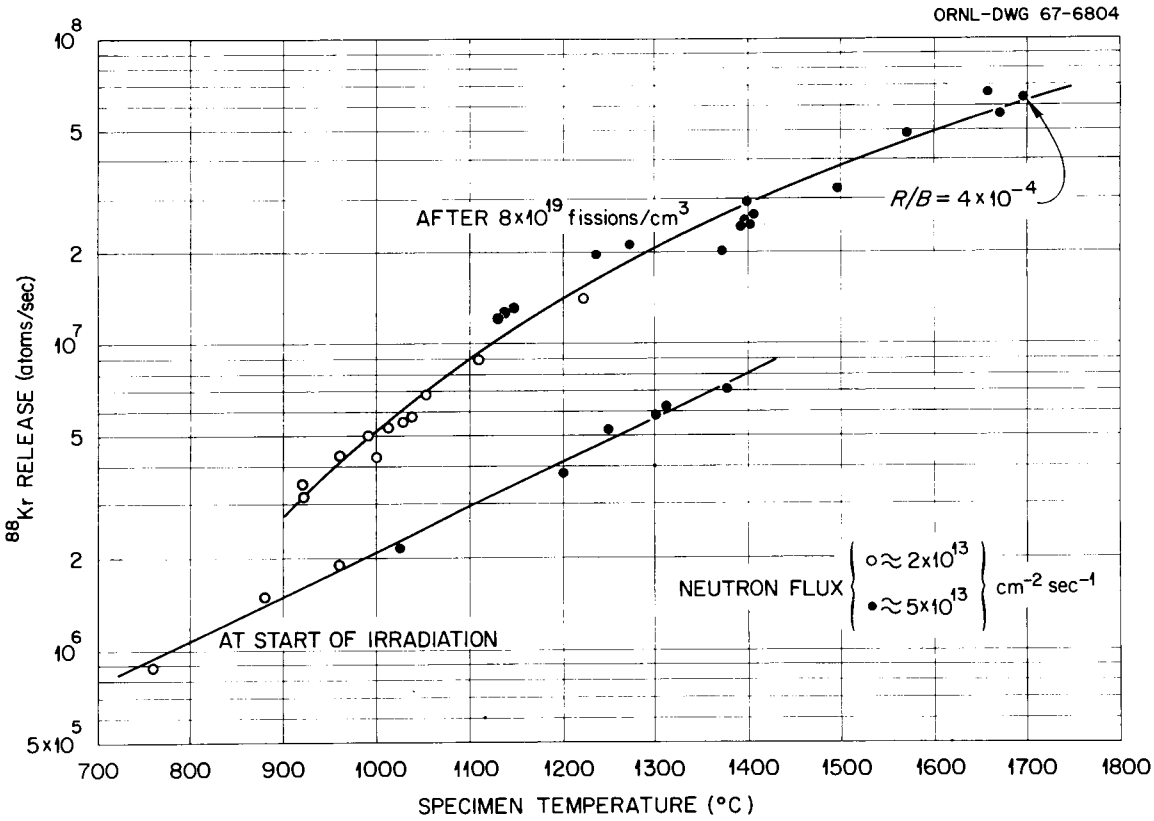

Fig. 7.1. Uranium Dioxide Single-Crystal (C1-19) Release Rate of ^{88}Kr after Equilibrium Times.

If the data of Fig. 7.1 is plotted as an Arrhenius plot (see Fig. 7.2) gas release rate at low burnup shows a change of activation energy at about 1100°C. We have previously explained this change as being caused by the migration of clusters of point defects rather than by individual point defects.[2] Note that the activation energy of the gas release after burnup to 8×10^{19} fissions/cm^3 is the same as that at the beginning of irradiation for temperatures greater than 1100°C. The data of Fig. 7.2 suggest that the dominant gas release after 8×10^{19} fissions/cm^3 is by release from migrating clusters even at temperatures as low as 900°C.

The theory of defect-cluster migration is substantiated by the short history dependence of the specimen after 8×10^{19} fissions/cm^3 burnup. By our past experience, when a specimen of UO_2 is cooled from

[2]R. M. Carroll, R. B. Perez, J. G. Morgan, and O. Sisman, Fuels and Materials Development Program Quart. Progr. Rept. Dec. 31, 1966, ORNL-TM-1720, p. 93.

[redacted]

[redacted]

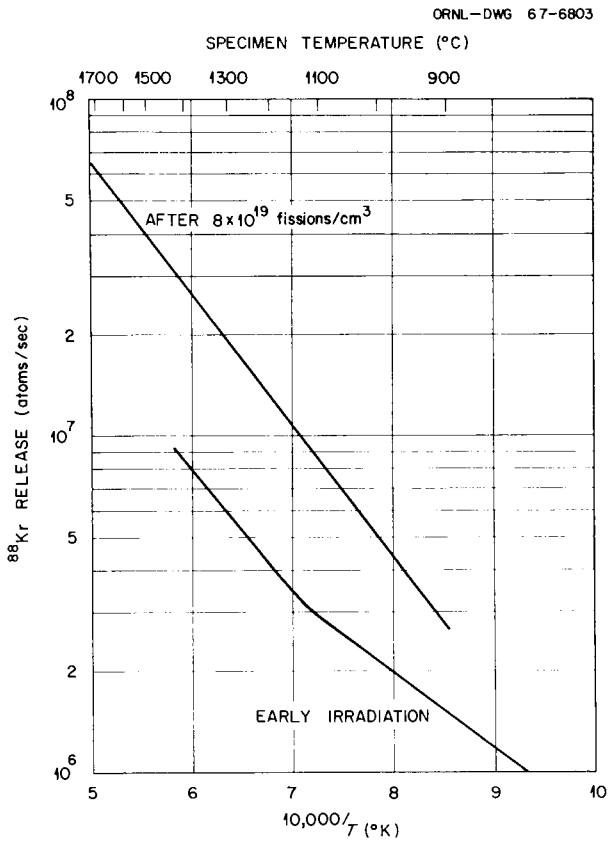

Fig. 7.2. Temperature Dependence of UO_2 Single-Crystal (Cl-19) ^{88}Kr Release Rate.

one steady-state temperature to another, the gas release decreases smoothly to its new steady-state level. This observation was one of the reasons we did not believe the gas release was by a pure diffusion process. By diffusion theory, a heating burst is found when the specimen temperature is increased (for temperatures greater than about 700°C). By the same token, when a specimen is cooled we would expect a dip in the gas release rate. After long irradiation we do observe a dip in the gas release rate from this specimen (see Fig. 7.3). This observation, coupled with the change in activation energy with burnup, indicates to us that clusters are diffusing. This conclusion is consistent with the prediction of the defect-trap theory that the clustered traps would become more important at higher temperatures and as burnup progressed. A study of fission-gas release at high burnups is scheduled for later this year.

[redacted]

[redacted]

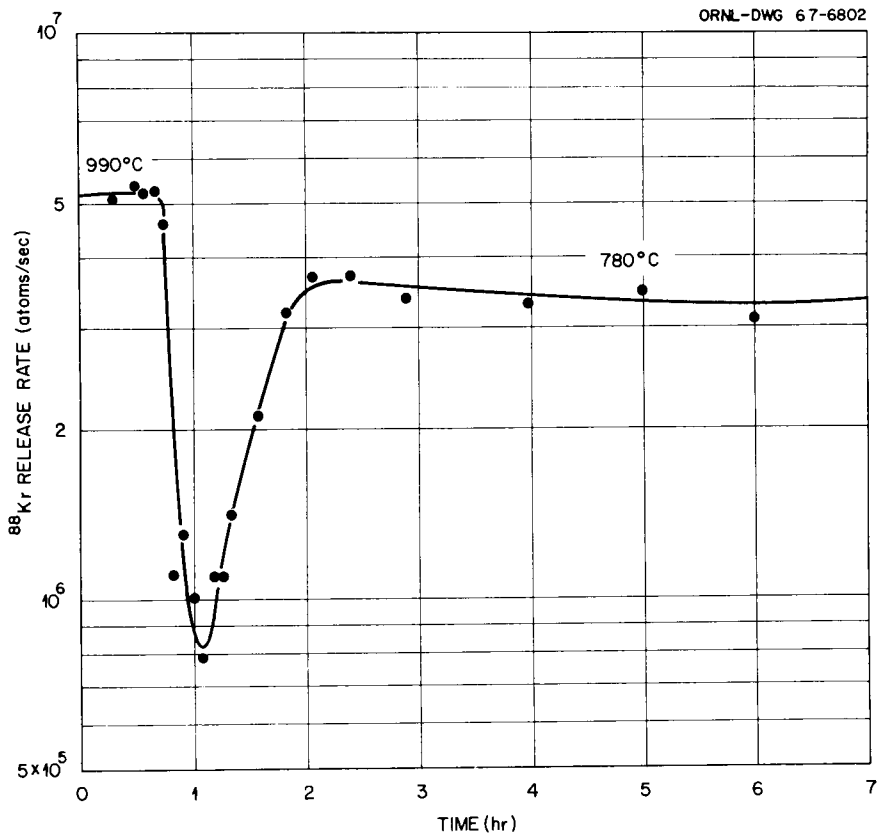

Fig. 7.3. Release of ^{88}Kr When Temperature of Single-Crystal UO_2 Specimen (C1-19) Was Reduced from 990 to 780°C at Constant Neutron Flux (after 8×10^{19} fissions/cm^3 burnup).

Low-Temperature, Knockout Release

Low-temperature gas-release experiments were not made on the hollow cylinder, single-crystal specimen until after about 8×10^{19} fissions/cm^3 burnup. As one would expect, from the high-temperature release, an unusually large surface area was indicated by the magnitude of the low-temperature release. A comparison with previous measurements on disk-type specimens is shown in Fig. 7.4.

We have shown that at low temperatures the gas release is mainly by a knockout process rather than by direct recoil of fission fragments, and that one would not expect a linear relation between fission rate and gas released by the knockout process (where the fission fragment knocks molecules of UO_2 and fission products from the specimen as it passes through the surface). We explained the observed linear relation as

[redacted]

[redacted]

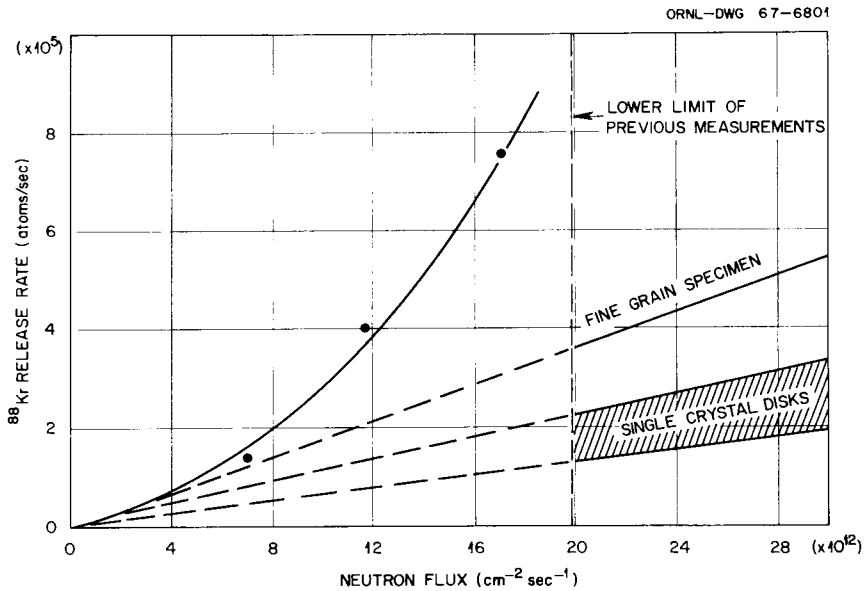

Fig. 7.4. Low-Temperature Release of ^{88}Kr from Single-Crystal Specimen (Cl-19).

being caused by knockout from a thin saturated layer at the specimen surface.[3]

The specimen in this experiment was heavily insulated to meet a requirement of the thermal tests. Thus, in order to obtain temperatures below 600°C, it was necessary to use very low neutron flux levels. Since the concentration of ^{88}Kr within the specimen was directly proportional to the neutron flux, the large surface area of the specimen apparently was not saturated with ^{88}Kr at the low flux levels. Therefore, a linear relation between neutron flux and ^{88}Kr release was not obtained (see Fig. 7.4).

If the data of Fig. 7.4 are plotted versus the neutron flux squared, then a linear relation is obtained as would be expected from the knockout process from an unsaturated surface layer.[3] This is further proof that the low-temperature release is by a knockout rather than a direct recoil process.

---

[3]R. M. Carroll and O. Sisman, "In-Pile Fission-Gas Release from Single-Crystal UO_2," Nucl. Sci. Eng. 21, 147–158 (1965).

[redacted]

[redacted]

The Mixing of a Trace Gas in Flowing Helium

When fission gas emerges from the specimen, it is entrained in a constantly moving stream of sweep gas and carried outside the reactor for analysis. When the fission gas is released in waves during oscillation of specimen temperature, the measured waves become distorted as they mix in the sweep gas during transit from the capsule to the spectrometer. In order to relate the measured wave shape to the wave shape generated by the specimen, we had to determine the mixing transfer function of the sweep-gas system (see Fig. 7.5).

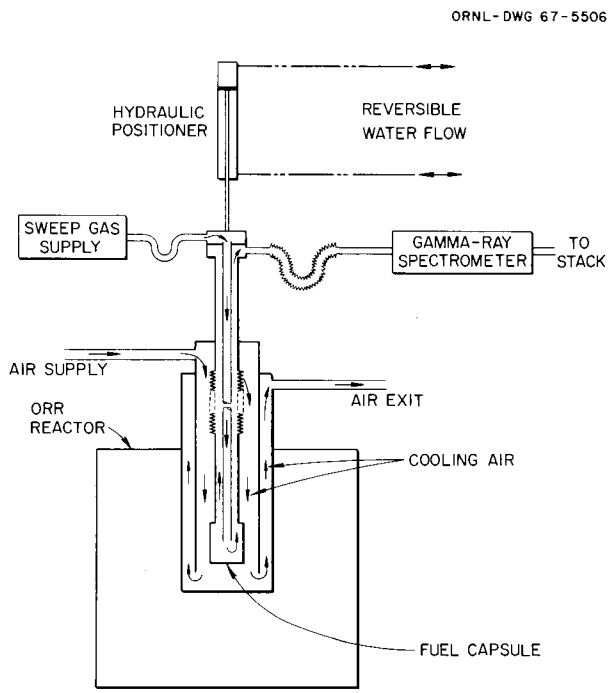

Fig. 7.5. Schematic Flow Diagram of Sweep Gas During the Specimen Irradiation.

A full-scale duplicate of the experiment piping system was constructed. A small pulse of argon was injected into a steady flow of helium to simulate a pulse of fission gas (Fig. 7.6). The argon concentration within the helium was measured by a thermal conductivity cell just after injection and then again after it passed through the piping system (see Fig. 7.7). The time-concentration data of each pulse were

[redacted]

[redacted]

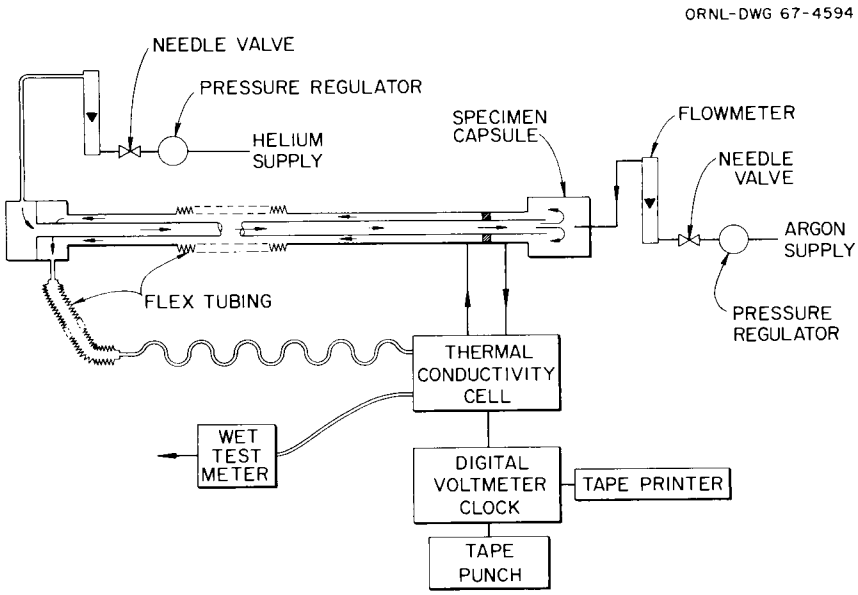

Fig. 7.6. Flow Diagram of Dynamic Experiment.

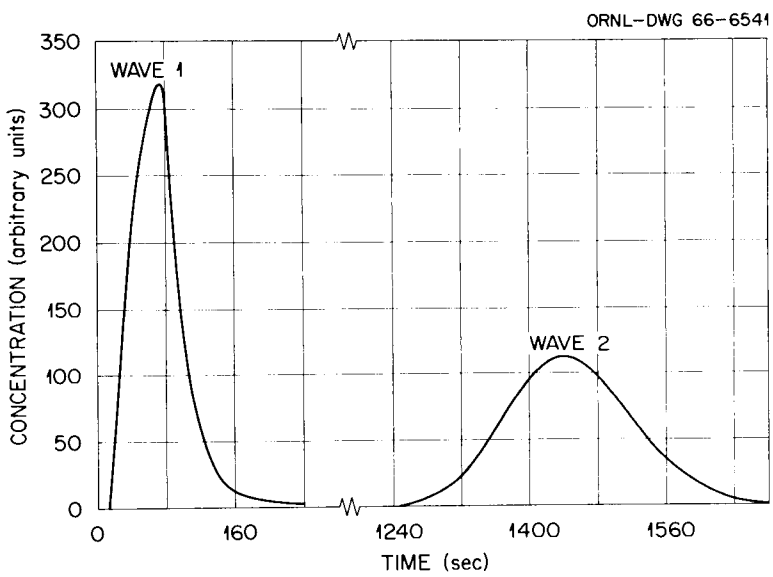

Fig. 7.7. Mixing of Argon in Helium Sweep Gas; Flow 1.114 cm^3/sec.

inserted into a computer program for a Fourier analysis, yielding amplitude and angle values for the frequency spectrum of the pulse.

We have previously reported[4] that a limited theoretical treatment by Prados and Scott (assuming smooth-walled tubing) had been placed in

[4]R. M. Carroll, R. B. Perez, J. G. Morgan, and O. Sisman, Fuels and Materials Development Program Quart. Progr. Rept. June 30, 1966, ORNL-TM-1570, pp. 79–85 [redacted]

[redacted]

a time-dependent version to conform to our experimental method. We have found that this analysis did not fit the measured data, likely because of the amount of mixing that occurs within the flex tubing and in the various chambers. Mainly, the analysis does not describe the sharp decrease of the transfer function amplitude for higher frequencies as was experimentally observed (see Fig. 7.8).

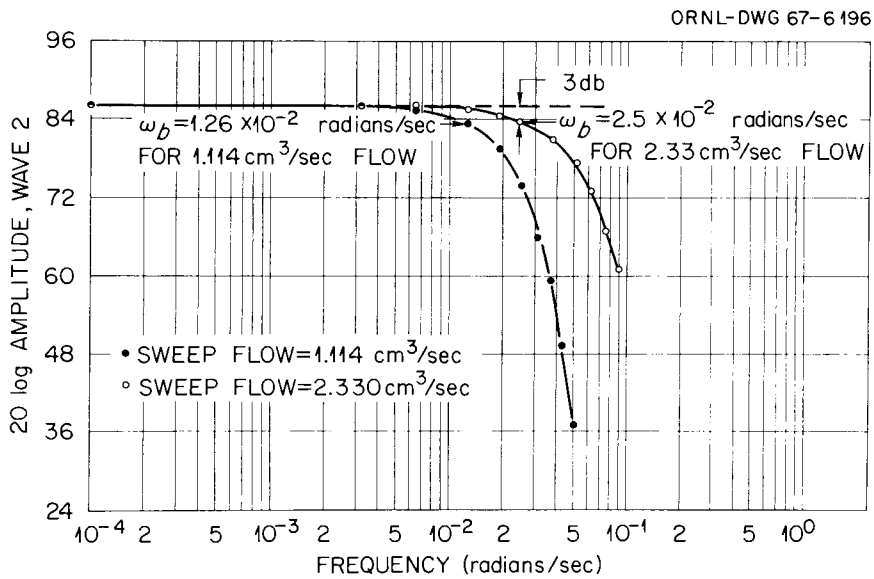

Fig. 7.8. Variation of Transfer Function Amplitude for Higher Frequencies.

Although the mixing transfer function for this particular system was determined empirically by this experiment, we wished to develop a working theory since very little work has been done in this field. In particular, the theory may be of relevance in the control of nuclear power plants where it is generally assumed that the flow of the coolant in the piping is in the form of slug flow.

The theoretical model for the mixing transfer function has been completed. The essence of the theoretical model is the realization that, although the experiment conditions yield a low Reynolds number (laminar flow), the geometric factors of the experiment, such as corrugated inner surfaces of tubing as well as bends and chambers, produce enough mixing

[redacted]

[redacted]

to alter or completely erase the parabolic radial dependence of the flow velocity typical of the laminar regime.

In brief, the theoretical model assumes axial turbulent flow (of linear velocity, v) with a flat radial distribution. The material balance of the argon concentration, $C(z,i\omega)$, is

$$\left\{\frac{\partial^2}{\partial x^2} - \frac{1}{\tilde{\ell}}\frac{\partial}{\partial z} - \frac{i\omega}{\tilde{D}}\right\} C(z,i\omega) = 0 \ ,$$

where

$\tilde{\ell}$ = mixing length (centimeters) in the axial direction, z
$\tilde{D}$ = turbulent diffusion coefficient.

The solution, valid for frequencies (ω) up to 10^{-1} radians/sec, gives the expressions for the amplitude (H_M) and the phase ($\theta_2 - \theta_1$) of the mixing transfer function as

$$|H_M\ (z,\omega)| = H_o \exp - (\tau\ \tilde{\tau}\ \omega_2) \ ,$$

and

$$(\theta_2 - \theta_1) = \tau\omega \ ,$$

where

τ is the transit time for a slug of gas between the measuring points,
$\tilde{\tau} = \tilde{\ell}/v$ is the mixing time.

Within the limits of this experiment the phase lag corresponds to slug flow (see Figs. 7.9 and 7.10). However, the amplitude is dependent on frequency, which does not correspond to slug flow. The agreement between the experiment and the theoretical model is excellent (see Table 7.1) and yields the basis for the necessary corrections for in-reactor time-dependent experiments.

[redacted]

[redacted]

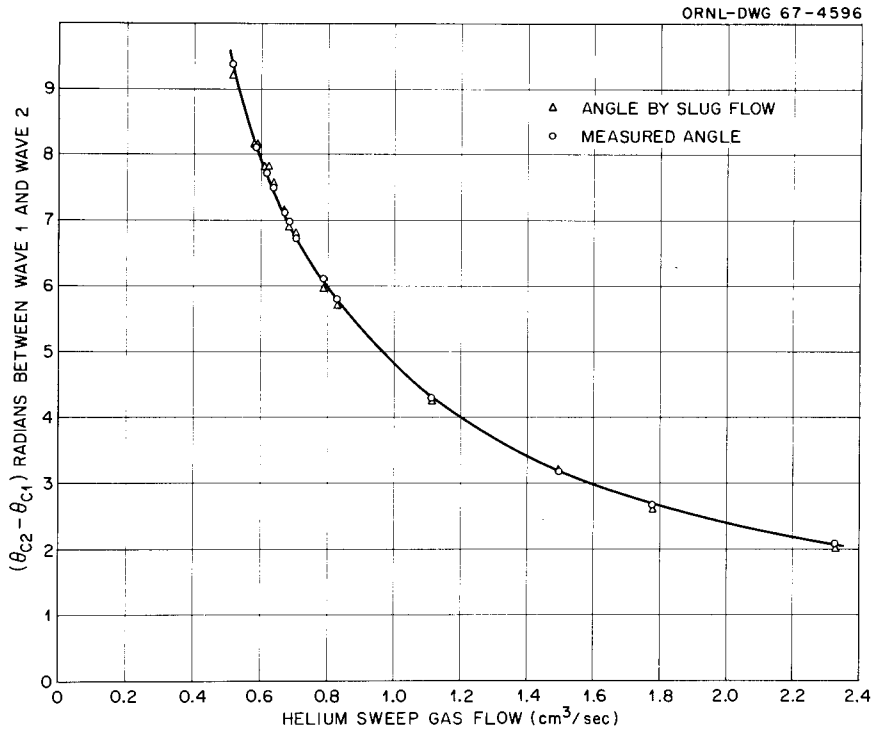

Fig. 7.9. Phase Shift Calculated and Measured for a Frequency of 3.14×10^{-3} radians/sec.

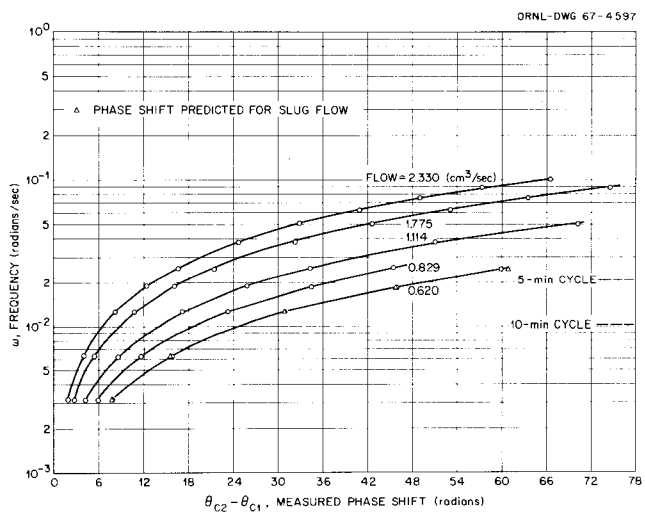

Fig. 7.10. Phase Shift Corrections for Measured Wave.

[redacted]

[redacted]

Table 7.1. Experimental and Theoretical Mixing Transfer Function[a]

ω (radians/sec)	H_M (decibels)		$\theta_2 - \theta_1$ (radians)	
	Experimental	Theoretical	Experimental	Theoretical
6.28×10^{-3}	85.6	85.5	8.7	8.5
1.88×10^{-2}	79.7	79.5	25.9	25.6
3.14×10^{-2}	67.3	67.0	42.8	42.6
4.4×10^{-2}	49.1	49.0	59.9	59.7
5.03×10^{-2}	37.4	37.7	70.5	68.2

[a]Flow = 1.114 cm^3/sec.

Thermal Diffusivity of Single-Crystal UO_2 During Irradiation

A hollow cylinder, single-crystal UO_2 specimen has been irradiated for the primary purpose of developing a dynamic method of measuring thermal diffusivity during irradiation. We first used the oscillation technique where the specimen responses were measured while the frequency of oscillation was changed. This method produced data that appeared good and computer methods of processing the data were developed. When final answers were obtained, however, the results showed too much scatter to be useful.

There were two possible causes for the data scatter. First, the mathematical analysis involved a transform that was very sensitive to small temperature differences. Second, several days were required to obtain the frequency spectrum for several different specimen temperatures. Although we used great care to adjust the experiment to compensate for changing reactor conditions, the reactor changes would produce some data scatter.

As a support program, we had measured the response of thermocouples to dynamic conditions by the use of a pulse method. The success of the pulse method on thermocouple measurements suggested that we could apply it to in-reactor diffusivity measurements. The great advantage of pulse testing is that irradiation conditions remain constant during the 15 min

[redacted]

required for a pulse test. Also, since all oscillation frequencies are contained within a pulse, we could obtain higher frequencies than with mechanical systems.

To make the pulses, we added a small fast-acting positioning-cylinder which rides piggyback on the main positioning cylinder. The main cylinder was used to locate the specimen at a specific neutron flux level, the air cooling was adjusted to obtain the desired temperature, and then the small cylinder was used to make a rapid step change of position in the neutron flux. The temperature change in response to the fission heating change was recorded by a high-speed data scanner and placed on punch tape.

Although (theoretically) all frequencies are contained within a pulse, in practice only a limited frequency can be obtained before the analysis will become inaccurate. An essential point in the mathematical treatment of the data is that we must obtain data at a frequency high enough so that a "break frequency" in the phase and amplitude response can be obtained. The oscillation method was failing just as this point was obtained, and a slight extension of frequency would have produced the desired results. Unfortunately, in the case of this particular single-crystal specimen, the phase analysis also collapsed just before the break frequency was obtained. The results were so near to the required point that we have spent considerable time trying to obtain the small extension of frequency range necessary for the method.

It now seems that the interaction of the thermocouple response and the UO_2 specimen response may have been responsible for this frustrating situation. Also the specimen was apparently broken by thermal stresses during the oscillation tests. Although the size of the specimen we use is restricted by thermal stress considerations, some increase is possible. Also, the specimen material changes may make a difference. For this reason we have constructed and installed a new capsule containing a somewhat larger specimen of fine-grain UO_2. We have hopes that this specimen will allow an extension of the frequency range. Also, we will try to revise the mathematical approach.

[redacted]

Previous reports in this series are:

ORNL-TM-920	Period Ending June 30, 1964
ORNL-TM-960	Period Ending September 30, 1964
ORNL-TM-1000	Period Ending December 31, 1964
ORNL-TM-1100	Period Ending March 31, 1965
ORNL-TM-1200	Period Ending June 30, 1965
ORNL-TM-1270	Period Ending September 30, 1965
ORNL-TM-1400	Period Ending December 31, 1965
ORNL-TM-1500	Period Ending March 31, 1966
ORNL-TM-1570	Period Ending June 30, 1966
ORNL-TM-1700	Period Ending September 30, 1966
ORNL-TM-1720	Period Ending December 31, 1966
ORNL-TM-1825	Period Ending March 31, 1967

[redacted]

[redacted]

INTERNAL DISTRIBUTION

1–3. Central Research Library
4–5. ORNL – Y-12 Technical Library Document Reference Section
6–15. Laboratory Records Department
16. Laboratory Records, ORNL R.C.
17. ORNL Patent Office
18. G. M. Adamson, Jr.
19. J. H. Barrett
20. S. E. Beall
21. R. J. Beaver
22. M. Bender
23. R. G. Berggren
24. J. O. Betterton, Jr.
25. D. S. Billington
26. A. L. Boch
27. B. S. Borie
28. G. E. Boyd
29. W. H. Bridges
30. R. B. Briggs
31. W. E. Brundage
32. D. A. Canonico
33. R. M. Carroll
34. J. V. Cathcart
35. G. W. Clark
36. K. V. Cook
37. G. L. Copeland
38. J. H. Crawford
39. F. L. Culler
40. J. E. Cunningham
41. J. H. DeVan
42. C. V. Dodd
43. K. Farrell
44. J. I. Federer
45. B. E. Foster
46. A. P. Fraas
47. J. H Frye, Jr.
48. R. J. Gray
49. W. R. Grimes
50. H. D. Guberman
51. D. G. Harman
52. W. O. Harms
53–54. M. R. Hill
55. N. E. Hinkle
56. D. O. Hobson
57. H. W. Hoffman
58. W. R. Huntley
59. H. Inouye
60. T. N. Jones
61. G. W. Keilholtz
62. B. C. Kelley
63. J. A. Lane
64. C. F. Leitten, Jr.
65. A. P. Litman
66. A. L. Lotts
67. R. N. Lyon
68. H. G. MacPherson
69. R. E. MacPherson
70. M. M. Martin
71. W. R. Martin
72. R. W. McClung
73. H. E. McCoy, Jr.
74. H. C. McCurdy
75. R. E. McDonald
76. D. L. McElroy
77. C. J. McHargue
78. F. R. McQuilkin
79. A. J. Miller
80. E. C. Miller
81. J. G. Morgan
82. F. H. Neill
83. T. A. Nolan (K-25)
84. S. M. Ohr
85. P. Patriarca
86. A. M. Perry
87. S. Peterson
88. R. E. Reed
89. P. L. Rittenhouse
90. W. C. Robinson
91. M. W. Rosenthal
92. G. Samuels
93. A. W. Savolainen
94. J. L. Scott
95. O. Sisman
96. G. M. Slaughter
97. N. K. Smith
98. S. D. Snyder
99. I. Spiewak
100. J. T. Stanley
101. W. J. Stelzman
102. J. O. Stiegler
103. D. B. Trauger
104. R. P. Tucker

[redacted]

[redacted]

105. J. T. Venard
106. G. M. Watson
107. A. M. Weinberg
108. J. R. Weir, Jr.
109. W. J. Werner
110. H. L. Whaley
111. G. D. Whitman
112. J. M. Williams
113. R. O. Williams
114. J. C. Wilson
115. F. W. Young, Jr.
116. C. S. Yust

EXTERNAL DISTRIBUTION

117–120. F. W. Albaugh, Battelle, PNL
121–123. R. J. Allio, Westinghouse Atomic Power Division
124. R. D. Baker, Los Alamos Scientific Laboratory
125. C. Baroch, Babcock and Wilcox
126. L. Brewer, University of California, Berkeley
127. V. P. Calkins, GE, NMPO
128. W. Cashin, Knolls Atomic Power Laboratory
129. S. Christopher, Combustion Engineering, Inc.
130. D. B. Coburn, General Atomic
131. D. F. Cope, RDT, SSR, AEC, Oak Ridge National Laboratory
132. G. K. Dicker, Division of Reactor Development and Technology, AEC, Washington
133. D. E. Erb, Division of Reactor Development and Technology, AEC, Washington
134. E. A. Evans, GE, Vallecitos
135. W. C. Francis, Idaho Nuclear Corporation
136. A. J. Goodjohn, General Atomic
137. R. G. Grove, Mound Laboratory
138. D. H. Gurinsky, BNL
139. A. N. Holden, GE, APED
140–142. J. S. Kane, Lawrence Radiation Laboratory, Livermore
143. H. Kato, U.S. Department of the Interior, Bureau of Mines
144. E. A. Kintner, Fuel Fabrication Branch, AEC, Washington
145. J. H. Kittel, ANL
146. E. J. Kreih, Westinghouse, Bettis Atomic Power Laboratory
147. W. J. Larkin, AEC, Oak Ridge Operations
148. W. L. Larsen, Iowa State University, Ames Laboratory
149. J. J. Lombardo, NASA, Lewis Research Center
150. J. H. MacMillan, Babcock and Wilcox Company
151. R. Mayfield, ANL
152. M. McGurty, GE, NMPO
153. M. Nevitt, ANL
154. R. E. Pahler, Division of Reactor Development and Technology, AEC, Washington
155. S. Paprocki, BMI
156. D. Ragone, General Atomic
157. W.L.R. Rice, AGMR, AEC, Washington
158. B. Rubin, Lawrence Radiation Laboratory, Livermore
159. F. C. Schwenk, Division of Reactor Development and Technology, AEC, Washington

[redacted]

[redacted]

160–162. J. M. Simmons, Division of Reactor Development and Technology, AEC, Washington
163. L. E. Steele, Naval Research Laboratory
164. R. H. Steele, Division of Reactor Development and Technology, AEC, Washington
165. W. F. Sheely, Division of Research, AEC, Washington
166. A. Strasser, United Nuclear Corporation
167. A. Taboada, Division of Reactor Development and Technology, AEC, Washington
168. A. Van Echo, Division of Reactor Development and Technology, AEC, Washington
169. R. Van Tyne, Illinois Institute of Technology Research Institute
170. C. E. Weber, Atomics International
171. J. F. Weissenberger, RDT, OSR, GE, NMPO
172. G. W. Wensch, Division of Reactor Development and Technology AEC, Washington
173. E. A. Wright, AEC, Washington
174. Division of Research and Development, AEC, Oak Ridge Operations
175–189. Division of Technical Information Extension